Theoretical investigations of wide-bandgap semiconductor nanowires for optoelectronic applications

by Dennis Franke

University of Bremen 2018

Theoretical investigations of wide-bandgap semiconductor nanowires for optoelectronic applications

Dissertation
zur Erlangung des akademischen Grades

Doktor der Naturwissenschaften
(Dr. rer. nat.)

am Fachbereich Physik und Elektrotechnik
der Universität Bremen

vorgelegt von
M. Sc. Dennis Franke

1. Gutachter: Prof. Dr. rer. nat. Thomas Frauenheim
2. Gutachter: Prof. Dr. rer. nat. Frank Jahnke

Bremen, 21. Dezember 2018

"You are only given a little spark of madness. You must not lose it."

Robin Williams

Abstract

University of Bremen
Department of Physics and Electrical Engineering

Doctor rerum naturalium

Theoretical investigations of wide-bandgap semiconductor nanowires for optoelectronic applications

by Dennis Franke

Improving existing optoelectronic devices is a crucial step in satisfying humanity's increasing demand for electricity. This work explores different ways to achieve this goal. First density functional theory (DFT) calculations are performed on functionalized ZnO and GaN surface structures to investigate possible changes to their structural, electronic, and optical properties due to the attached functional groups. For both materials, attaching thiol groups leads to intra-gap states, which are found to be optically active for ZnO.
Aiming at bigger GaN model sizes in future works compared to standard DFT approaches, a DFTB model was developed for GaN surface nanostructures. The interatomic interaction parameters were validated against standard DFT, achieving acceptable performances on bulk Ga, bulk GaN, and surface GaN systems.
Another possible route to modify the electronic properties of semiconductor nanostructures is doping. ZnO bulk was doped with cobalt atoms to model different intrinsic defect complexes. Many-body GW calculations were employed to investigate their electronic structures. One defect complex is identified to be responsible for the experimentally observed photoluminescence.
Due to the continuing decrease in size of electronic devices, the standard gate oxide SiO_2 needs to be replaced, since today's required film thicknesses expose a crucial weakness of SiO_2, a high tunneling leakage current. Possible candidates to be used as a replacement are $Hf_xSi_{1-x}O_2$ nanostructures, that avoid the described weakness. In a first step a density functional-based tight binding (DFTB) model for HfO_2 was developed and validated against standard DFT calculations, achieving a very good performance for Hf bulk and HfO_2 bulk. The obtained parameters were then used in a MD study on amorphous HfO_2 systems to discuss their structural and electronic properties. In a second step this model was extended by silicon and applied to amorphous $Hf_xSi_{1-x}O_2$ structures to evaluate the influence of different Hf:Si ratios.

Contents

List of Figures

List of Tables

List of Abbreviations

BLYP	**B**ecke **L**ee **Y**ang **P**arr
CBM	**C**onduction **B**and **M**inimum
DFT	**D**ensity **F**unctional **T**heory
DFTB	**D**ensity **F**unctional based **T**ight **B**inding
DOS	**D**ensity **O**f **S**tates
GGA	**G**eneralized **G**radient **A**pproximation
HOMO	**H**ighest **O**ccupied **M**olecular **O**rbital
HSE	**H**eyd **S**cuseria **E**rnzerhof
LDA	**L**ocal **D**ensity **A**pproximation
LUMO	**L**owest **O**ccupied **M**olecular **O**rbital
MD	**M**olecular **D**ynamics
MPA	**M**ercapto **C**arboxylic **A**cid
PBE	**P**erdew **B**urke **E**rnzerhof
PBE0	**P**erdew **B**urke **E**rnzerhof **0**
PV	**P**hoto**v**oltaic
RE	**R**are **E**arth
SK	**S**later **K**oster
TDDFT	**T**ime **D**ependent **D**ensity **F**unctional **T**heory
TM	**T**ransition **M**etal
VBM	**V**alence **B**and **M**aximum

Dedicated to Helena, who helped me to rediscover the faith in myself.

"To thine own self be true."

Polonius in Hamlet

Chapter 1

Introduction

1.1 Semiconductors for optoelectronics

Humanity is currently facing one of the biggest technological challenges since the Industrial Revolution in the 18th century. Fossil fuels need to be replaced successively by renewable energies. But this task can only succeed, if energy is used more efficiently and renewable energies are made easier accessible. At the end of 2016, renewable energies accounted for 10.4 % of the global energy consumption [1]. 1.6 % were generated from solar-based sources. However, solar photovoltaic (PV) capacity grew continuously over the past years, adding more than 5000 % over the last decade. In particular 2017 was a remarkable year. Solar PV installations added more net capacity than natural gas, nuclear power, and coal combined [1]. This development is not surprising, since every year, harvestable sun energy hits the earth which is about three orders of magnitude bigger than the global energy consumption in 2017.

Nowadays, solar cells are still predominantly made of crystalline silicon or compounds partially made of crystalline silicon with a typical efficiency between 15 and 22 %. This rapid growth in capacity can be attributed to the decreasing cost of the solar panels over the years. It reduced by over 60 % between 2010 and 2017 with the semiconductor module itself being the largest impact factor [2]. Manufacturing costs decreased by 86 %, the module accounts for only 12 to 34 % of the total cost, depending on the type of solar panel. On the other hand, so-called "soft costs" like installment costs, taxes, profits, or overheads remained almost constant. Consequently there is a natural limit to the total cost since the semiconductor's contribution will decrease even further. Therefore, the second way to reduce the cost is to increase the panel's efficiency. That way more energy can be generated with the same number of panels. As a consequence, scientific interest in high-efficiency PV installments has grown over the past years. In order to achieve higher efficiency rates, silicon is combined with wide-bandgap materials. Very recently an efficiency of 33.3 % was achieved by combining Si with GaAs and GaInP [3]. A good example for the scientific effort in this field is the development of perovskite solar cells. First mentioned in 2009 with an efficiency of only 3.8 %

[4], recently researchers in Hong Kong successfully developed perovskite-silicon solar cells with an efficiency of 25.5 % [5].

Silicon has been the material of choice for applications in the semiconductor industry since the invention of the first transistor in 1948 [6]. Main reasons for this are its low cost and its ability to form an insulating silicon dioxide layer for the use as a gate oxide for example in diodes, transistors, or PV panels. However, due to the continuing decrease in size of electronic devices, silicon dioxide is no longer reliable as the first choice, since the small thickness leads to high tunneling leakage current [7, 8]. Consequently, possible replacing materials need to be investigated. In addition, silicon is not suited for applications in light-emitting devices, since it is an Sindirect semiconductor. Therefore, an emission process is unlikely to happen.

But besides harvesting renewable energies more effectively, energy in general needs to be used more efficiently. One major contributor to the global electricity consumption is lighting. It is responsible for around 20 % of the global electricity consumption [9]. This is mainly due to the fact that light emitting diode (LED) still do not account for the vast majority of the global lighting. However, during the past years, the LED market grew considerably and LED-based devices accounted for 54 % of the global lighting market in 2017 [10]. Consequently, there is tremendous potential for further growth left. LEDs are up to 90 % more efficient than traditional incandescent bulbs and therefore the global energy consumption would benefit greatly from the described growth. Furthermore, similar to the aforementioned solar cells, LEDs also benefit from the reduced costs of semiconductor modules.

One possible route to address the aforementioned challenges and opportunities are semiconductor-based nanowires. Nanowires are nanostructures with a diameter of the order of a few nanometers and a large length-to-width ratio. Furthermore, they also have a large surface-to-volume ratio. These properties make them interesting in particular for optoelectronic applications like PV devices or LEDs. Figure 1.1 shows a SEM image of grown ZnO nanowires. Nanowires are typically being synthesized by two different approaches, either top-down or bottom-up. Top-down approaches use lithography techniques to etch out thin structures from a bulk material. This provides an easy way to synthesize ordered arrays of nanowires, which makes it appealing for the use in optoelectronic devices. However, the desired target sizes are limited by the employed lithography technique and the considered wavelength. Thus more advanced lithography approaches need to be used, which lead to a drastic increase of cost of the nanowires. In contrast, bottom-up approaches use gases or liquids as precursors in order to grow a crystalline structure by assembling the molecules step by step. This approach offers greater control over the nanowire composition, providing access to more

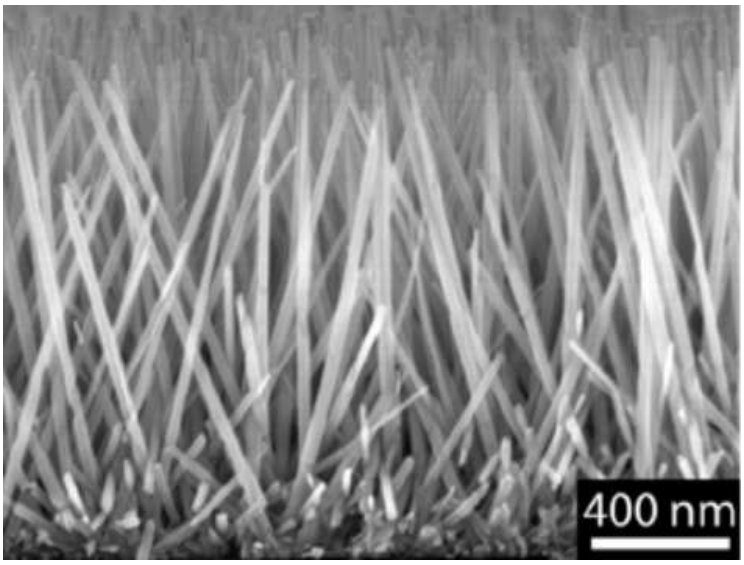

FIGURE 1.1: SEM image of ZnO nanowires. Reprinted from [11], Copyright 2013, with permission from Elsevier.

complex forms. On the other hand, growing ordered arrays is challenging compared to the top-down approach.

Improving these processes as well as developing different techniques to alter and enhance the optoelectronic properties of nanowires is of great interest to many scientific research groups and companies around the globe. The following chapters will discuss different approaches on how to alter the optoelectronic properties of semiconductor nanostructures. Furthermore, a study on possible replacements for silicon oxide in electronic devices will be presented.

1.2 Theoretical approach

Throughout history mankind has driven technological developments further with determination and invented increasingly sophisticated devices along the way. Nowadays it is possible to investigate materials on an atomic scale experimentally and to observe time-dependent phenomena on femtosecond and sometimes even attosecond timescales. Nevertheless, it is still a challenging task to attain information and knowledge on an atomic scale directly from experiments without any supporting information such as theoretical input.

This raises the question, is there a way to combine theoretical and experimental approaches to overcome the described difficulty?

One possible solution is the use of increasingly powerful computers. Computer simulations serve as a bridge between microscopic length and time scales in a real material and the macroscopic world inside a laboratory. A main benefit is

the complete control over the chosen parameters. Furthermore, it provides safety and even allows to simulate conditions, which are very hard or even impossible to employ in a laboratory like extreme temperatures or extremely short time steps. From a practical point of view it is also cheaper and therefore allows to test several different simulation conditions before actually conducting an experiment. Thus, computer simulations in materials science could be described as virtual experiments.

However, even with today's computational resources, approximations have to be made to a certain point, because an exact solution is simply too complex to achieve for anything else than trivial problems. Several approximations and consequently different levels of accuracy will be introduced and applied to different physical systems in this thesis.

1.3 Outline of this thesis

This thesis is organized as follows. Chapter 2 introduces DFT, TDDFT, and the GW method. The key aspects and physical ideas behind these approaches are explained. Chapter 3 briefly reviews the DFTB method and the necessary approximations needed in order to make it work. In Chapter 4 the concept of MD is introduced. The connection between statistical physics and computational materials science is derived and established in order to demonstrate how the dynamics of an atomistic system can be treated with the use of a computer.

Chapter 5 presents the results for surface functionalization of ZnO and GaN nanostructures. Referring to Chapter 2, the parameters for the executed DFT and TDDFT calculations are given. In the first part the obtained results for mercaptocarboxylic acids (MPA)-derived molecules ($SH-(CH_2)_n-COOH$) on ZnO surfaces are shown. Structural as well as electronic and optical properties are discussed. The second part reviews the functionalization of GaN surfaces with thiol, carboxyl, and amine groups and evaluates the possibility to influence the electronic and optical properties of GaN-based nanostructures.

A correct description of TM or RE-doped ZnO nanostructures is a challenging task. The usual approaches within standard DFT often fail to describe the band gap and especially the position of defect states accurately. Therefore, in Chapter 6 the GW approximation is validated for bulk ZnO and then applied to cobalt-doped ZnO nanostructures with different defect complexes. Structural as well as electronic properties are discussed in order to evaluate which defect complex might be responsible for the photoluminescence that has been observed in experiments on Co-doped ZnO.

Even nowadays, describing a system of several hundred atoms in DFT is computationally very expensive. Different DFT-based methods like the introduced DFTB approach provide a way to overcome this difficulty. In Chapter 7 the DFTB parametrizations of HfO_2, $Hf_xSi_{1-x}O_2$, and GaN are presented and tested on different target systems. The obtained parameters for HfO_2 are used within a MD study to generate information about the influence of a varying density on the structural and electronic properties of amorphous HfO_2 systems. For further validation of the parametrization, the results are compared to classically obtained models and DFT calculations from the literature. The parametrization for $Hf_xSi_{1-x}O_2$ has also been validated against both a classical MD study and a DFT MD approach. Chapter 8 concludes the thesis.

Chapter 2

Density functional theory

This chapter will present a brief overview of the Density Functional Theory (DFT) to the extent appropriate for the scope of this thesis. A more detailed review of the background, exact mathematical formulation and available extensions can be found in the literature [12–14].

2.1 Wave mechanics

The basic problem in computational materials science related calculations is solving the Schrödinger equation

$$\hat{H}\Phi^n(x_i) = E^n\Phi^n(x_i). \tag{2.1}$$

with $\mathbf{x}_i \equiv (\mathbf{r}_i, \sigma_i)$ containing the spatial and spin coordinates and Φ describing the time-independent many-electron wave function for N interacting electrons

$$\Phi^n = \Phi^n(x_i), \qquad i = 1...N. \tag{2.2}$$

n labels the different energetic states with the ground state having the lowest energy. The stationary and non-relativistic Hamiltonian of a many-body system is given by

$$\hat{H} = \sum_i^N \hat{h}_1(\mathbf{r}_i) + \frac{1}{2}\sum_{i\neq j}^N \hat{h}_2(\mathbf{r}_i, \mathbf{r}_j) \tag{2.3}$$

with

$$\begin{aligned} \hat{h}_1(\mathbf{r}_i) &= -\frac{1}{2}\nabla_i^2 - \sum_I^{N_n} \frac{Z_I}{|\mathbf{r}_i - \mathbf{R}_I|} \\ \hat{h}_2(\mathbf{r}_i, \mathbf{r}_j) &= \frac{1}{|\mathbf{r}_i - \mathbf{r}_j|} \end{aligned}. \tag{2.4}$$

This Hamiltonian is valid in the Born-Oppenheimer approximation, which opens up the possibility to separate the motion of the electrons from the motion of the nuclei. This is justified by the large mass difference and therefore vastly different time and length scales for the electrons and nuclei.

The aforementioned Schrödinger equation is a second-order partial differential equation, which cannot be solved analytically for a many-electron system due to the electron-electron interaction. There have been several approaches to deal with this problem, such as the Hartree- and Hartree-Fock theory [15, 16]. The former describes the many-electron wavefunction Φ as a product of one-electron orbitals, while the latter extends this to a Slater determinant of spin orbitals. The Slater determinant formulation ensures an antisymmetric solution and indistinguishable particles, and thus fulfills Pauli's exclusion principle. While Hartree-Fock theory can describe exchange interaction correctly, it cannot treat correlation effects. Extensions like a linear combination of Slater determinants can describe configuration interaction between states, but due to the interaction of all electrons in a system, including spatial and spin variables, the computational complexity increases drastically and scales exponentially to the number of atoms.

Density Functional Theory takes a completely different approach by reformulating the basic problem in terms of a simpler and more convenient variable, the electron density $n(\mathbf{r})$. The major advantage in using the electron density as the main variable is its dependency on only three variables.

2.2 Hohenberg-Kohn theorems

Density Functional Theory is based on two theorems stated in 1964 by Hohenberg and Kohn [17]. The first one can be formulated as

> *The external potential is a unique functional of the electron density in the ground state, and therefore the total energy is also a functional of the ground state electron density.*

Following this theorem, the electron density n determines the ground state wavefunction Φ and thus all ground state properties of a given system, meaning that these properties can be expressed as a functional of the density. In particular, the total energy functional can be written as

$$E[n(\mathbf{r})] = F[n(\mathbf{r})] + \int d\mathbf{r} V_{\text{ext}}(\mathbf{r}) n(\mathbf{r}). \tag{2.5}$$

with $F[n(\mathbf{r})]$ describing an unknown, but universal functional of the electron density, which consists of a kinetic energy functional T and an interaction functional U_{ee} that contains all non-classical effects. Since the functional $F[n(\mathbf{r})]$ is the same

for all N-electron systems, the Hamiltonian H is entirely defined by the number of electrons N and the external potential $V_{\text{ext}}(\mathbf{r})$. The second theorem states the following:

> *Given a system with the electronic density $n(\mathbf{r})$, the ground state energy E_0 corresponds to the global minimum of the total energy functional $E[n(\mathbf{r})]$, and the density $n_0(\mathbf{r})$, which minimizes $E[n(\mathbf{r})]$, is the exact ground state density.*

So the ground state energy in DFT is the minimum value of the energy functional and obtained, when the functional is evaluated at the ground state density. With $n(\mathbf{r})$ being the ground state density and $n'(\mathbf{r})$ being another density, the theorem can be summarized as follows

$$E[n'(\mathbf{r})] > E[n(\mathbf{r})]. \tag{2.6}$$

2.3 Kohn-Sham formalism

There are still some remaining problems in the theory of Hohenberg and Kohn, and those concern finding the ground state density and a proper expression for the functional $F[n(\mathbf{r})]$ in order to be able to determine the ground state energy. Kohn and Sham suggested the following separation of $F[n(\mathbf{r})]$ in 1965 [18]:

$$F[n(\mathbf{r})] = T_0[n(\mathbf{r})] + E_{\text{H}}[n(\mathbf{r})] + E_{\text{XC}}[n(\mathbf{r})]. \tag{2.7}$$

Here $T_0[n(\mathbf{r})]$ describes the ground state kinetic energy functional for a fictious system of N non-interacting electrons

$$T_0[n(\mathbf{r})] = \sum_i n_i \int d\mathbf{r} \Phi_i^*(\mathbf{r})(-\frac{1}{2}\nabla^2)\Phi_i(\mathbf{r}). \tag{2.8}$$

$E_{\text{H}}[n(\mathbf{r})]$ is the Hartree energy, a classical term describing the Coulomb repulsion

$$E_{\text{H}}[n(\mathbf{r})] = \frac{1}{2}\int\int d\mathbf{r} d\mathbf{r}' \frac{n(\mathbf{r})n(\mathbf{r}')}{|\mathbf{r}-\mathbf{r}'|}. \tag{2.9}$$

Lastly, E_{XC} is the exchange-correlation functional accounting for all the non-classical many-body effects and given by

$$E_{\text{XC}}[n(\mathbf{r})] = T[n(\mathbf{r})] - T_0[n(\mathbf{r})] + U_{\text{ee}}[n(\mathbf{r})] - E_{\text{H}}[n(\mathbf{r})], \tag{2.10}$$

where $T[n(\mathbf{r})]$ is teh kinetic energy of the interacting system. The terms n_i and Φ_i in Eq. (2.8) are the normalized occupation number and the eigenfunctions

obtained by solving the one-electron Schrödinger equation for an effective single-electron potential V_{eff}

$$(-\frac{1}{2}\nabla^2 + V_{eff}(\mathbf{r}))\Phi_i(\mathbf{r}) = \varepsilon_i\Phi_i(\mathbf{r}), \tag{2.11}$$

respectively. Then, the electron density can be written as follows

$$n(\mathbf{r}) = \sum_{i=1}^{\text{occ}} n_i|\Phi_i(\mathbf{r})|^2, \qquad N = \int d\mathbf{r}n(\mathbf{r}). \tag{2.12}$$

The aforementioned Φ_i are the so-called Kohn-Sham orbitals, describing normalized single-electron orbitals

$$\int d\mathbf{r}\Phi_i^*(\mathbf{r})\Phi_i(\mathbf{r}) = \int d\mathbf{r}|\Phi_i(\mathbf{r})|^2 = 1. \tag{2.13}$$

This results in the following form for the Kohn-Sham energy functional

$$E_{\text{KS}}[n(\mathbf{r})] = \sum_i n_i \int d\mathbf{r}\Phi_i^*(\mathbf{r})(-\frac{1}{2}\nabla^2 + V_{ext}(\mathbf{r}) + \frac{1}{2}\int \frac{n(\mathbf{r}')}{|\mathbf{r}'-\mathbf{r}|}d\mathbf{r}')\Phi_i(\mathbf{r}) + E_{\text{XC}}[n(\mathbf{r})]. \tag{2.14}$$

Besides the last term $E_{\text{XC}}[n(\mathbf{r})]$ every part has an analytical form. This exchange-correlation term needs to be approximated, apart from that the Kohn-Sham theory is exact. Several different approaches to tackle this problem have emerged over the course of the last five decades and will be discussed in the next section. The ground state energy of the functional in Eq. (2.14) can be found by applying the variation principle under consideration of the normalization condition. Using the Euler-Lagrange formalism, the variation at the ground state energy needs to be equal to zero

$$\frac{\delta}{\delta\Phi_i^*(\mathbf{r})}\Omega[\{\Phi_i(\mathbf{r})\}] = \frac{\delta}{\delta\Phi_i^*(\mathbf{r})}\{E[n(\mathbf{r})] - \sum_i^N\sum_j^N \varepsilon_{ij}(\int d\mathbf{r}\Phi_i^*(\mathbf{r})\Phi_j(\mathbf{r}) - 1)\} = 0. \tag{2.15}$$

This results in the so-called Kohn-Sham equations

$$\{-\frac{1}{2}\nabla^2 + V_{\text{ext}}(\mathbf{r}) + \int d\mathbf{r}'\frac{n(\mathbf{r}')}{|\mathbf{r}'-\mathbf{r}|} + V_{\text{XC}}[n(\mathbf{r})]\}\Phi_i(\mathbf{r}) = \varepsilon_i\Phi_i(\mathbf{r}). \tag{2.16}$$

with

$$V_{\text{XC}}[n(\mathbf{r})] = \frac{\delta E_{\text{XC}}[n(\mathbf{r})]}{\delta n(\mathbf{r})}. \tag{2.17}$$

With the effective potential

$$V_{\text{eff}}[n(\mathbf{r}), \mathbf{r}] = V_{\text{ext}}(\mathbf{r}) + \int d\mathbf{r}' \frac{n(\mathbf{r}')}{|\mathbf{r} - \mathbf{r}'|} + V_{\text{XC}} \tag{2.18}$$

this set of effective single-electron equations has the form of a Hartree equation with the Kohn-Sham eigenfunctions $\Phi_i(\mathbf{r})$ and eigenenergies ε_i

$$[-\frac{1}{2}\nabla^2 + V_{\text{eff}}([n(\mathbf{r})], \mathbf{r})]\Phi_i(\mathbf{r}) = \varepsilon_i \Phi_i(\mathbf{r}). \tag{2.19}$$

The Kohn-Sham equations are solved self-consistently, since $V_{\text{eff}}([n(\mathbf{r})], \mathbf{r})$ is a functional of the electron density, which is being calculated by using the desired wavefunctions $\Phi_i(\mathbf{r})$. Solving these equations analytically is unrealistic, so in order to find a solution, the process starts with guessing a start effective potential and using that as a starting point of the iteration scheme.

2.3.1 The plane wave formalism in DFT

In a crystalline system, a large number of atoms and consequently a large number of electrons and ions needs to be described by the employed theory. This is computationally unattainable and therefore this number needs to be reduced in practice. Bloch's theorem is used for this purpose. It states that the wave functions $\Phi_{n\mathbf{k}}(\mathbf{r})$ of an electron in a periodic potential can be expressed as the product of the cell-periodic $u_n(\mathbf{r})$ and a plane wave function $e^{i\mathbf{kr}}$

$$\Phi_{n\mathbf{k}}(\mathbf{r}) = u_n(\mathbf{r}) e^{i\mathbf{kr}}, \tag{2.20}$$

with n as the band index and $\mathbf{k}$ as a vector in reciprocal space that is confined to the first Brillouin zone. The cell-periodic $u_n(\mathbf{r})$ has the same periodicity as the crystal lattice and can thus be expressed as a Fourier expansion of plane waves with reciprocal lattice vectors $\mathbf{G}$ of the crystal as wave vectors

$$u_n(\mathbf{r}) = \sum_{\mathbf{G}} C_{n,\mathbf{G}} e^{i\mathbf{Gr}}. \tag{2.21}$$

$\mathbf{G}$ obeys the relation $\mathbf{GR} = 2\pi m$ with $\mathbf{R}$ as a lattice vector in real space. Combining Eqs. (2.20) and (2.21), every single-electron wave function can be described as a sum of these plane waves

$$\Phi_{n\mathbf{k}}(\mathbf{r}) = \sum_{\mathbf{G}} C_{n,\mathbf{k}+\mathbf{G}} e^{i(\mathbf{k}+\mathbf{G})\mathbf{r}}. \tag{2.22}$$

Expressing the wave functions in terms of plane waves in reciprocal space allows a formulation of the Kohn-Sham equations in reciprocal space. Using the fact that

the contributions to the effective potential in the Kohn-Sham equation (Eq. 2.19) can be written as follows

$$v(\mathbf{r}) = \sum_{\mathbf{G}} \tilde{v}(\mathbf{G}) e^{i\mathbf{G}\mathbf{r}}, \tag{2.23}$$

where $\tilde{v}(\mathbf{G})$ is the Fourier transform of the respective variable in real space, and substituting Eq. (2.22) into Eq. (2.19), leads to the reciprocal space form of the Kohn-Sham equations

$$\sum_{\mathbf{G}'} \{ \frac{|\mathbf{k}+\mathbf{G}|^2}{2} \delta_{\mathbf{G}\mathbf{G}'} + \tilde{v}_{\text{ext}}(\mathbf{G}-\mathbf{G}') + \tilde{v}_{\text{H}}(\mathbf{G}-\mathbf{G}') + \tilde{v}_{\text{XC}}(\mathbf{G}-\mathbf{G}') \} C_{n,\mathbf{k}+\mathbf{G}'} = \varepsilon_i(\mathbf{k}) C_{n,\mathbf{k}+\mathbf{G}}. \tag{2.24}$$

Here, the first term is the kinetic energy, and the other three terms on the left side of the equation are the Fourier representations of the external, the Hartree, and the exchange-correlation functionals, respectively. It can be seen that the kinetic energy is diagonal. An infinite number of plane waves needs to be considered for an exact calculation, but since this is in practice not possible, an kinetic energy cutoff is employed to consider only plane waves with a kinetic energy smaller than the cutoff. This also defines the dimension of the Hamilton matrix in Eq. (2.24)

$$\frac{|\mathbf{k}+\mathbf{G}|^2}{2} \leq E_{\text{cut}}. \tag{2.25}$$

Increasing E_{cut} leads to a larger plane wave basis set and will therefore yield more accurate results, however, it will also make the calculation computationally more demanding. Thus, finding a reasonable compromise between accuracy and complexity is important. The main weakness of the plane-waves approach is the poor description of orbitals close to the nucleus. The strong changes of the potential and wave functions near the nucleus require an unreasonable large number of basis functions. This problem is avoided in practice by employing pseudo potentials, which lead to a smooth behaviour of the wave functions in the core region. Throughout this work, the projector-augmented wave method (PAW) has been used to construct these pseudo potentials for all DFT calculations [19, 20].

2.3.2 Sampling the Brillouin zone

According to Bloch's theorem, the electrons in a unit cell can be found at an infinite number of **k**-points. Consequently, an integral in real space over the unit cell can be replaced by an integral in reciprocal space over the first Brillouin zone. However, this would require the calculation of an infinite number of **k**-points in

reciprocal space, which is not possible in practice. But since the wave functions do not change significantly for **k**-points that are close to each other, a finite mesh of **k**-points can be employed. Consequently, any quantity $f(\mathbf{r})$ can be calculated as follows

$$f(\mathbf{r}) = \frac{\Omega}{(2\pi)^3} \int_{BZ} d\mathbf{k} F(\mathbf{k}) = \sum_n \omega_n F(\mathbf{k}_n), \tag{2.26}$$

where $F(\mathbf{k})$ is the Fourier transform of $f(\mathbf{r})$, Ω is the cell volume and ω_n is a weighting factor. The number of **k**-points required to obtain sufficiently accurate results depends on the system of interest. For example metallic system require a denser mesh and therefore more **k**-points to properly describe the Fermi surface. Thus, before actually investigating a system, the appropriate number of **k**-points has to be figured out by converging the total energy of the system with respect to the **k**-point mesh. For the calculations in this work, the Monkhorst-Pack method was used to sample the first Brillouin zone [21]. Within this method, the **k**-points are distributed evenly throughout the Brillouin zone. They are constructed as follows

$$k_{prs} = u_p \mathbf{b}_1 + u_r \mathbf{b}_2 + u_s \mathbf{b}_3, \qquad u_r = \frac{2r - q_r - 1}{2q_r}, \qquad r = 1, 2, ...q_r, \tag{2.27}$$

where $\mathbf{b}_1$, $\mathbf{b}_2$, and $\mathbf{b}_3$ are the reciprocal lattice vectors. q_r determines the number of **k**-points in r-direction (the formalism is the same for p and s).

2.4 Exchange-Correlation functionals

The biggest problem in DFT is the fact that the exact form of V_{XC} is unknown. Over the years several approximations were suggested, which are typically parametrized against high-level quantum chemical approaches. This is sometimes referred to as a weak spot of the otherwise exact DFT, but it also provides a certain level of flexibility to make small corrections to these approximations at moderate computational costs, if necessary. That being said, it is mandatory to get a deeper understanding of the existing exchange-correlation functionals. Therefore, this section will give a brief overview of the commonly used functionals.

2.4.1 Local density approximation

The simplest existing approximation to V_{XC} is the local density approximation (LDA) [18]. Kohn and Sham themselves suggested it in 1965. In LDA, the electrons of a given system are treated as an homogeneous electron gas, meaning that

the dependency of E_{XC} is strictly local

$$E_{\mathrm{XC}}^{\mathrm{LDA}}[n(\mathbf{r})] = \int d\mathbf{r} n(\mathbf{r}) \varepsilon_{\mathrm{XC}}^{\mathrm{LDA}}[n(\mathbf{r})] \tag{2.28}$$

with $\varepsilon_{\mathrm{XC}}^{\mathrm{LDA}}$ as the exchange-correlation energy per electron inside a homogeneous electron gas with density $n(\mathbf{r})$. This leads to the following potential

$$\begin{aligned} V_{\mathrm{XC}}^{\mathrm{LDA}}[n(\mathbf{r})] &= \frac{\delta E_{\mathrm{XC}}^{\mathrm{LDA}}[n(\mathbf{r})]}{\delta n(\mathbf{r})} \\ &= \frac{\delta}{\delta n(\mathbf{r})} \int d\mathbf{r} n(\mathbf{r}) \varepsilon_{\mathrm{XC}}^{\mathrm{LDA}}[n(\mathbf{r})] \qquad . \\ &= \varepsilon_{\mathrm{XC}}^{\mathrm{LDA}}[n(\vec{r})] + n(\vec{r}) \frac{\delta \varepsilon_{\mathrm{XC}}^{\mathrm{LDA}}[n(\mathbf{r})]}{\delta n(\mathbf{r})} \end{aligned} \tag{2.29}$$

LDA also assumes the possibility to split $\varepsilon_{\mathrm{XC}}^{\mathrm{LDA}}$ into two terms, describing the exchange and the correlation part, respectively.

$$\varepsilon_{\mathrm{XC}}^{\mathrm{LDA}}[n(\mathbf{r})] = \varepsilon_{\mathrm{X}}^{\mathrm{LDA}}[n(\mathbf{r})] + \varepsilon_{\mathrm{C}}^{\mathrm{LDA}}[n(\mathbf{r})] \tag{2.30}$$

The exchange part is given by the Dirac exchange-correlation functional [22] for the homogeneous electron gas and reads

$$\varepsilon_{\mathrm{X}}^{\mathrm{LDA}}[n(\mathbf{r})] = -\frac{3}{4}\left(\frac{3}{\pi} n(\mathbf{r})^{\frac{1}{3}}\right). \tag{2.31}$$

Ultimately meaning that it can be computed exactly within the boundaries of LDA. The correlation part does not have such an analytical expression. Fortunately though, in 1980 Ceperley and Alder have shown a way to calculate it with good accuracy by using Quantum Monte-Carlo methods [23]. In the following years these methods have been interpolated to provide a variety of analytical forms [24, 25].

But there is a major deficiency, namely self-interaction. This can be easily understood by taking a look at the electron-electron interaction energy. It is a sum of the Hartree part of the total energy and the exchange-correlation energy E_{XC}

$$E_{\mathrm{C}}^{\text{e-e}} = \frac{1}{2} \int d\mathbf{r} d\mathbf{r}' \frac{n(\mathbf{r}) n(\mathbf{r}')}{|\mathbf{r} - \mathbf{r}'|} + E_{\mathrm{XC}} \tag{2.32}$$

As evident from this equation, the Hartree energy contains interaction of an electron with itself, which is unphysical. This can be understood rather straightforward, since the electron-electron interaction energy is not equal to zero for an one-electron system. This self-interaction error would be cancelled by an exact

exchange-correlation energy, however, within LDA this does not happen. Nevertheless, the LDA approach performs quite well for most systems with an uniform electron distribution due to the nature of the aforementioned approximations, but usually fails for other systems like surfaces or molecules. Due to the self-interaction error, LDA typically overestimates cohesive properties, thus calculating too strong cohesion, dissociation and adsorption energies and consequently giving too small lattice constants and bond lengths.

2.4.2 Generalized gradient approximation

LDA tends to overestimate the correlation energy and underestimate the exchange energy [26]. This is due to the assumption of a uniform electron density, which is not the case for most atomic and molecular systems. In order to counter this tendency and improve upon LDA, generalized gradient approximations (GGA) have been developed, which not only take into account the electron density itself, but also its gradient to be able to describe a varying electron density more accurately [27–29]. Since the corrections take into account the density and the density gradient, so consequently information about the density surrounding a certain point **r**, they are often referred to as being semi-local. The GGA exchange-correction functional has the following general form

$$E_{\mathrm{XC}}^{\mathrm{GGA}}[n_\uparrow, n_\downarrow] = \int d\mathbf{r} f(n_\uparrow, n_\downarrow, \nabla n_\uparrow, \nabla n_\downarrow). \tag{2.33}$$

Several approaches have been made to come up with possible analytical forms for f, generally separating the exchange and the correlation part, just as in LDA. One popular example that is predominantly used in chemistry, is known as BLYP, named after Becke for the exchange part [29] and Lee, Yang and Parr for the correlation part [30] of the energy. A popular example in solid-state physics, which was the standard choice for a long time, is the PW91 functional, named after Perdew and Wang [27, 31]. It has a non-empirical form, thus it does not contain any free parameters which were fitted to experimental data. It is derived from quantum-mechanical relations. The advantage of such non-empirical GGA functionals is the applicability to a variety of problems while yielding reliable results at the same time. In contrast, empirical approaches are fitted to perform well for a specific set of elements [32]. Another functional that is commonly used especially in solid-state physics nowadays, is the PBE functional, named after Perdew, Burke and Ernzerhof [33]. It provides reliable results and describes structural and cohesive properties of solids and molecules with good accuracy. Since this functional plays a major role in this work, it will be explained in more detail. Like the PW91 functional, it is an analytical solution, meaning it is not fitted to experimental data, but rather analytically derived. E_{XC} is again separated into two

parts, the exchange part reads

$$E_{\mathrm{X}}^{\mathrm{PBE}}(n,|\nabla n|) = \int d\mathbf{r} n \varepsilon_{\mathrm{X}}^{\mathrm{LDA}}(n) F_{\mathrm{X}}^{\mathrm{PBE}}(s) \tag{2.34}$$

with $F_{\mathrm{X}}^{\mathrm{PBE}}(s)$ being the PBE exchange enhancement factor

$$F_{\mathrm{X}}^{\mathrm{PBE}}(s) = 1 + \kappa - \frac{\kappa}{1 + \frac{\mu s^2}{\kappa}}, \tag{2.35}$$

where $\kappa = 0.804$, $\mu = 0.219$, and $s = \frac{|\nabla n|}{2k_F n}$ is a dimensionless gradient term. The correlation part has the following form

$$E_{\mathrm{C}}^{\mathrm{GGA}}[n_\uparrow, n_\downarrow] = \int d\mathbf{r} n [\varepsilon_{\mathrm{C}}^{\mathrm{unif}}(r_s, \zeta) + H(r_s, \zeta, t)]. \tag{2.36}$$

with $\varepsilon_{\mathrm{C}}^{\mathrm{unif}}$ describing the correlation energy of the uniform electron gas, $r_s = \frac{k_F}{\pi}(\frac{4}{9})^{\frac{1}{3}}$ the local Seitz radius, $\zeta = \frac{n_\uparrow - n_\downarrow}{n}$ the relative spin polarization and $t = \frac{|\nabla n(\mathbf{r})|}{2gk_s n(\mathbf{r})}$ a dimensionless gradient term. The following analytical form is chosen for H

$$H = \frac{e^2}{a_0}\gamma\Phi^3 ln[1 + \frac{\beta}{\gamma}t^2(\frac{1 + At^2}{1 + At^2 + A^2t^4})]. \tag{2.37}$$

with

$$A(r_s, \zeta) = \frac{\beta}{\gamma}\frac{1}{e^{-\varepsilon_{\mathrm{C}}^{\mathrm{LDA}}/\gamma\Phi^3} - 1}, \quad \Phi(\zeta) = \frac{[(1+\zeta)^{\frac{2}{3}} + (1-\zeta)^{\frac{2}{3}}]}{2}, \quad \gamma = \frac{1 - ln(2)}{\pi^2}, \tag{2.38}$$

where $\beta = 0.067$ and $\gamma = 0.031$. PBE improves upon every aspect of LDA, but still suffers from the self-interaction error and the band gap problem. One way to tackle this problem are hybrid functionals.

2.4.3 Hybrid functionals

The biggest issue with local and semi-local functional is the general underestimation of the band gap of semiconducting and insulating materials. For example GGA yields a band gap value of $E_{\mathrm{g}} = 0.7\,\mathrm{eV}$ for bulk ZnO, which is 79 % too small compared to the experimental value of $E_{\mathrm{g}}^{\mathrm{exp}} = 3.3\,\mathrm{eV}$. The effect is less drastic for GaN, but with 30 % discrepancy still of serious nature with $E_{\mathrm{g}} = 2.4\,\mathrm{eV}$ and $E_{\mathrm{g}}^{\mathrm{exp}} = 3.4\,\mathrm{eV}$. This is of fundamental importance in the context of this work and thus needs to be dealt with. An explanation for the band gap problem can be found by taking a closer look at the Kohn-Sham theory. The fundamental band

gap of a semiconductor or insulator material with N electrons is defined by the difference between the first ionization energy $I(N)$ and the first electron affinity $A(N)$ of a neutral solid [34]. With $E(M)$ as the ground state energy of a given system with M particles, the fundamental gap is also given by

$$E_{\text{g,fun}} = (E_{N+1} - E_N) - (E_N - E_{N-1}). \tag{2.39}$$

With ε^i as one-electron energies and $E_\text{g} = \varepsilon^{\text{LU}} - \varepsilon^{\text{HO}}$ as the well known HOMO-LUMO band gap, which denotes the energy difference between the highest occupied and the lowest unoccupied orbital energy, it can be shown, that E_g^{HL} equals E_g^{fun} for approximative functionals [35]. If we have a look at a qualitative sketch of the behaviour of the exchange-correlation energy for the exact Kohn-Sham case and the approximative GGA case in Fig. 2.1, it is clear that the former shows discontinuities for integer particle numbers. Based on Eq. (2.31) this leads to another

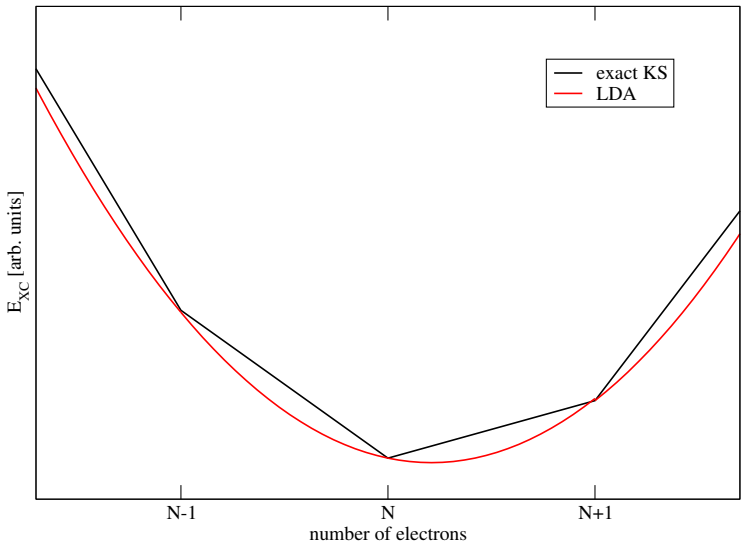

FIGURE 2.1: Qualitative sketch of the exchange-correlation energy as a function with respect to the number of electrons in a generic system. The red curve shows discontinuities at N-1, N, and N+1.

expression for the exact exchange-correlation functional

$$E_{\text{g,fun}}^{\text{exact}} = \lim_{\nu \to 0^+} \{ \frac{\delta E[n]}{\delta n(\mathbf{r})} \big|_{N+\nu} - \frac{\delta E[n]}{\delta n(\mathbf{r})} \big|_{N-\nu} \}. \tag{2.40}$$

By applying Janak's theorem $\varepsilon_i = \frac{\delta E[n]}{\delta n_i(\mathbf{r})}$ [36] with εi denoting the energy of the i-th electron and considering the derivative discontinuity Δ_{XC}, this leads to

$$\begin{aligned} E_{\text{g,fun}}^{\text{exact}} &= \varepsilon_{N+1} - \varepsilon_N + \Delta_{\text{XC}} \\ &= E_\text{g}^{\text{exact}} + \Delta_{\text{XC}} \end{aligned}. \tag{2.41}$$

This means that even in the exact exchange-correlation case, the fundamental band gap does not equal the Kohn-Sham HOMO-LUMO gap, due to the absence of the derivative discontinuity. To tackle this issue, Becke proposed in 1993 that exact exchange contributions had to be included in the calculations to compensate for the self-interaction error [37, 38]. This is achieved by admixing exact Hartree-Fock exchange and GGA exchange-correlation energy. The resulting so-called hybrid functionals have the following form

$$V_{\mathrm{XC}} = V_{\mathrm{C}}^{\mathrm{GGA}} + (1-\alpha)V_{\mathrm{X}}^{\mathrm{GGA}} + \alpha V_{\mathrm{X}}^{\mathrm{HF}}. \tag{2.42}$$

α describes the amount of exact Hartree-Fock exchange. One popular hybrid functional is the B3LYP functional, which mixes exchange and correlation energies on the LDA level with exchange and correlation energies on the GGA level with exact Hartree-Fock exchange energy [39]. The mixing parameters are fitted against a set of experimental thermochemical data. It was the first hybrid functional which was widely accepted in the DFT community, because it outperforms GGA methods especially for molecule and atom based calculations and thus made DFT popular even beyond condensed matter physics. PBE0 is another popular and widely employed hybrid functional, which calculated the exchange and correlation parts of the energy on the PBE level [40], making it a non-empirical approach. It uses an amount of 25 % Hartree-Fock exchange and reads

$$V_{\mathrm{XC}} = V_{\mathrm{C}}^{\mathrm{GGA}} + \frac{3}{4}V_{\mathrm{X}}^{\mathrm{GGA}} + \frac{1}{4}V_{\mathrm{X}}^{\mathrm{HF}}. \tag{2.43}$$

One should keep in mind that this ratio is not universally valid and strongly dependent on the system of interest [41]. Calculating exact exchange energy is computational very expensive, therefore being two to four orders of magnitude slower compared to pure DFT methods. In the case of PBE0, the long-range interaction is purely and inconsistently described, making it computational even more expensive. On the other hand it significantly improves the thermochemical and electronic properties of solids, in particular yielding accurate band gaps [42]. In 2003 Heyd, Scuseria and Ernzerhof proposed the HSE hybrid functional in order to employ a faster way to tackle the weaknesses of conventional GGA approaches [43]. It uses an error function to separate the short- and long-range Coulomb interaction, treating the short-ranged part of the exchange on the PBE0 level, while the long-ranged part is described on the PBE level. This separation is controlled by an empirical parameter ω, turning this into a semi-empirical functional.

$$E_{\mathrm{XC}}^{\mathrm{HSE}}(\omega) = \alpha E_{\mathrm{X}}^{\mathrm{HF,sr}}(\omega) + (1-\alpha)E_{\mathrm{X}}^{\mathrm{PBE,sr}}(\omega) + E_{\mathrm{X}}^{\mathrm{PBE,lr}}(\omega) + E_{\mathrm{C}}^{\mathrm{PBE}}. \tag{2.44}$$

2.5 Time-dependent density functional theory

DFT has become the go-to choice to tackle a variety of stationary physics and chemistry related problems on a computer. Nevertheless it cannot handle time-dependent phenomena, thus tremendous effort has been put into research to come up with a DFT-like approach for such non-stationary problems, the time-dependent density functional theory (TDDFT). In 1984 Runge and Gross managed to prove an analogy with the ground state Hohenberg-Kohn formalism [44]. Similar to the Hohenberg-Kohn theorems, they introduced the Runge-Gross theorem. It states that

> *For a fixed initial state and given an analytic time dependent potential, the mapping to the time dependent probability density is injective. That is, for the same initial state, two different external potentials can not give the same probability density function* $n((r), t)$.

For a time-dependent field, the Hamiltonian takes the form

$$H(t) = T + U + V_{\text{ext}}(t) \tag{2.45}$$

with T describing the kinetic energy, U denoting the electron-electron interaction, and $V_{\text{ext}}(t)$ being an external potential, which according to the theorem determines the time-dependent density of the system. In this case, the time-dependent Schrödinger equation needs to be considered

$$H(t)\Phi(\mathbf{r}, t) = i\hbar\frac{\partial}{\partial t}\Phi(\mathbf{r}, t). \tag{2.46}$$

Analogous to the time-independent formalism, one needs to find a non-interacting Hamiltonian $H_{\text{s}}(t)$ corresponding to an effective potential $V_{\text{eff}}(\mathbf{r}, t)$. Then, the Hamiltonian reads

$$H_{\text{s}}(t) = T + V_{\text{eff}}(\mathbf{r}, t). \tag{2.47}$$

Applied to the Schrödinger equation

$$H_{\text{s}}(t)\Phi_i(\mathbf{r}, t) = i\hbar\frac{\partial}{\partial t}\Phi_i(\mathbf{r}, t) = \{-\frac{1}{2}\nabla^2 + V_{\text{eff}}(\mathbf{r}, t)\}\Phi_i(\mathbf{r}, t), \tag{2.48}$$

this determines a set of Kohn-Sham wave functions $\Phi_i(\mathbf{r}, t)$, that ultimately generates the desired density

$$n(\mathbf{r}, t) = \sum_i = 1^N n_i|\Phi_i(\mathbf{r}, t)|^2. \tag{2.49}$$

Analogous to standard Kohn-Sham theory, this effective potential $V_{eff}(\mathbf{r}, t)$ consists of the applied external potential, the time-dependent Hartree potential and an exchange-correlation term.

$$V_{\text{eff}}(\mathbf{r}, t) = V_{\text{ext}}(\mathbf{r}, t) + \int d\mathbf{r}' \frac{n(\mathbf{r}', t)}{|\mathbf{r} - \mathbf{r}'|} + V_{\text{XC}}(\mathbf{r}, t). \tag{2.50}$$

Runge and Gross proposed to derive V_{XC} via the Dirac action

$$A[\Phi] = \int_{t_0}^{t_1} dt \int d\mathbf{r}' \Phi^*(\mathbf{r}', t) \{ i \frac{\partial}{\partial t} - H(t) \} \Phi(\mathbf{r}', t), \tag{2.51}$$

with $V_{\text{XC}} = \frac{\delta A_{\text{XC}}}{\delta n}$.
However, this approach suffers from a major issue. A change of the potential at a certain time cannot affect the density of earlier times, this would violate the causality. But the response functions the Dirac action produces are symmetric in time and therefore do not fulfill this principle. This problem was not solved until 1998, when van Leeuwen used the Keldysh formalism to define a new action potential A [45]. This is based on the Keldysh time contour, which uses a pseudotime parameter τ to parametrize the real time $t(\tau)$. If τ runs from an initial pseudotime τ_i to a final pseudotime τ_f, the real time t runs from t_0 to t_1 and back. The relation reads

$$V_{\text{XC}}(\mathbf{r}, t) = \frac{\delta A_{\text{XC}}}{\delta n(\mathbf{r}, \tau)} \Big|_{n(\mathbf{r},t)} \tag{2.52}$$

In contrast to standard DFT, which is a well established method, TDDFT is still less researched and therefore good approximations for the exchange-correlation functional V_{XC} are less sophisticated, although in principle, the standard DFT hybrid functionals can be employed for TDDFT. For the TDDFT calculation in Chapter 5, the PBE0 functional has been used.

2.6 The GW method

The Kohn-Sham formalism has proven itself as a successful method to describe ground state properties of various systems like metals, semiconductors, insulators or molecules. In standard DFT the many-body problem is mapped onto an effective single-particle potential created by the other electrons. But for phenomena linked to excitation such as photoemission or absorption, the energy required to add or remove an electron from the system needs to be evaluated. Kohn-Sham DFT does not provide a theoretical foundation to calculate these energies and therefore a different method needs to be employed.

In a real system, an electron (or hole) disturbs its surrounding, which results in screening effects and a change to its effective mass. Consequently these particles should be described together with that resulting screening cloud as a so-called quasiparticle. It was first introduced by Landau in 1956 and originally intended for investigating liquid helium [46]. One widely employed way to describe quasiparticles is the Green function formalism [47].

2.6.1 Introducing the Green function

The single-particle Green function $G(1,2)$ is the key quantity in many-body perturbation theory and defined as

$$G(1,2) = -i < \Psi|\hat{T}[\hat{\psi}(1)\hat{\psi}^{\dagger}(2)]|\Psi > . \tag{2.53}$$

Here, 1 and 2 are introduced as space-time-spin variables $1 \equiv \{\mathbf{r}_1, t_1, \sigma_1\}$, $2 \equiv \{\mathbf{r}_2, t_2, \sigma_2\}$. Ψ denote the N-electron many-body ground state wave function and $\hat{\psi}(1)$ and $\hat{\psi}^{\dagger}(2)$ are annihilation and creation operators in the Heisenberg picture, respectively. $\hat{T}$ is a time-ordering operator and defined as

$$\hat{T}[[\hat{\psi}(1)\hat{\psi}^{\dagger}(2)]] = \begin{cases} \hat{\psi}(1)\hat{\psi}^{\dagger}(2), & t_1 > t_2 \\ -\hat{\psi}^{\dagger}(2)\hat{\psi}(1), & t_1 < t_2 \end{cases}. \tag{2.54}$$

In the case of $t_1 > t_2$ the Green function describes the propagation of an electron from state 1 to state 2 and in the case of $t_1 < t_2$ the same process for a hole. This can be generalized to obtain the case of a N-particle Green function

$$G_N(1,...N;1',...N') = (-i)^N < \Psi|\hat{T}[\hat{\psi}(1)...\hat{\psi}(N)\hat{\psi}^{\dagger}(N')...\hat{\psi}^{\dagger}(1')]|\Psi > . \tag{2.55}$$

Using the commutation relations for fermions and the definitions of the one- and two-particle Green functions according to Eq. (2.46), we can derive the following equation of motion for the one-particle case

$$\{i\frac{\partial}{\partial t_1} - \hat{h}_0(1)\}G(1,2) + i\int d3v(1,3)G_2(1,3;2,3^+) = \delta(1,2) \tag{2.56}$$

with $v(1,2) = \frac{\delta(t_1-t_2)}{|\mathbf{r}_1-\mathbf{r}_2|}$ as the Coulomb interaction between two electrons and 3^+ describing the time with a positive infinitesimal time shift $t_3^+ = t_3 + 0^+$. Thus, the single-particle Green function's equation of motion contains the two-particle Green function and technically it is possible to construct any many-body Green function this way. This hierarchy of integro-differential equations can be closed by introducing the so-called exchange-correlation self-energy Σ_{XC} which contains all two-electron effects, leading to the following new equation of motion, the

Dyson equation

$$\{i\frac{\partial}{\partial t_1} - \hat{h}_0(1)\}G(1,2) - \int d3\Sigma_{\mathrm{XC}}(1,3)G(3,2) = \delta(1,2). \tag{2.57}$$

The self-energy is defined by

$$\int d3\Sigma_{\mathrm{XC}}(1,3)G(3,2) = -i\int d3v(1,3)G_2(1,3;2,3^+) \tag{2.58}$$

or in an explicit form using the inverse of the Green function G^{-1}

$$\Sigma_{\mathrm{XC}}(1,4) = -i\int\int d2d3v(1,3)G_2(1,3;2,3^+)G^{-1}(2,4) \tag{2.59}$$

with $\int d2G(3,2)G^{-1}(2,4) = \delta(3,4)$ as definition of the inverse. The self-energy Σ accounts for all possible many-body effects a particle can experience while propagating through a many-particle system. In general the self-energy is a non-local and non-Hermitian operator, meaning its eigenvalues are complex. The real part corresponds to exchange and correlation interactions, the imaginary part contains information about the lifetime of the particle. Introducing the non-interacting Green function G_0, which is related to the single-electron Hamiltonian and therefore has no two-particle contributions, allows the formulation of the following equation of motion

$$\{i\frac{\partial}{\partial t_1} - h_0(1)\}G_0(1,2) = \delta(1,2). \tag{2.60}$$

Finally, combining the Eqs. (2.48) and (2.51) and multiplying the resulting equation with $\int d2G^{-1}(2,4)$, this leads to the Dyson equation for the one-particle Green function

$$G^{-1}(1,2) = G_0^{-1}(1,2) - \Sigma_{\mathrm{XC}}(1,2). \tag{2.61}$$

This equation allows an approximative calculation of the interacting Green function G by using the non-interacting Green function G_0 and an approximative form for the self-energy Σ_{XC}.

2.6.2 Quasiparticle energies

The self-energy Σ only depends on the time difference between times t_1 and t_2 $\tau = t_1 - t_2$, so $\Sigma_{\mathrm{XC}}(1,2) = \Sigma_{\mathrm{XC}}(\mathbf{x}_1, \mathbf{x}_2, \tau)$. Here, $x_i \equiv \mathbf{r}_i, \sigma_i$ denotes a generalized

space-spin variable. With $\Sigma_{\mathrm{XC}}(\mathbf{x}_1, \mathbf{x}_2, \omega)$ being the corresponding Fourier transform, Eq. (2.48) may be rewritten as

$$[\omega - \hat{h}_0(\mathbf{x}_1)]G(\mathbf{x}_1, \mathbf{x}_2, \omega) - \int d\mathbf{x}_3 \Sigma_{\mathrm{XC}}(\mathbf{x}_1, \mathbf{x}_3, \omega)G(\mathbf{x}_3, \mathbf{x}_2, \omega) = \delta(\mathbf{x}_1, \mathbf{x}_2). \tag{2.62}$$

With ψ_n^{QP} and E_n^{QP} denoting the quasiparticle wavefunctions (or Dyson orbitals) and the corresponding quasiparticles, respectively, this equation can be rewritten as

$$\hat{h}_0(\mathbf{x}_1)\psi_{n\mathbf{k}}^{\mathrm{QP}}(\mathbf{x}_1) + \int d\mathbf{x}_3 \Sigma_{\mathrm{XC}}(\mathbf{x}_1, \mathbf{x}_3, E_{n\mathbf{k}}^{\mathrm{QP}})\psi_{n\mathbf{k}}^{\mathrm{QP}}(\mathbf{x}_3) = E_{n\mathbf{k}}^{\mathrm{QP}}\psi_{n\mathbf{k}}^{\mathrm{QP}}(\mathbf{x}_1). \tag{2.63}$$

These are the quasiparticle equations, yielding the quasiparticle wavefunctions $\psi_{n\mathbf{k}}^{\mathrm{QP}}$ and the corresponding quasiparticle energies $E_{n\mathbf{k}}^{\mathrm{QP}}$. The latter describe the ionization energies or electron affinities of the respective particles. Calculating the self-energy is not trivial, since it still requires the unknown two-particle Green function. One possible way to approach this problem are the integro-differential equations, Hedin [47] proposed

$$\begin{aligned}
G(1,2) &= G_0(1,2) + \int d34 G_0(1,3)[v(3)\delta(3,4) + \Sigma_{\mathrm{XC}}(3,4)]G(4,2) \\
\Sigma_{\mathrm{XC}}(1,2) &= i\int d34 G(1,4)W(1^+,3)\Gamma(4,2;3) \\
W(1,2) &= v(1,2) + \int d34 v(1,3)P(3,4)W(4,2) \\
P(1,2) &= -i\int d34 G(2,3)G(4,2)\Gamma(3,4;1) \\
\Gamma(1,2;3) &= \delta(1,2)\delta(1,3) + \int d4567 \frac{\delta\Sigma_{\mathrm{XC}}(1,2)}{\delta G(4,5)} G(4,6)G(7,5)\Gamma(6,7;3).
\end{aligned} \tag{2.64}$$

$P(1,2)$ describes the irreducible polarizability, $W(1,2)$ denotes the screened Coulomb potential, which basically describes the Coulomb potential at a point 1 in space, originating at point 2, while taking the electrons' polarization into account and $\Gamma(1,2;3)$is the so-called vertex function. Since each of Hedin's equations depends on the other four, it needs to be solved self-consistently in an iterative manner. The corresponding scheme is sketched in Fig. 2.2

2.6.3 The GW approximation

Solving Hedin's equations is in practice impossible without considering approximations due to the complexity of the self-consistency conditions. In 1969, Hedin suggested to approximate the self-energy in terms of the screened Coulomb-interaction W [48].

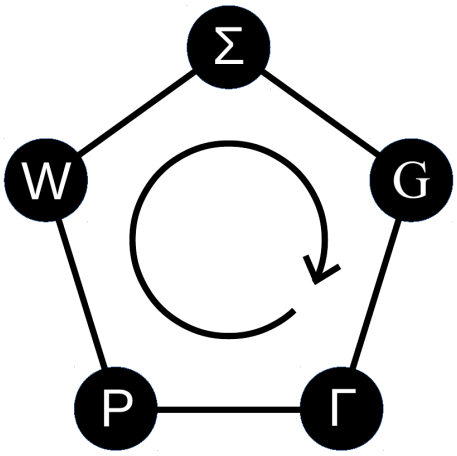

FIGURE 2.2: Qualitative sketch of the self-consistent scheme to solve Hedin's equations.

Starting with $\Gamma = 0$ and $\Sigma = 0$, this yields a vertex function without electron-hole interactions

$$\Gamma(1,2;3) = \delta(1,2)\delta(1,3) \tag{2.65}$$

and the polarizability in the independent particle approximation (or random-phase approximation RPA [49–51]) with $G = G_0$

$$P(1,2) = -iG(1,2)G(2,1). \tag{2.66}$$

After this zeroth iteration the self-energy reads as follows in the first iteration

$$\Sigma(1,2) = iG(1,2)W(1,2). \tag{2.67}$$

This is known as the GW approximation.

2.6.4 Implementation in DFT

To perform electronic structure calculations within the GW approximation in practice, the quasi-particle equation (2.54) needs to be solved. Introducing the condition that $E^{\mathrm{QP}}_{n\mathbf{k}}$ is real and considering DFT wave functions ψ_n, it can be rewritten in bra-ket notation as

$$\begin{aligned} E^{\mathrm{QP}}_{n\mathbf{k}} =& \mathrm{Re}[\langle \psi_{n\mathbf{k}} | h_0 + \Sigma_{\mathrm{XC}}(E^{\mathrm{QP}}_{n\mathbf{k}}) - V_{\mathrm{XC}} | \psi_n \rangle] \\ =& \mathrm{Re}[\langle \psi_{n\mathbf{k}} | T + V_{\mathrm{ext}} + V_H + \Sigma_{\mathrm{XC}}(E^{\mathrm{QP}}_{n\mathbf{k}}) - V_{\mathrm{XC}} | \psi_{n\mathbf{k}} \rangle]. \end{aligned} \tag{2.68}$$

Since this is an equation with respect to $E^{\mathrm{QP}}_{n\mathbf{k}}$ itself, it needs to be solved by iteration. Linearizing $\Sigma(E^{N+1}_{n\mathbf{k}}$ around $\Sigma(E^{N}_{n\mathbf{k}})$ leads to an iterative solution

$$\begin{aligned} E^{N+1}_{n\mathbf{k}} =& \mathrm{Re}[\langle\psi_{n\mathbf{k}}|T+V_{\mathrm{ext}}+V_H+\Sigma_{\mathrm{XC}}(E^{N+1}_{n\mathbf{k}})-V_{\mathrm{XC}}|\psi_{n\mathbf{k}}\rangle] \\ =& E^{N}_{n\mathbf{k}}+Z_{n\mathbf{k}}\mathrm{Re}[\langle\psi_{n\mathbf{k}}|T+V_{\mathrm{ext}}+V_{\mathrm{H}}+\Sigma(E_{n\mathbf{k}})-V_{\mathrm{XC}}|\psi_{n\mathbf{k}}\rangle-E^{N}_{n\mathbf{k}}], \end{aligned} \tag{2.69}$$

where $Z_{n\mathbf{k}}$ is the normalization factor

$$Z_{n\mathbf{k}} = \left(1-\mathrm{Re}[\langle\psi_{n\mathbf{k}}|\frac{\partial\Sigma(\omega)}{\partial\omega}|_{\omega=E^{N}_{n\mathbf{k}}}|\psi_{n\mathbf{k}}\rangle]\right)^{-1}. \tag{2.70}$$

For readability purposes, the superscript QP has been omitted.
If only one iteration step of Eq. (2.60) is performed with DFT energies as initial values, it is referred to as the G_0W_0 approximation. In the GW_0 approximation, several iterations are considered with the self-energy Σ

$$\begin{aligned} \bar{\Sigma}(\omega)_{n\mathbf{k},n\mathbf{k}} =& \langle\psi_{n\mathbf{k}}|\Sigma(E^{N}_{n\mathbf{k}})|\psi_{n\mathbf{k}}\rangle \\ =& \frac{i}{2\pi V}\sum_{\mathbf{q},\mathbf{G},\mathbf{G'}}\sum_{n'}2\int_0^\infty d\omega'\bar{W}_{\mathbf{q}}(\mathbf{G},\mathbf{G'},\omega')\langle\psi_{n\mathbf{k}}|e^{i(\mathbf{G}+\mathbf{q})\mathbf{r}}|\psi_{n'\mathbf{k}+\mathbf{q}}\rangle \\ & \langle\psi_{n'\mathbf{k}+\mathbf{q}}|e^{-i(\mathbf{G'}+\mathbf{q})\mathbf{r'}}|\psi_{n\mathbf{k}}\rangle\Big(\frac{1}{\omega+\omega'-\varepsilon_{n'\mathbf{k}+\mathbf{q}}+i\eta\mathrm{sgn}[\varepsilon_{n'\mathbf{k}+\mathbf{q}}-\mu]} \\ & +\frac{1}{\omega-\omega'-\varepsilon_{n'\mathbf{k}+\mathbf{q}}+i\eta\mathrm{sgn}[\varepsilon_{n'\mathbf{k}+\mathbf{q}}-\mu]}\Big), \end{aligned} \tag{2.71}$$

and μ as the Fermi energy. The dielectric function is kept fixed at the DFT level. Since W approaches the bare Coulomb kernel $v^{\mathrm{bare}}_{\mathbf{q}}$ at large frequencies ω, $v^{\mathrm{bare}}_{\mathbf{q}}$ has been substracted from the screened potential $\bar{W}$ to make the frequency integration well behaved

$$\bar{W}_{\mathbf{q}}(\mathbf{G},\mathbf{G'},\omega') = W_{\mathbf{q}}(\mathbf{G},\mathbf{G'},\omega') - v^{\mathrm{bare}}_{\mathbf{q}}(\mathbf{G},\mathbf{G'}). \tag{2.72}$$

The final self-energy is then obtained by adding the exact Fock exchange term

$$\Sigma(\omega)_{n\mathbf{k},n\mathbf{k}} = \bar{\Sigma}_{n\mathbf{k},n\mathbf{k}}(\omega) + \langle\psi_{n\mathbf{k}}|V_{\mathrm{X}}|\psi_{n\mathbf{k}}\rangle \tag{2.73}$$

To obtain a full PAW GW implementation, sophisticated knowledge and modeling of the dielectric function would be required. In order to avoid this, it is assumed that the dielectric matrix is an identity matrix whenever terms inside atomic spheres are evaluated. Therefore, for the evaluating of one-center terms of the self-energy, the bare Coulomb kernel replaces the screened counterpart, leading to the Hartree-Fock Hamiltonian in this case. This approximation is expected to be reliable, since differences between pseudo-wave functions and exact

wave functions are only significant for large vectors $\mathbf{G}$, but ε approaches one in these cases.

It is also important to include core-valence interaction contributions to the quasiparticle energies in Eq. (2.60), which can be done within the PAW framework. Within LDA, this yields

$$\langle \psi_{n\mathbf{k}} | V_{\mathrm{XC,core\text{-}val}}^{\mathrm{LDA}} | \psi_{n\mathbf{k}} \rangle = \langle \psi_{n\mathbf{k}} | V_{\mathrm{XC}}^{\mathrm{LDA}}(n_{\mathrm{v}} + n_{\mathrm{c}}) - V_{\mathrm{XC}}^{\mathrm{LDA}}(n_{\mathrm{v}}) | \psi_{n\mathbf{k}} \rangle, \tag{2.74}$$

where n_{c} describes the core density and n_{v} the valence density. Due to the frozen-core approximation of the applied PAW framework, the core wave functions need to be determined consistently with the partial wave functions of the valence states. A more detailed review on the implementation of the GW approximation in VASP can be found in the works of Shishkin and Kresse [52–54].

The aforementioned derivation can be summarized in the following scheme

- Starting with a Kohn-Sham system, construction the non-interacting Green function G_0 with one-electron energies and orbitals from a preliminary self-consistent GGA or hybrid DFT calculation.
- Calculation of the polarizability P.
- Calculation of the screened Coulomb-interaction W.
- Evaluation of the self-energy Σ_{GW} according to the GW approximation.
- Calculation of the quasiparticle energies E^{QP}.

Theoretically, as a next step, the Dyson equation can be solved to obtain the interacting Green function G. This procedure is then repeated until self-consistency is reached.

If only one iteration is performed without updating the Green function, this is referred to as G_0W_0. G_0W_0 has been applied successfully to a variety of problems, including electronic excitation [55, 56] and the description of semiconductors [57, 58]. It also improves the band gaps in semiconductors and insulators compared to LDA and GGA [59, 60]. Since G_0W_0 only performs one iteration, it is strongly dependent on the initial non-interacting Green function G_0 as a starting point and therefore on the underlying DFT calculation. The approximation assumes that the Kohn-Sham wavefunctions are almost equivalent to the quasiparticle counterpart, which is true in many cases, but far from reality in others [58].

One possible way to improve upon this is the GW_0 method [61, 62]. In this framework only G is updated, whereas W is kept fix at the LDA or GGA level. Formally, this is a partially self-consistent scheme, which proved to be a reasonable compromise between desired accuracy and the computational costs of fully

self-consistent GW methods [63, 64]. In this work, GW_0 calculations have been performed to determine the electronic properties of Co-doped ZnO systems in Chapter 6.

Chapter 3

Density functional based tight binding

Over the years there have been several quantum mechanical approaches to tackle biological, chemical or physical problems on a computer. DFT-based methods gained tremendous significance over the years due to their accuracy and high efficiency. But they are still very demanding in terms of computational resources, therefore less accurate and consequently less expensive methods have been developed to be able to describe larger systems and longer time spans. Among these methods, the density functional based tight binding method (DFTB) provides a very efficient way to investigate large systems of even a few thousand atoms. It is typically about two or three orders of magnitude faster than conventional DFT methods at comparable accuracy [65]. At first only intended to describe periodic solids, several extensions to the DFTB method in the last years have turned DFTB into a powerful tool to investigate a variety of problems. These extensions include the formulation to treat spin polarized systems [66] and a time-dependent formalism [67, 68]. This chapter will give a brief review of the DFTB method and its underlying mathematical derivation. A more detailed overview can be found in [69].

3.1 From DFT to DFTB

Following standard density functional theory, the total energy of an atomic system is the sum of the Kohn-Sham energy E_{KS} of an ideally self-consistent density $n(\mathbf{r})$ and the core-core repulsion E_{i-i}

$$E_{\text{tot}} = E_{\text{KS}}[n(\mathbf{r})] + E_{\text{i-i}}(\{\mathbf{R}_\alpha\}). \tag{3.1}$$

Here, $\mathbf{R}_\alpha$ denotes the ion positions. The core-core term describes a coulomb energy. Based on the Kohn-Sham representation of the electron density

$$n(\mathbf{r}) = \sum_i^N n_i |\phi_i(\mathbf{r})|^2 \tag{3.2}$$

we can write the total energy as follows

$$\begin{aligned} E_{\text{tot}} = &\sum_i^{\text{occ}} n_i \int d\mathbf{r} \phi_i^*(\mathbf{r}) \left\{ -\frac{\nabla^2}{2} + V_{\text{ext}}(\mathbf{r}) + \frac{1}{2} \int d\mathbf{r}' \frac{n(\mathbf{r}')}{|\mathbf{r} - \mathbf{r}'|} \right\} \phi_i(\mathbf{r}) + E_{\text{XC}}[n(\mathbf{r})] \\ &+ \frac{1}{2} \sum_{a,b}^N \frac{Z_a Z_b}{|\mathbf{R}_a - \mathbf{R}_b|}. \end{aligned} \tag{3.3}$$

The first sum is over Kohn-Sham eigenstates ϕ_i, the second term E_{XC} describes the exchange correlation energy, and the last term accounts for core-core repulsion contributions.

According to the idea of Foulkes and Haydock, the electron density can be expressed as a sum of a reference density $n_0(\mathbf{r})$ and density fluctuations $\delta n(\mathbf{r})$ [70]. Using this, the total energy can be expanded up to second order in these density fluctuations

$$\begin{aligned} E_{\text{tot}} = &\sum_i^{\text{occ}} n_i \int d\mathbf{r} \phi_i^*(\mathbf{r}) \left\{ -\frac{\nabla^2}{2} + V_{\text{ext}}(\mathbf{r}) + \int d\mathbf{r}' \frac{n_0'(\mathbf{r}')}{|\mathbf{r} - \mathbf{r}'|} + V_{\text{XC}}[n_0(\mathbf{r})] \right\} \phi_i(\mathbf{r}) \\ &- \frac{1}{2} \int \int d\mathbf{r} d\mathbf{r}' \frac{n_0'(\mathbf{r}')(n_0(\mathbf{r}) + \delta n)}{|\mathbf{r} - \mathbf{r}'|} - \int d\mathbf{r} V_{\text{XC}}[n_0(\mathbf{r})](n_0(\mathbf{r}) + \delta n) \\ &+ \frac{1}{2} \int \int d\mathbf{r} d\mathbf{r}' \frac{\delta n'(n_0(\mathbf{r}) + \delta n)}{|\mathbf{r} - \mathbf{r}'|} + E_{\text{XC}}[n_0(\mathbf{r}) + \delta n] + \frac{1}{2} \sum_{a,b}^N \frac{Z_a Z_b}{|\mathbf{R}_a - \mathbf{R}_b|}. \end{aligned} \tag{3.4}$$

Here, the second term accounts for double counting contributions, the third term for exchange-correlation contributions, and the fourth term describes a Hartree energy with respect to n_0 and δn. This can be summarized as follows

$$E_{\text{tot}} = E_{\text{BS}}[n_0] + E_{\text{Rep}}[n_0] + E_{\text{2nd}}[n_0, \delta n^2]. \tag{3.5}$$

The first so-called band structure term E_{BS} describes the occupied Kohn-Sham energies, as mentioned above and only depends on the reference density n_0

$$E_{\text{BS}}[n_0] = \sum_i^N n_i \int d\mathbf{r} \phi_i^*(\mathbf{r}) \left\{ -\frac{\nabla^2}{2} + V_{\text{ext}}(\mathbf{r}) + \int d\mathbf{r}' \frac{n_0'}{|\mathbf{r} - \mathbf{r}'|} + V_{\text{XC}}[n_0] \right\} \phi_i(\mathbf{r}). \tag{3.6}$$

The middle term E_{Rep} corresponds to a repulsive energy contribution as in a regular tight-binding scheme [71]

$$E_{Rep}[n_0] = -\frac{1}{2}\int\int d\mathbf{r}d\mathbf{r}'\frac{n_0 n_0'}{|\mathbf{r}-\mathbf{r}'|} - \int d\mathbf{r}V_{\mathrm{XC}}[n_0]n_0 + E_{\mathrm{XC}}[n_0] + \frac{1}{2}\sum_{a,b}^{N}\frac{Z_a Z_b}{|\mathbf{R}_a - \mathbf{R}_b|}. \tag{3.7}$$

$E_{2\mathrm{nd}}$ is the only contribution containing second-order terms in the density fluctuations. This term plays an important role in the case of heteronuclear molecules and polar semiconductors, where the bonding is significantly affected by long-range Coulomb interactions and charge transfer processes and is subject in a self-consistent treatment of DFTB

$$E_{2\mathrm{nd}}[n_0, \delta n^2] = \frac{1}{2}\int\int d\mathbf{r}d\mathbf{r}'\left\{\frac{1}{|\mathbf{r}-\mathbf{r}'|} + \frac{\delta^2 E_{\mathrm{XC}}}{\delta n \delta n'}\Big|_{n_0}\right\}\delta n(\mathbf{r})\delta n(\mathbf{r}'). \tag{3.8}$$

3.2 Approximations in DFTB

In order to achieve its computational speed and efficiency, a number of approximations are made within the DFTB method. The general idea is to avoid the computational most time-consuming parts of the calculations by establishing prepared sets for the interactions between different elements. These preparatory calculations can be done for every homo- and heteronucleic combination of two elements and then be used for every DFTB calculations by just reading the values from the resulting tables. This section will cover the main approximations, which are done in the DFTB approach starting at the total energy expression in Eq. (3.5).

3.2.1 Pseudo atomic density

The reference density n_0 in the DFTB method is chosen as a superposition of single atom densities

$$n_0(\mathbf{r}) = \sum_a n_0^a(\mathbf{r} - \mathbf{R}_a). \tag{3.9}$$

Since the density of a free atom is diffuse and thus not suited to properly describe the real situation in a compound system of many atoms or molecules, compressed densities are used, because they simulate the effects of neighbouring atoms more accurately, resulting in the description of pseudo-atoms [72]. Their densities are obtained via self-consistent LDA or GGA DFT calculations. The pseudo-atoms

are confined in space according to the following modified Kohn-Sham equation

$$\left\{-\frac{1}{2}\nabla^2 + V_{\text{eff}}[n_0^a] + \left(\frac{r}{r_0}\right)^m\right\}\phi_\nu(\mathbf{r}) = \varepsilon_\nu \Phi_\nu(\mathbf{r}) \tag{3.10}$$

with

$$V_{\text{eff}}[n_0^a] = -\frac{Z}{r} + V_{\text{H}}[n_0^a] + V_{\text{XC}}[n_0^a]. \tag{3.11}$$

The term $(\frac{r}{r_0})^m$ represents a confinement potential to strengthen the localization of the atomic orbitals. Although it was shown that the exponent m influences the results only weakly, it can still be varied in order to obtain more accurate results [73]. Nowadays $m = 2$ is mostly used, following the initial formulation of the method. The compression value r_0 can technically be obtained by applying variational principles. The pseudo-atomic orbitals ϕ_ν form a minimal LCAO basis and are constructed by employing Slater-type atomic orbitals

$$\phi_\nu(\mathbf{r}) = \sum_{i=1}^{n_i}\sum_{j=0}^{n_j} a_{ij} r^{l+j} e^{-\alpha_i r} Y_{lm}\left(\frac{\mathbf{r}}{r}\right) \tag{3.12}$$

with l and m denoting their angular momentum and magnetic quantum number, respectively. Using a minimal basis means that only valence orbitals are considered, which reduces the computational effort.

Over the years different schemes have been used for the calculation of the density and the potential to calculate the atomic orbitals. In the original formulation, Seifert used the self-consistent potential of the free atom, Porezag later used the self-consistent potential of the confined atom. Shortly after that, Elstner proposed to use weakly compressed densities with a density compression radius r_0^n. While the first two schemes use only a small amount of variables and are therefore easier to apply to atomic systems, the latter provides the possibility to describe desired properties more accurately, despite introducing an additional variable, which is debatable from a theoretical point of view.

3.2.2 Hamiltonian and overlap matrices

Using the atomic orbitals ϕ_ν described above, Kohn-Sham-like wavefunctions can be constructed

$$\Phi_i(\mathbf{r}) = \sum_{\nu=1}^{N} C_{i\nu}\phi_\nu(\mathbf{r} - \mathbf{R}_a). \tag{3.13}$$

The corresponding Schrödinger equation reads

$$H\Phi_i(\mathbf{r}) = \sum_{\nu=1}^{N} C_{i\nu} \left\{ -\frac{1}{2}\nabla^2 + V_{\text{eff}}[n_0, \mathbf{r}] \right\} \phi_\nu(\mathbf{r}) = \varepsilon_i \sum_{\nu=1}^{N} C_{i\nu}\phi_\nu(\mathbf{r}). \tag{3.14}$$

Multiplying with ϕ_μ^* and integrating yield the Hamiltonian and non-orthogonal overlap matrix elements $h^0_{\mu\nu}$ and $s_{\mu\nu}$, respectively

$$\begin{aligned} h^0_{\mu\nu} &= \int d\mathbf{r}\phi_\mu^*(\mathbf{r}) H \phi_\nu \\ s_{\mu\nu} &= \int d\mathbf{r}\phi_\mu^*(\mathbf{r})\phi_\nu \end{aligned} \tag{3.15}$$

with the corresponding secular equation

$$\sum_{\nu=1} C_{i\nu} \left(h^0_{\mu\nu} - \varepsilon_i s_{\mu\nu} \right) = 0, \;\; \forall i, \mu. \tag{3.16}$$

A symmetry evaluation of these integrals simplifies the problem significantly. Only ten two-center interactions are not equal to zero, if no f-orbitals are considered. In the case of f-orbitals, twenty integrals remain. This is achieved by decomposing the effective potential V_{eff} into atomic-like contributions, either by potential superposition (I) or by density superposition (II)

$$V_{\text{eff}}[n_0, \mathbf{r}] = \begin{cases} \sum_c V_c^0[n_0^c, \mathbf{r}_c], & I \\ V_{\text{eff}}(\sum_c n_c^0(\mathbf{r}_c)), & II \end{cases}. \tag{3.17}$$

Both parametrizations presented in Chapter 7 use the density superposition, although both approaches are still being used nowadays.

In practice, only the densities of atoms at which the atomic orbitals ϕ_μ and ϕ_ν are located, will contribute to the effective potential in the Hamiltonian H and consequently to the calculation of the Hamiltonian matrix elements. With a, b denoting orbital centers, c denoting the potential center, and basis functions $\mu \in a$, $\nu \in b$, the integrals in Eq. (3.15) can be categorized as presented in Table 3.1

Category	Centers	Included
Onsite terms	$a = b = c$	Yes
Two-center terms	$a \neq b, c = a$ or $c = b$	Yes
Three-center terms	$a \neq b \neq c$	No
Crystal-field terms	$a = b \neq c$	No

TABLE 3.1: Categories of integrals contributing to the Hamiltonian matrix elements $h^0_{\mu\nu}$.

Neglecting the three-center terms in particular provides a significant simplification and thus saves a lot of computational effort. In contrast, the crystal-field terms technically could actually improve the simulation results at moderate computational costs, but due to the nature of the theory, there is considerable error cancellation involved and both neglections have to appear simultaneously. The mathematical formalism behind this is quite complex and is therefore not derived here. Nevertheless, it can be found in [69, 74].

These approximations finally allow the evaluation of the Hamiltonian matrix elements $h^0_{\mu\nu}$

$$h^0_{\mu\nu} = \begin{cases} \varepsilon_\mu^{\text{free atom}}, & \mu = \nu \\ \int d\mathbf{r}\phi^*_\mu(\mathbf{r})(T + V_{\text{eff}}[n^0_a + n^0_b])\phi_\nu, & \mu \in a, \nu \in b \\ 0, & \text{otherwise.} \end{cases} \tag{3.18}$$

If one considers orbitals up to d, the remaining contributions to the integrals are

$$dd^\sigma, dd^\pi, dd^\delta, pd^\sigma, pd^\pi, pp^\sigma, pp^\pi, sd^\sigma, sp^\sigma, ss^\sigma. \tag{3.19}$$

The Hamiltonian and overlap matrix elements are calculated with respect to the inter-atomic distance between the corresponding atoms and finally tabulated in so-called Slater-Koster files (sk-files). Therefore, no integrals have to be evaluated during a DFTB calculation, ultimately speeding up the process tremendously.

3.2.3 Repulsive potential

The previous section described a scheme to calculate the electronic part of the DFTB total energy E_{BS} according to Eq. (3.6). The next step is finding an appropriate way to calculate the repulsive part E_{Rep} of the total energy according to Eq. (3.7). With the definition of the reference electron density n_0 as a superposition of atomic neutral electron densities, there is no dependency on charge fluctuations or long-range Coulomb-interaction involved in E_{Rep}. This leads to the possibility to neglect three-center electron-electron contributions, since they cancel each other out with nucleus-nucleus interaction terms. Thus, E_{Rep} can be approximated by a sum of two-center terms and expanded into a cluster series [70]

$$E_{\text{Rep}}[n_0] = \sum_a E_{\text{Rep}}[n^a_0] + \frac{1}{2}\sum_a \sum_{a\neq b} \left\{ E_{\text{Rep}}[n^a_0 + n^b_0] - E_{\text{Rep}}[n^a_0] - E_{\text{Rep}}[n^b_0] \right\} + \dots . \tag{3.20}$$

In this formulation, E_{Rep} would not vanish for large interatomic distances $\mathbf{R}_{ab} = \mathbf{R}_b - \mathbf{R}_a$, but rather approach a constant value

$$E_{\text{Rep}}[n_0] = \sum_a E_{\text{Rep}}[n_0^a], \quad \mathbf{R}_{ab} \to \infty. \tag{3.21}$$

This is unphysical, since there should be no apparent repulsive interaction in the dissociation limit, so as a consequence the monomer contributions are included in the atomic orbital energies ε_i and the repulsive energy can be approximated as the sum of short-ranged two-center terms

$$E_{\text{Rep}}[n_0] = E_{\text{Rep}}[n_0] - \sum_a E_{\text{Rep}}[n_0^a] = \frac{1}{2}\sum_{ab} V[n_0^a, n_0^b]. \tag{3.22}$$

The repulsive energy part can be determined as the difference between the electronic energy part E_{BS} and the total energy resulting from a full LDA/GGA DFT calculation and be written as a function of the interatomic distance between two atoms

$$E_{\text{Rep}}(|\mathbf{R}_{ab}|) = E_{\text{Rep}}(R_{ab}) = E_{\text{DFT}}^{\text{tot}}(\mathbf{R}_b) - E_{\text{BS}}(\mathbf{R}_b) = \frac{1}{2}\sum_a \sum_{b\neq a} V_{\text{Rep}}^{ab}(R_{ab}). \tag{3.23}$$

In practice, depending on the desired system to investigate, this short-range pair potential is fitted to a dimer or a preferably simple crystalline system and represented mathematically by a polynomial of the following form

$$V_{\text{Rep}}(r) = \begin{cases} \sum_i a_i (r_c - r)^i, & r < rc \\ 0, & \text{otherwise} \end{cases}. \tag{3.24}$$

r_c denotes the cutoff radius and is typically chosen between 1.5 and 2 times the equilibrium bond length. Beyond that the repulsive interaction vanishes. A more detailed overview on how to generate the repulsive part will be given in Chapter 7 for the examples of HfO_2 and GaN.

3.2.4 Second-order corrections

Finally the second-order correction term needs to be discussed. Whenever a representation of the electron density as a sum of atomic electron densities is no longer a justified approximation, this term needs to be considered in order to obtain reliable results. Consistent with the aforementioned derivation of the DFTB scheme, the density fluctuations $\delta n(\mathbf{r})$ are decomposed into atomic contributions, which decay quickly with an increasing distance from their respective centers.

Combining this with Eq. (3.8) yields

$$E_{2\mathrm{nd}}[n_0, \delta n] = \frac{1}{2}\sum_{a,b}\int\int d\mathbf{r}d\mathbf{r}' \left\{ \frac{1}{|\mathbf{r}-\mathbf{r}'|} + \frac{\delta^2 E_{\mathrm{XC}}}{\delta n \delta n'}\Big|_{n_0} \right\} \delta n_a(\mathbf{r})\delta n_b(\mathbf{r}'). \tag{3.25}$$

Next, the atomic density fluctuations are expanded into a sum of radial and angular parts

$$\delta n_a(\mathbf{r}) = \sum_{l,m} c^a_{lm} F^a_{lm}(|\mathbf{r}-\mathbf{R}_a|) Y_{lm}\left(\frac{\mathbf{r}-\mathbf{R}_a}{|\mathbf{r}-\mathbf{R}_a|}\right) \approx \Delta q_a F^a_{00}(|\mathbf{r}-\mathbf{R}_a|) Y_{00}. \tag{3.26}$$

This multipole expansion is truncated after the monopole term as a compromise between accuracy and complexity. F^a_{lm} describes the normalized radial dependence of the density fluctuations at atom a. Finally, considering the charge preservation $\sum_a \Delta q_a = \int d\mathbf{r}\delta n(\mathbf{r})$ with $\Delta q_a = q_a - q^0_a$ describing a point charge, the final expression for the second-order correction term reads

$$E_{2\mathrm{nd}} = \frac{1}{2}\sum_{a,b}^{N} \Delta q_a \Delta q_b \gamma_{ab} \tag{3.27}$$

with

$$\gamma_{ab} = \int\int d\mathbf{r}d\mathbf{r}' \frac{1}{4\pi}\left[\frac{1}{|\mathbf{r}-\mathbf{r}'|} + \frac{\delta^2 E_{\mathrm{XC}}}{\delta n \delta n'}\right]_{n_0} F^a_{00}(|\mathbf{r}-\mathbf{R}_a|) F^b_{00}(|\mathbf{r}-\mathbf{R}_b|). \tag{3.28}$$

In the case of different atom centers $a \neq b$ the Coulomb interaction of their respective charge distributions determines γ_{ab} [75]. In the limit $a = b$, where no Coulomb interaction is to consider, correlation effects become important and need to be appropriately represented in the formalism. Consequently γ_{aa} is approximated by the Hubbard parameter of atom a, which is related to the chemical hardness η_a. The Hubbard parameter basically describes the difference between the ionisation potential and the electron affinity of the atom [76]. It is defined as the second derivative of the total atomic energy with respect to the atom's charge

$$\gamma_{aa} = U_a = 2\eta_a = \frac{\partial^2 E^{\mathrm{at}}_{\mathrm{tot}}}{\partial q^2_a}. \tag{3.29}$$

A possible interpretation of this result is the presence of highly localized wavefunctions for elements with a high chemical hardness. The latter is usually obtained from a self-consistent DFT calculation. Using Janak's theorem [36], this expression can be rewritten as the first derivative of the highest occupied orbital

energy with respect to its occupation number

$$\gamma_{aa} = U_a = \frac{\partial \varepsilon_a^{\mathrm{HOMO}}}{\partial n_a^{\mathrm{HOMO}}}. \tag{3.30}$$

In contrast, for large interatomic distances, γ_{ab} describes the Coulomb interaction between two point charges Δq_a and Δq_b. Since γ_{ab} is only dependent on the interatomic distance and the Hubbard parameters, it is an intrinsic parameter and not empirical. Putting everything together, the SCC-DFTB total energy looks as follows

$$E_{\mathrm{tot}}^{\mathrm{DFTB}} = \sum_i \int d\mathbf{r} \phi_i^*(\mathbf{r}) H \phi_i(\mathbf{r}) + \frac{1}{2} \sum_{a,b} \gamma_{ab} \Delta q_a \Delta q_b + \sum_{a \neq b} V_{\mathrm{Rep}}^{ab}(R_{ab}). \tag{3.31}$$

Chapter 4

Molecular dynamics

Molecular dynamics (MD) is one of the principal tools in the theoretical study of biomolecules, chemical physics and materials science. Originally developed in the late 1950s by Alder and Wainwright and applied to five hundred atoms, nowadays it allows the simulation of up to hundreds of thousands of particles [23]. In contrast to DFT, atoms are treated as classical particles in MD. The trajectory of each atom is determined by solving Newton's laws of motion to study the dynamical evolution of the whole system over time. Therefore, the atoms are allowed to interact with each other for a specific amount of time (typically no more than a few femtoseconds). These interactions are determined by using force-field methods, semi-empirical methods or ab-initio approaches. Due to the increased computational complexity, the latter does not allow the same system sizes in MD simulations, although with steadily increasing computational resources, it gained more relevance over the past years.

4.1 Dynamics of an atomistic system

The foundation of MD is Newtonian mechanics. The goal is a numerical, step-by-step solution of Newton's equations of motion, which can be written as follows

$$m_i \frac{\partial^2 \mathbf{r}_i}{\partial t^2} = \mathbf{F}_i, \quad \mathbf{F}_i = -\frac{\partial U\{\mathbf{r}_i\}}{\partial \mathbf{r}_i}, \tag{4.1}$$

where m_i denotes the mass of an atom i, $\mathbf{F}_i$ the applied force, and $U\{\mathbf{r}_i\}$ the potential energy. $\mathbf{r}_{i}{}_{i=1}^{N}$ represents the 3N atomic coordinates. For solving this second-order differential equation a numerical algorithm needs to be employed in order to get access to the exact positions $\mathbf{r}_i$ and velocities $\mathbf{v}_i$ of an atom i. In 1967 the Verlet algorithm was introduced [77], which turned out to be very successful for MD calculations, because it is simple to implement, time-reversible, fairly accurate (error of the order Δt^4) and stable. It can be derived easily by Taylor expanding the position $r(t)$ up to third order twice, once forward and once backward in time. With Δt as one time step, v as the first, a as the second, and b as the third

derivative of r with respect to the time t, the Taylor expansions read

$$r(t+\Delta t) = r(t) + v(t)\Delta t + \frac{1}{2}a(t)\Delta t^2 + \frac{1}{6}b(t)\Delta t^3 + O(\Delta t^4) \tag{4.2}$$

$$r(t-\Delta t) = r(t) - v(t)\Delta t + \frac{1}{2}a(t)\Delta t^2 - \frac{1}{6}b(t)\Delta t^3 + O(\Delta t^4). \tag{4.3}$$

Adding Eqs. (4.2) and (4.3) yields the basic form of the Verlet algorithm

$$r(t+\Delta t) = 2r(t) - r(t-\Delta t) + a(t)\Delta t^2 + O(\Delta t^4). \tag{4.4}$$

A similar expression can be derived for the velocities v(t)

$$v(t) = \frac{r(t+\Delta t) - r(t-\Delta t)}{2\Delta t} + O(\Delta t^2) \tag{4.5}$$

with $a(t) = -\frac{F(t)}{m}$.

However, one huge disadvantage of this original Verlet algorithm is the fact that it is not self-starting. To calculate $r(0)$, $r(-\Delta t)$ is needed, which is an unknown value that needs to be guessed. Another problem is the accuracy of the velocity integration, which is just of the order Δt^2. A possible approach to overcome these drawbacks is the Velocity-Verlet algorithm [78]. Writing the following Taylor expansions for $r(t)$ and $v(t)$

$$r(t+\Delta t) = r(t) + v(t)\Delta t + \frac{1}{2}a(t)\Delta t^2 \tag{4.6}$$

$$v(t+\frac{1}{2}\Delta t) = v(t) + \frac{1}{2}a(t)\Delta t \tag{4.7}$$

$$v(t+\Delta t) = v(t+\frac{1}{2}\Delta t) + \frac{1}{2}a(t+\Delta t)\Delta t \tag{4.8}$$

with $a(t+\Delta t) = -\frac{F(t+\Delta t)}{m}$ leads to the velocity form of the Verlet algorithm by plugging Eq. (4.7) into Eq. (4.8)

$$\begin{aligned} r(t+\Delta t) &= r(t) + v(t)\Delta t + \frac{1}{2}a(t)\Delta t^2 \\ v(t+\Delta t) &= v(t) + \frac{1}{2}(a(t) + a(t+\Delta t))\Delta t. \end{aligned} \tag{4.9}$$

In this formulation, all mentioned disadvantages of the basic Verlet form are avoided. Due to this, the Velocity Verlet algorithm was employed for the MD

calculations in Chapter 7.

4.2 Statistical ensembles

MD simulations acquire results such as atomic positions or velocities at the microscopic level with the goal to connect them to macroscopic observables. These observables are for example the total number of atoms N, the temperature T or the total energy E. This desired connection between the microscopic world of the atoms and the macroscopic properties of the system requires statistical physics. Within statistical physics, there are a few important concepts, which will be introduced below.

- The *microscopic state* of a system describes its complete set of positions $\mathbf{r}_i$ and velocities $\mathbf{v}_i$ at any given time t. Or in terms of a phase space formulation, it specifies the exact phase space vector $\Gamma = \{\mathbf{r}_i(t), \mathbf{v}_i(t)\}_{i=1}^{N}$.
- The *macroscopic state* of a system is defined by a macroscopic observable like the temperature T or pressure P.
- An *ensemble* is a set of all possible systems with different microscopic states, but the same macroscopic state.

There are different types of ensembles, which are usually characterized by the macroscopic states, which are kept fixed. A few examples are

- A *microcanonical ensemble* describes an isolated system, which cannot exchange particles or energy with its surroundings. Since the volume is also kept constant, it is typically referred to as *NVE-ensemble*.
- A *canonical ensemble* describes a system, which is in contact with a heat bath at constant temperature, which allows energy exchange. Since every virtual copy of this system will have the temperature T of the heat bath, it is usually referred to as *NVT-ensemble*. This type of ensemble will be employed during the MD simulations in Chapter 7.
- A *grandcanonical ensemble* describes a system, which is in contact with a heat and a particle bath, so it can exchange energy and particles. For example a liquid in contact with its vapor in equilibrium. Since both the system and the head and particle bath are in equilibrium, the chemical potential is the same for both. In consequence this type of ensemble is also referred to as *μVT-ensemble*.

In order to link macroscopic observables A to real measurements in an experiment, the so-called ensemble average needs to be considered, since MD simulations can only calculate time averages, whereas macroscopic observables are ensemble averages. The ensemble average is defined as follows

$$< A >= \frac{1}{Z} \int d\Gamma A(\Gamma)\rho(\Gamma), \tag{4.10}$$

where $\rho = e^{-H(\Gamma)}$ is the phase space density and $Z = \int d\Gamma \rho(\Gamma)$ the partition function. This leads to one of the fundamental principles of MD, the ergodic hypothesis [79]. It states that the time average of a macroscopic observable A and its ensemble average are the same, allowing the formulation of the following equation

$$\bar{A}^t =< A > . \tag{4.11}$$

The idea behind this is that if the system evolves in time indefinitely, every point in the phase space will have been passed through eventually. As a consequence, only those systems can be considered as ergodic, in which every point in the phase space can be reached. However, formally proving ergodicity for a given system is not straightforward, but most systems in MD are treated as ergodic systems, since the results justify this.

4.3 Thermostats - Controlling the temperature

In 1827, Robert Brown investigated the movement of pollen in water and noticed that the pollen moved in an apparently random manner. This Brownian Motion was later explained theoretically by Einstein in 1905 and served as evidence that atoms and molecules exist [80, 81]. it is also referred to as a random walk, which seems to be enhanced when the system is exposed to heat. MD makes use of this relation between the dynamics of the atoms and the applied temperature by employing so-called thermostats. Thermostats can be used to monitor and actively control the temperature in an atomic system. In kinetic theory, each particle has three translative degrees of freedom. According to the equipartition theorem, each of these degrees of freedom has an average kinetic energy of $\frac{1}{2}k_{\mathrm{B}}T$ with k_{B} as the Boltzmann-constant as T denoting the temperature of the system. Using the kinetic energy for a N-atom system, this allows to connect the velocity $\mathbf{v}_i = \frac{\partial \mathbf{r}_i}{\partial t}$ to the temperature T

$$\frac{3}{2}Nk_{\mathrm{B}}T = \langle \sum_{i=1}^{3N} \frac{m_i}{2}\mathbf{v}_i^2 \rangle. \tag{4.12}$$

with T reading

$$T = \frac{2}{3Nk_\mathrm{B}} \langle \sum_{i=1}^{3N} \frac{m_i}{2} \mathbf{v}_i^2 \rangle. \tag{4.13}$$

This average is an ensemble average. Using the aforementioned ergodic hypothesis, we can express the temperature T in terms of the velocities' time average.

$$T = \frac{2}{3Nk_\mathrm{B}} \overline{\sum_{i=1}^{3N} \frac{m_i}{2} v_i^2}^t \tag{4.14}$$

If one is just interested in the momentary temperature, the time average can be neglected and the temperature can be calculated. Furthermore, the temperature can also be controlled and adjusted during the calculation by rescaling the velocities of the atoms with a specific scaling factor after a few simulation steps according to Eq. (4.5)

$$v_i' = \sqrt{\frac{T_0}{T}} v_i, \tag{4.15}$$

where v_i is the momentary velocity, v_i' is the rescaled velocity, T is the momentary temperature, and T_0 is the desired temperature. In practice, this is often used for equilibrating a system, where a new set of velocities and thus a new temperature is generated in each step of the MD run. However, this approach to control the temperature is not consistent with a canonical ensemble, because the momentary temperature fluctuates and forcing it to a specific value disturbs the system.

A more sophisticated way to monitor and control the temperature are thermostats. Instead of rescaling the temperature in a discrete way after a specific amount of simulation steps, they monitor the control in a continuous way.

4.3.1 Nose-Hoover thermostat

One possible and widely employed option is the Nose-Hoover thermostat, introduced by Nose in 1984 [82]. He proposed the introduction of an additional degree of freedom s, which represents the heat bath, that can exchange heat with the physical system. s can also be seen as a scaling factor of the physical time t

$$dt = sdt', \tag{4.16}$$

where t is the real time and t' is a virtual time. As a consequence , dependent on the value of s, the kinetic energy will either increase ($s < 1$) or decrease ($s > 1$). Using this, the Lagrangian of the extended system, consisting of the physical

system and the heat bath, is written as follows

$$L = \sum_{i=1}^{N} \frac{1}{2} m_i s^2 \dot{\mathbf{r}}_i^2 - \Phi(\mathbf{r}) + \frac{1}{2} Q \dot{s}^2 - (3N+1) k_B T_0 \ln(s). \tag{4.17}$$

Here, Q is a fictious effective mass associated with the heat bath, while $\frac{1}{2}Q\dot{s}^2$ and $(3N+1)k_B T_0 \ln(s)$ are the corresponding kinetic and potential energies, respectively. Q controls how strongly both systems are coupled and $3N+1$ is the total number of degrees of freedom, limiting this derivation to the description of atoms, but the transfer to molecules is straightforward. Applying the Euler-Lagrange equations

$$\frac{d}{dt}\left(\frac{\partial L}{\partial \dot{A}}\right) = \frac{\partial L}{\partial A}, \tag{4.18}$$

with A representing one of the variables, deriving the Nose equations of motion for $\mathbf{r}$ and s is straightforward

$$\ddot{\mathbf{r}}_i = \frac{\mathbf{F}_i}{m_i s^2} - \frac{2\dot{s}}{s}\dot{\mathbf{r}}_i, \qquad Q\ddot{s} = \sum_{i=1}^{N} m_i s \dot{\mathbf{r}}_i - \frac{(3N+1)k_B T_0}{s}. \tag{4.19}$$

They sample a microcanonical ensemble in the extended system, however, it can be shown that they sample a canonical ensemble in the real system [82]. In practice, it is easier to work with real time steps, since sampling a trajectory at uneven time steps is impractical. Consequently the Nose equations are expressed with respect to the real time t. Introducing $\gamma = \frac{\dot{s}}{s}$, the Nose equations look as follows

$$\ddot{\mathbf{r}}_i = -\frac{\mathbf{F}_i}{m_i} - \gamma \mathbf{r}_i, \qquad \frac{1}{2}Q\dot{\gamma} = \frac{1}{2}\sum_{i=1}^{N} m_i \dot{\mathbf{r}}_i^2 - \frac{1}{2}(3N+1)k_B T_0. \tag{4.20}$$

The role of γ can be seen as an artificial friction, which causes the particles to decelerate or to accelerate, depending on the value for Q, the coupling strength. If the first term (momentary kinetic energy) in the equation for γ is larger than the second one (desired kinetic energy), it will force the particles to decelerate to match the desired kinetic energy and ultimately the desired temperature. Choosing a proper value for Q is challenging, since too large values (weak coupling) will result in poor temperature monitoring and temperature oscillations, while very low values (strong coupling) will unnecessarily extend the time, the system needs to reach a canonical distribution.

4.3.2 Andersen thermostat

Another popular and simple thermostat, which correctly samples a canonical ensemble, is the Andersen thermostat [83]. The energy of a given system at constant temperature fluctuates, because of the above discussed Brownian motion. To account for that, Andersen introduced stochastic forces to influence the kinetic energy of the particles in a given system. This will mimic random collisions with heat bath particles at a certain temperature T. The resulting new velocity of an affected particle will be chosen according to the Maxwell-Boltzmann distribution

$$P(v_{x,i}) = \sqrt{\frac{m_i}{2\pi k_\mathrm{B} T}} e^{-\frac{m_i v_{x,i}^2}{2k_\mathrm{B} T}}. \tag{4.21}$$

This procedure will be applied to each velocity component separately. Similar to the above described derivation of the Nose equations of motions, equations of motions can be obtained for the Andersen case. Consequently, the system evolves according to

$$\dot{\mathbf{r}}_i = \mathbf{v}_i, \qquad \dot{\mathbf{v}}_i = -\nabla_{\mathbf{r}_i} U, \tag{4.22}$$

where U is the interatomic potential. In practice, a so-called collision frequency ν is introduced. It determines how strongly the system is coupled to the heat bath. The time intervals between successive collisions are distributed according to a Poisson distribution

$$P(t) = \nu e^{-\nu t}, \tag{4.23}$$

with $P(t)\Delta t$ describing the probability that a chosen time interval between collisions is between t and $t + \Delta t$. A proper value for Δt is chosen prior to the simulation. An alternative way to determine which particles are affected uses random numbers. Here, a random number a_i between 0 and 1 is selected for the i-th particle. This is done for each particle in the system. If $a_i < \nu \Delta t$, the velocity of the i-th particle will be updated according to Eq. (4.11). Although the Andersen thermostat samples a canonical ensemble correctly, it has shortcomings. Due to the random reassignment of the velocities, within this scheme momenta are not preserved. As a consequence, certain values such as diffusion constants or viscosities cannot be calculated reliably. Nevertheless because of its simplicity and ability to sample a canonical ensemble, it is employed for the MD calculations in Chapter 7.

4.4 Static correlation functions

Static correlation functions provide a way to obtain detailed information on the structure of an atomic system. They are often employed for the description of distance relations in amorphous structures. First, particle densities need to be introduced. Besides an average density $n_0 = \frac{N}{V}$, one-particle and two-particle densities $\nu^{(1)}$ and $\nu^{(1)}$ can be expressed as follows

$$\nu^{(1)}(\mathbf{r}) = \sum_{i=1}^{N} \delta(\mathbf{r} - \mathbf{R}_i), \quad \int d\mathbf{r}\nu^{(1)}(\mathbf{r}) = N \tag{4.24}$$

$$\nu^{(2)}(\mathbf{r}_1, \mathbf{r}_2) = \sum_{i=1}^{N} \sum_{i \neq j}^{N} \delta(\mathbf{r}_1 - \mathbf{R}_i)\delta(\mathbf{r}_2 - \mathbf{R}_j), \quad \int \int d\mathbf{r}_1 d\mathbf{r}_2 \nu(\mathbf{r}_1, \mathbf{r}_2) = N(N-1). \tag{4.25}$$

The construction of a N-particle density is straightforward. Due to thermal fluctuations in a given atomic system of interest, thermodynamic average values need to be considered. They provide access to the one-particle and two-particle distribution functions

$$n^{(1)}(\mathbf{r}) = < \nu^{(1)}(\mathbf{r}) > \tag{4.26}$$

$$n^{(2)}(\mathbf{r}_1, \mathbf{r}_2) = < \nu^{(2)}(\mathbf{r}_1, \mathbf{r}_2) > . \tag{4.27}$$

Here, $d\mathbf{r}n^{(1)}(\mathbf{r})$ denotes the probability to find a particle in a volume element $d\mathbf{r}$ around $\mathbf{r}$. Analogously, $d\mathbf{r}_1 d\mathbf{r}_2 n^{(2)}(\mathbf{r}_1, \mathbf{r}_2)$ denotes the probabilities to find two particles at the same time in the volume elements $d\mathbf{r}_1$ and $d\mathbf{r}_2$ around $\mathbf{r}_1$ and $\mathbf{r}_2$. Using these definitions, the pair distribution function can be formulated as follows

$$g^{(2)}(\mathbf{r}_1, \mathbf{r}_2) = \frac{n^{(2)}(\mathbf{r}_1, \mathbf{r}_2)}{n^{(1)}(\mathbf{r}_1)n^{(1)}(\mathbf{r}_2)}. \tag{4.28}$$

$g^{(2)}(\mathbf{r}_1, \mathbf{r}_2)$ describes the probability to find a particle at $\mathbf{r}_2$ in the presence of another particle at $\mathbf{r}_1$.

Since amorphous systems are generally discussed as being homogeneous and isotropic, the following assumptions can be employed

$$n^{(1)} = n^{(2)} = n_0, \quad \mathbf{r}_1 - \mathbf{r}_2 \to \mathbf{r}, \quad \mathbf{r} \to r. \tag{4.29}$$

Consequently, the following expression for $g^{(2)} = g$ results

$$g(r) = \frac{V}{4\pi N^2 r^2} < \sum_{i=1}^{N} \sum_{i \neq j}^{N} \delta(r - r_{ij}) > . \tag{4.30}$$

This derivation is valid for homonucleic systems, in case of a heteronucleic system, the total pair distribution function $g(r)$ as a weighted sum of partial pair distribution functions $g_{\alpha\beta}$ needs to be considered

$$g(r) = \frac{1}{\langle b^2 \rangle} \sum_{\alpha,\beta} c_\alpha b_\alpha c_\beta b_\beta g_{\alpha\beta}(r), \quad \langle b^2 \rangle = (\sum_{\alpha} c_\alpha b_\alpha)^2. \tag{4.31}$$

$c_{\alpha,\beta}$ denotes the concentration of the respective element and $b_{\alpha,\beta}$ is the corresponding scattering length. Unfortunately, the pair distribution function can only be obtained during computational calculations, but not directly measured in experiments. However, the so-called structure factor $S(k)$ can be measured directly and thus provides access to comparisons with experimental findings for electron, x-ray or neutron scattering. It basically described the intensity distribution on a detector in scattering experiments of crystalline or amorphous structures. Using the pair distribution function $g(r)$, $S(k)$ reads in reciprocal space

$$S(k) = 1 + 2\pi n_0 \int_0^\infty dr g(r) r^2 \mathrm{sinc}(kr). \tag{4.32}$$

Chapter 5

Functionalization of ZnO/GaN

Scientific interest in hybrid nanostructures made of organic and inorganic materials for applications in electronic and optoelectronics has grown over the past years. Surface functionalization is a possible way to modify electronic and optical properties of nanostructures. This Chapter will present the results of surface functionalizations of zinc oxide (ZnO) and gallium nitride (GaN) surfaces.

5.1 ZnO

Zinc oxide is a widely used material for surface functionalization due to a variety of reasons. It is a wide-bandgap semiconductor (3.3 eV) with high absorbance in the UV range, a high electron mobility, and low production costs [84]. Furthermore, it and can be synthesized in many different forms. As introduced in Chapter 1, nanowires are interesting to the scientific community. Due to the large surface-to-volume ratio of ZnO nanowires, surface functionalization is an effective way to enhance their electronic and optical properties, for example for one-dimensional electron transport [85]. In contrast, zero-dimensional nanostructures like colloidal quantum dots possess unique electronic and optical properties such as superior photostability. Another important feature of zero-dimensional nanostructures is a size-dependent band gap, which provides a way to a more efficient absorption across the solar spectrum [86–88]. Recent works corroborate this by suggesting that attaching ligand-capped quantum dots on ZnO surfaces could lead to hybrid solar cells with a high absorption in a broad spectral range [89, 90]. In systems like that, the functional groups serve as a bridge between the surface and the quantum dot.

Over the years, there have been several DFT studies on functionalizing ZnO $(10\bar{1}0)$ surfaces with small functional groups [91–96]. It was shown for example that thiol groups bind strongly to the ZnO $(10\bar{1}0)$ surfaces with a covalent monodentate adsorption mode [95, 97]. Similar investigations were pursued experimentally and corroborated these findings. In particular, molecules consisting of two functional groups bridged by long carbon chains were found to be stable

[98, 99].

Therefore, this section will present a study for mercaptocarboxylic acids (MPA) molecules of the form $SH-(CH_2)_n-COOH$, (n = 1,2,3,7) on ZnO $(10\bar{1}0)$ surfaces. This Section is based on previously published results [100].

5.1.1 Computational details

DFT as implemented in the Vienna ab initio simulation package (VASP) [101–104] was employed for the calculations. The projected augmented wave method (PAW) was used [19, 20] throughout. Atomic structures were optimized on the PBE level [33]. As has been shown in previous studies [105], the PBE functional provides an accurate description of structural properties, however, the electronic structure can be underestimated significantly as discussed in Chapter 2 [40, 42, 62]. To overcome this bandgap problem, the PBE0 hybrid formalism was applied for a more accurate description of the electronic properties. 25 % of Hartree-Fock exchange is added to the PBE functional, ultimately yielding a more reasonable band gap for ZnO [106]. A plane wave basis with an energy cutoff of $E_{cut} = 400\,eV$ was applied. For the geometry optimization, a $(1 \times 4 \times 4)$ Monkhorst-Pack **k**-point sampling was used [21], whereas only the Γ point was considered for the PBE0 calculations.

The independent particle approximation within the PBE0 functional (IPA-PBE0) was employed for the calculation of the dielectric function. In addition TDDFT has been used to partly include excitonic effects to obtain a more accurate dielectric function. Finally the surface models consisted of a (3×2) surface supercell with 96 atoms (48 ZnO units) units and one MPA molecule. Consequently a low coverage regime of 1 molecule/nm^2 was considered in this work.

5.1.2 Structural properties

First, the structural and thermodynamical properties will be discussed. In this work, several different initial configurations have been tested for the MPA molecules on the surfaces. Depending on the initial geometry, two stable optimized geometries were found for every carbon chain length, a monodentate and a bidentate mode. Figure 5.1 displays the ground state geometries for the monodentate and the bidentate binding mode at the top and the bottom, respectively. The monodentate mode is energetically more stable against bidentate and hollow positions. The energy difference ΔE between the ground state total energies of both binding modes decreases with increasing carbon chain length. Therefore, longer chain lengths need to be investigated in order to to see if the monodentate mode remains more stable. For both binding modes, the MPA molecules are adsorbed dissociatively with an adsorption energy E_{ads} of around 1 eV for all chain lengths.

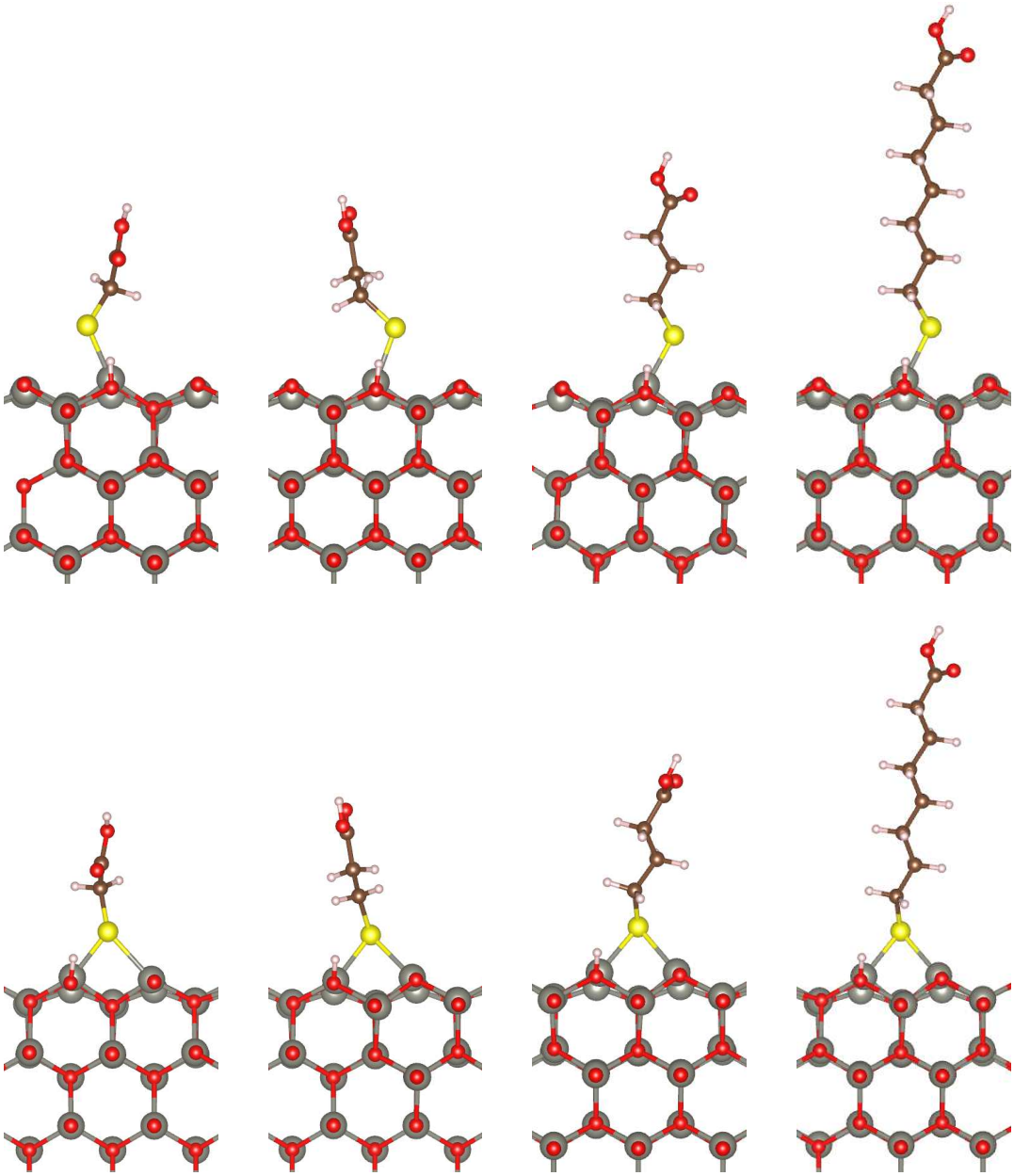

FIGURE 5.1: Optimized structures for the $(10\bar{1}0)$ ZnO surface functionalized with one MPA molecule (SH-$(CH_2)_n$-COOH). The figures at the top correspond to the monodentate binding mode, left to right n = 1, 2, 3, 7. The figures at the bottom correspond to the bidentate binding mode, left to right n = 1, 2, 3, 7. Adapted with permission from [100]. Copyright 2018 American Chemical Society.

The adsorption energy was calculated as the difference between the total energy of the functionalized system and the total energies for the bare surface and an isolated MPA molecule via $E_{ads} = E_{tot}^{MPA/ZnO} - E_{tot}^{bare\ surf} - E_{tot}^{MPA}$. This strong bonding explains, why the Zn-S bond lengths d_{Zn-S} between the outermost zinc atom of the slab and the sulphur atom of the molecule remain almost constant for all

structures. This trend is also observed for the buckling Δz, the relaxation of that outermost Zn atom relative to other Zn atoms of the surface. These results are summarized in Table 5.1.

chain length n	Δ z (Å)	d_{Zn-S}(Å)	Δ E (eV)	E_{ads}(eV)
1	0.28	2.26	-2.20	1.00
2	0.35	2.23	-1.90	1.00
3	0.28	2.26	-1.10	1.10
7	0.28	2.26	-0.70	1.10

TABLE 5.1: Relative outward relaxation of the surface zinc atom Δ z, Zn-S bond length d_{Zn-S}, energy difference Δ E between monodentate and bidentate modes, and adsorption energies E_{ads} of the monodentate mode for SH-$(CH_2)_n$-COOH (n=1,2,3,7) molecules on ZnO $(10\bar{1}0)$ surfaces. Reprinted with permission from [100]. Copyright 2018 American Chemical Society.

5.1.3 Electronic and optical properties

This part will cover the discussion on the electronic properties. Figure 5.2 shows the total and projected density of states (PDOS) for the structures with a monodentate mode. The systems with a bidentate binding mode will not be discussed further, since they are energetically less stable and therefore unlikely to form. The bands were aligned with respect to the electrostatic potential of the vacuum level as derived in [107, 108]. The highest occupied molecular orbital (HOMO) of the bare surface (Fig. 5.2(a)) denotes the zero of the energy axis for all structures. Figures 5.2 (b)-(e) show intra-gap states for all functionalized systems. These states are strongly localized on the S atom of the MPA molecule (red curve) with small hybridization with the ZnO surface and the first methyl groups of the carbon chain. The energy difference between the intra-gap states and the valence band maximum (VBM) remains the same for all carbon chain lengths. This indicates that the interaction between atoms at the top of the slab and the functional group close to it dominates the electronic structure. A look at the band decomposed partial charge density in Fig. 5.3 corroborates this observation. The figures at the top show the HOMO-1 orbitals in SH-$(CH_2)_n$-COOH (left to right, n=1,2,3,7) on the $(10\bar{1}0)$ ZnO surface, whereas the figures at the bottom show the HOMO for these structures. A and B states in the Figs. 5.2 (b)-(e) correspond to the HOMO-1 and HOMO, respectively. The band decomposed partial charge densities clearly show that the charge for both states is mainly localized on the S atom and the first methyl group of the molecule with small contributions from the surface. This confirms the small hybridization seen in Fig. 5.2. All investigated systems show this feature, indicating that the methyl groups play a minor role in charge transfer

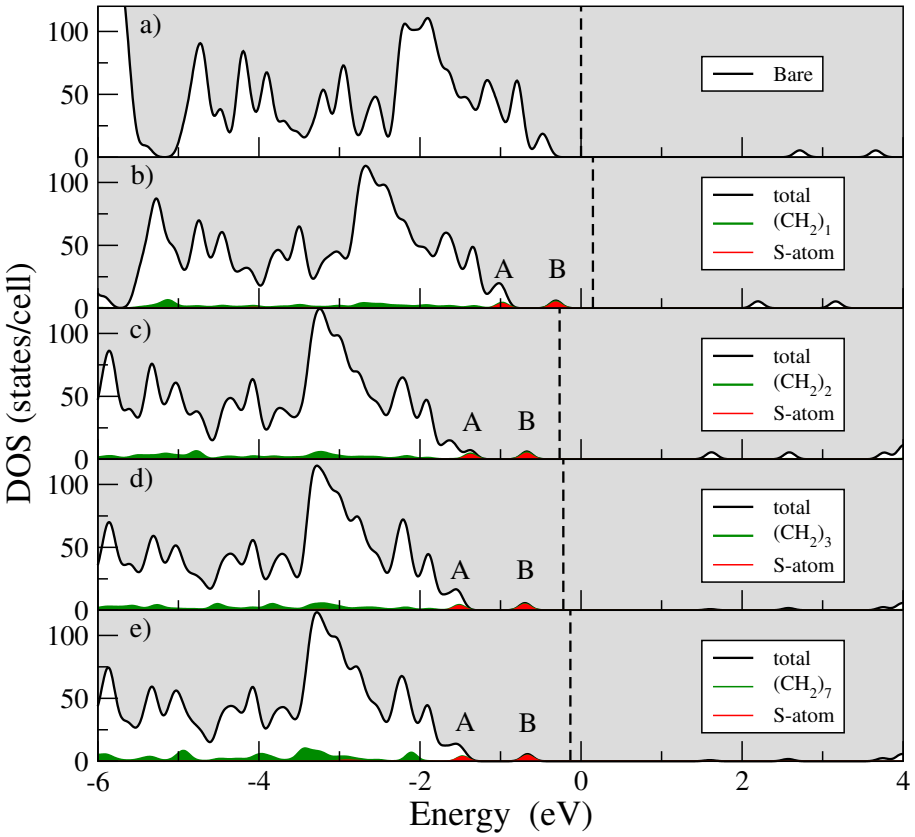

FIGURE 5.2: (a)-(e) Total and projected DOS for the bare and modified surfaces with MPA in a monodentate binding mode. The black and green lines represent the total DOS and its projection onto molecular states, respectively. The red lines represent the PDOS of the sulphur atom. Dashed lines denote the Fermi energy. A and B correspond to the highest-minus-one and the highest occupied state, respectively. Adapted with permission from [100]. Copyright 2018 American Chemical Society.

processes. Thus changes in the electronic structure of hybrid MPA/ZnO systems are dominated by the attached functional thiol group, not by the chosen carbon chain length for the MPA molecule.

Finally, the optical properties will be investigated. Intra-gap states can serve as a way to modify the optoelectronic properties of an atomic system. In order to investigate the possibility to use the aforementioned intra-gap states for this purpose, the dielectric function in the independent particle approximation (IPA) [109] has been calculated for the bare and the functionalized systems. The real part was calculated from ϵ_2 using the Kramers-Kronig relation according to

$$\epsilon_1(\omega) = 1 + \frac{2}{\pi} \int_0^\infty d\omega' \epsilon_2(\omega') \Big(\frac{\omega'}{\omega'^2 - \omega^2} \Big), \tag{5.1}$$

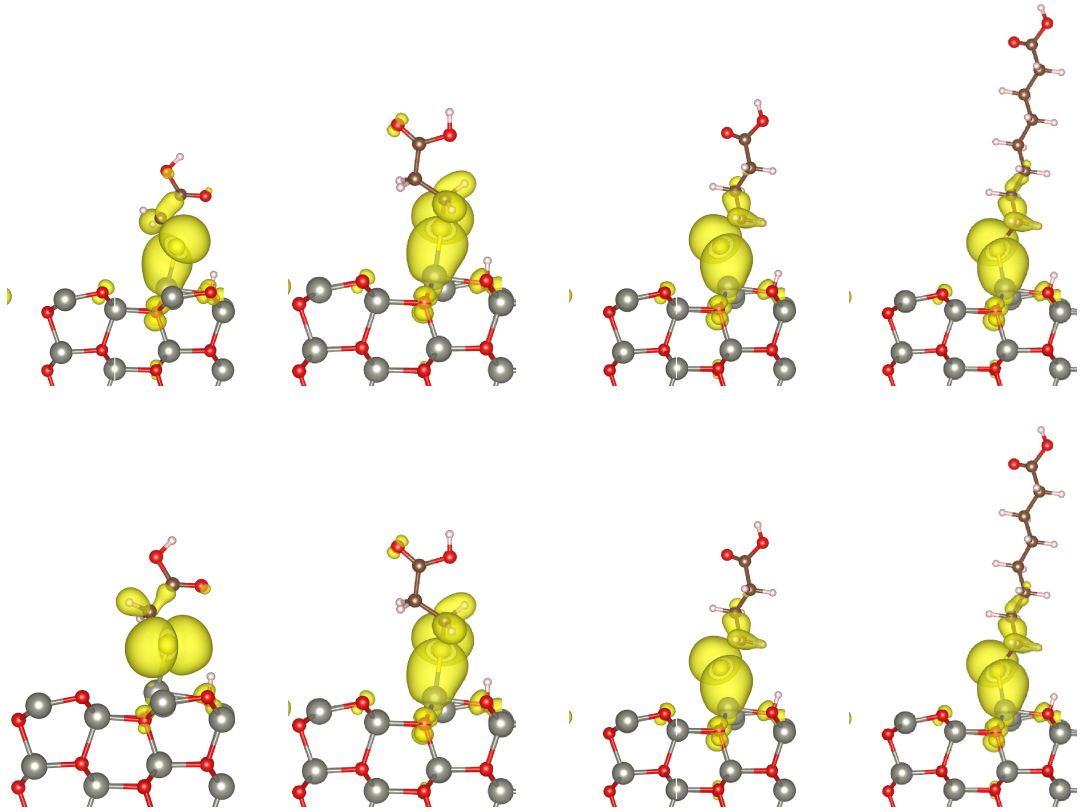

FIGURE 5.3: The band decomposed charge density at the Γ point. The figures at the top correspond to the HOMO-1 in SH-$(CH_2)_n$-COOH (n=1,2,3,7) on the $(10\bar{1}0)$ ZnO surface. The figures at the bottom correspond to the HOMO for the same systems. The A and B states are indicated in the Fig. 5.2(b)-(e). Adapted with permission from [100]. Copyright 2018 American Chemical Society.

On the other hand, for the imaginary part, the joint density of states and the momentum matrix elements between occupied and unoccupied states was used and calculated according to:

$$\begin{aligned} \epsilon_2^{ij}(\omega) &= \frac{4\pi^2 e^2}{\Omega m^2 \omega^2} \sum_{\mathbf{k}nn'} \langle \mathbf{k}n | p_i | \mathbf{k}n' \rangle \langle \mathbf{k}n' | p_j | \mathbf{k}n \rangle \times \\ &\quad \times f_{\mathbf{k}n} \left(1 - f_{\mathbf{k}n'}\right) \delta\left(E_{\mathbf{k}n'} - E_{\mathbf{k}n} - \hbar\omega\right), \end{aligned} \tag{5.2}$$

where e is the electron charge, m the electron mass, Ω is the volume of the crystal, $f_{\mathbf{kn}}$ the Fermi distribution function, and $|\mathbf{k}n\rangle$ the crystal wave function corresponding to the n^{th} eigenvalue $E_{\mathbf{k}n}$ with crystal wave vector $\mathbf{k}$.

In anisotropic materials like the investigated hybrid ZnO systems, dielectric properties are described by the so-called dielectric tensor. In this work it can be written

as follows

$$\underline{\underline{\varepsilon}} = \begin{pmatrix} \varepsilon_{\perp} & 0 & 0 \\ 0 & \varepsilon_{||} & 0 \\ 0 & 0 & \varepsilon_{||} \end{pmatrix} , \tag{5.3}$$

for a polarization perpendicular ($\varepsilon_{\perp}$) and parallel ($\varepsilon_{||}$) to the surface, respectively. Figure 5.4 displays the dielectric function for all chain lengths.

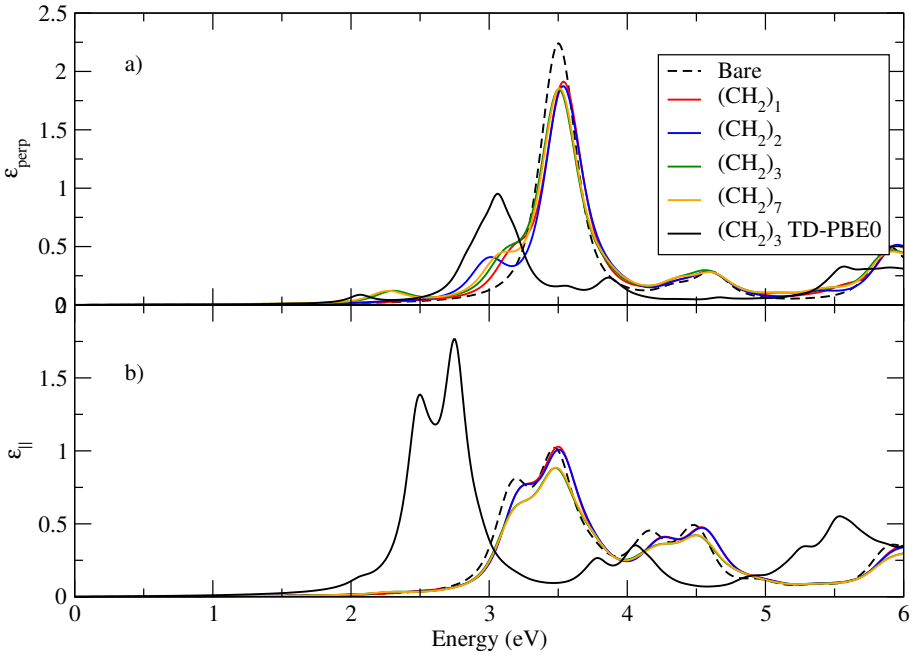

FIGURE 5.4: Dielectric function for the bare and modified surfaces with a monodentate binding mode, shown are $\varepsilon_{\perp}$ (a) and $\varepsilon_{||}$ (b). Reprinted with permission from [100]. Copyright 2018 American Chemical Society.

$\varepsilon_{\perp}$ in Fig. 5.4 (a) and $\varepsilon_{||}$ in Fig. 5.4 (b) correspond to the propagation of the electromagnetic field perpendicular and parallel to the surface, respectively. Optical activity of the intra-gap states is found for both cases. More precisely, $\varepsilon_{\perp}$ shows a peak around 2.3 eV for the SH-$(CH_2)_3$-COOH and SH-$(CH_2)_7$-COOH structures. They stem from band-to-band transitions between the conduction band of the surface and the molecular B state. In addition, transitions between the conduction band of the ZnO surface and the molecular A state correspond to a shoulder at low energies close to the main peak. This feature is found for all chain lengths, because the charge distribution extends across the MPA molecule to carboxyl group, resulting in a more delocalized charge distribution.

So far the IPA was employed which does not take excitonic effects into account.

However, the latter is needed in order to obtain a more accurate prediction of materials for optoelectronic devices. Electron-hole pairs can be included by employing different levels of approximative theoretical methods like TDDFT or GW+Bethe-Salpether equation (BSE). This allows the partial inclusion of excitonic effects. Excitation energies for catechol and dopamine interactions with TiO_2 surfaces have been obtained with TDDFT, as reported in [110]. Therefore, TDDFT calculations as introduced in Chapter 2 were performed to calculate the dielectric function. Occupied and empty states were calculated with the PBE0 functional. Compared to IPA-PBE0, this approach should lead to improved absorption spectra which are qualitatively equivalent to the solution of the BSE equation. Ultimately the dielectric function is then obtained by solving Casida's equation [111]. Figure 5.4 shows the results of this approach for the SH-$(CH_2)_3$-COOH structure for the $\varepsilon_\perp$ and $\varepsilon_\parallel$ components in (a) and (b), respectively.

Including many-body effects leads to a red shift of the spectrum. These results could stimulate further experiments on surface functionalization of ZnO with thiol groups. Additionally a GW+BSE spectrum would be helpful for comparison purposes, however, due to the high computational costs of such calculations, this is not possible at the moment. It is important to point out that a change of the physical picture is not expected when excitonic effects are included, since exciton binding energies between delocalized conduction band states and localized molecular states should be small, because of a small overlap in the corresponding Coulomb exchange matrix elements.

In conclusion, the absorption around 2.3 eV could be used to enhance the efficiency of functionalized semiconductor surfaces-based solar cells. Nanowires are typically grown along the [0001] direction with the non-polar surfaces being exposed. Since the additional absorption peak was found for the perpendicular component of the dielectric function, it would be most effective, if the field propagated along the nanowires surfaces.

5.2 GaN

GaN is a wide-bandgap semiconductor (3.4 eV), which is of high practical interest, because it is widely used in electrically pumped UV-blue LEDs, photodetectors, lasers, and high temperature devices [112–114]. This stability is one of the reasons, why GaN is often used for biomedical applications [115–118]. As described in the former Section for ZnO, functionalization with small molecules is a possible way to modify the physical properties of surface structures, since these molecules can bind covalently to a variety of biomolecules [119, 120]. These procedure can also be used to introduce optically active states into the band gap for applications in optoelectronic devices [121], as seen for large MPA molecules

on ZnO surfaces in the former Section. In the past organic groups like alkenes [122], silanes [123], and thiols [124] were attached to GaN surfaces in order to alter their electronic structure. Functionalization with thiol groups in particular indicates that the bonds remain stable, even upon annealing [124]. Additionally, the authors in [125] developed a technique to immobilize biomolecules by producing amine groups directly on the GaN surfaces. But despite these efforts over the years, GaN is still less explored than ZnO and several aspects like the adsorbant coverage or the strength of interaction between suitable molecules and the surface slabs and consequently their influence on the electronic structure of the hybrid systems are unclear. Thus this section will present a DFT study of electronic and optical properties of small ligands on GaN-$(10\bar{1}0)$ surfaces.

5.2.1 Computational details

For these calculations the same framework conditions as described in the Section about ZnO was employed. However, the smaller size of the attached molecules allowed the employment of a $(1 \times 10 \times 10)$ Monkhorst-Pack **k**-point sampling [21]. The most stable crystal phase of GaN is a wurtzite structure with 2 Ga and 2 N atoms per unit cell. In this work a surface slab with 8 GaN atomic layers and a vacuum region of 18 Å along the $(10\bar{1}0)$ direction modeled the bare surface. The same supercell dimensions were employed for the functionalized surfaces to ensure that the attached molecule will not interact with itself across the supercell boundaries. Furthermore, two molecules per supercell were considered, one on each side of the slab, leading to one ligand per surface unit cell.

5.2.2 Molecules on GaN (10-10) surfaces

Three different molecules were adsorbed, thiol groups ($CH_3 - SH$), carboxyl groups ($CH_3 - COOH$), and amine groups ($CH_3 - NH_2$). The optimized geometries are presented in Fig. 5.5. First, the structural and thermodynamic properties will be discussed. Thiol and carboxyl groups bind to the surface dissociatively, whereas the amine group does not dissociate. Similar to Section 5.1, the molecules bind with a monodentate binding mode to the surface. The Ga-N bond lengths in the center of all investigated systems vary between 1.95 and 2.00 Å, values similar to those found in bulk GaN. This means that the model is large enough to avoid interactions between both sides. However, a difference in bond lengths can be observed at the surface, where they are almost the same for the thiol and carboxyl systems compared to bulk, but shorter for the bare and amine system compared to bulk (1.84-1.90 Å). This is due to the presence of dangling bonds in the latter two cases. The dangling bonds at the nitrogen binding sites are passivated for the thiol and carboxyl cases due to the dissociation of the ligands.

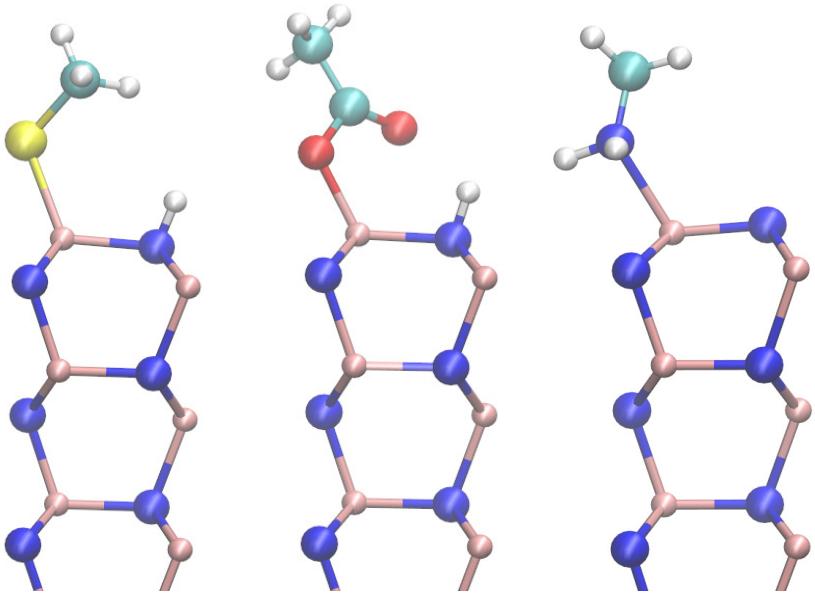

FIGURE 5.5: Optimized structures of the GaN surfaces functionalized with $CH_3 - SH$ (left), $CH_3 - COOH$ (middle) and $CH_3 - NH_2$ (right) molecules. The spheres represent gallium (bronze), nitrogen (blue), oxygen (red), carbon (turquoise), sulphur (yellow), and hydrogen (white) atoms.

In the case of modification with thiol groups (Fig. 5.5, left) the functional -SH groups adsorb on the surface via S-Ga bonds with a bond length of 2.26 Å and a S-Ga-N angle of 115°. The Ga-S-C angle is 111°. For the carboxyl system (Fig. 5.5, middle) the functional -COOH groups bind via two asymmetric bonds between the oxygen atoms of the functional group and the gallium atoms of the surface with a bond length of 1.90 Å and a O-Ga-N angle of 120°. The O-C-O angle is 122°. The amine groups (Fig. 5.5, right) bind via N-Ga bonds with a bond length of 2.15 Å and a N-Ga-N angle of 117°. The Ga-N-C angle is 132°.

Adsorption energies were calculated to evaluate the stability of the investigated molecules on GaN surfaces. Analogously to Section 5.1, they were calculated according to $E_{ads} = E_{tot}^{GaN/mol} - E_{tot}^{bare} - E_{tot}^{mol}$, with $E_{tot}^{GaN/mol}$, E_{tot}^{bare} and E_{tot}^{mol} as the total energies for the functionalized GaN model, for the bare surface, and for the isolated molecule, respectively. The resulting values are -3.22 eV (thiol), -4.01 eV (carboxyl), and -0.54 eV (amine). This indicates that all attached groups bind strongly to the surface, which corroborates with experimental works [124, 125].

Secondly, the electronic properties are to be discussed. The total and projected DOS for the bare and functionalized surfaces are presented in 5.6. The band alignment was done with respect to the vacuum level as described in [107, 108] and performed in Section 5.1. As mentioned before, the vacuum region in which the structures are embedded, is large enough to ensure that the electrostatic potential

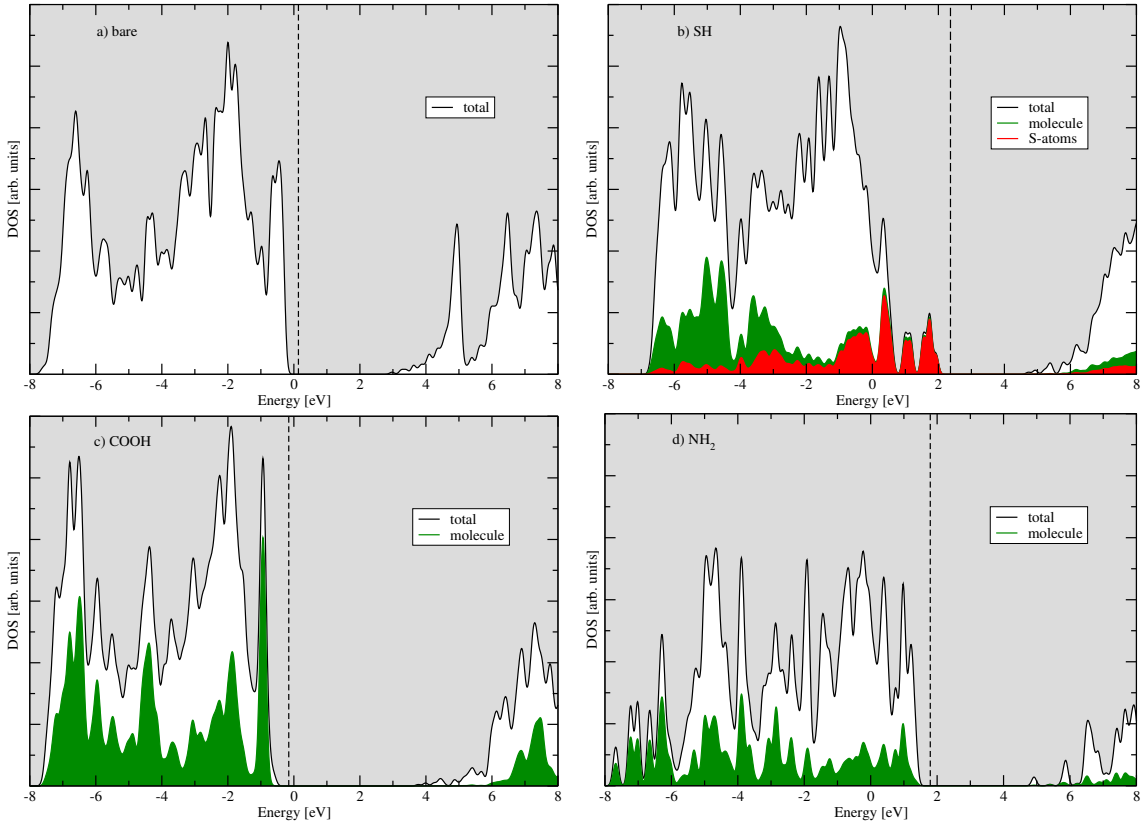

FIGURE 5.6: Projected density of states for the a) bare and functionalized surfaces with b) thiol, c) carboxyl, and d) amine groups. The black, green, and red lines represent the total DOS, the projection onto the ligand states, and the contribution from the sulphur atoms, respectively. The dashed line denotes the Fermi energy.

reaches its vacuum value and flattens out. Furthermore, the DOS are aligned relatively to the VBM of the bare surface, whose energy was set to 0 eV.

Using the PBE0 functional yields a band gap of 3.6 eV for bulk GaN which is much more in line with the experimental value [106] and in agreement with other works [126]. However, a slightly reduced band gap was found for the bare surface. This is due to additional surface states close to the valence and conduction bands.

In the case of modification with thiol groups two intra-gap states are introduced into the band gap. They are located energetically at 0.3 eV and VBM + 1 eV, as displayed in Fig. 5.6 (b). These states stem mainly from S-*p* states of the thiol groups. In addition, changes around the VBM are visible. This is also due to the S-*p* states, which hybridize with the N-*p* states of the surface. The band decomposed partial charge density was calculated in this case for a more complete picture of these intra-gap states, and is shown in Fig. 5.7. This confirms the aforementioned findings as the intra-gap states are strongly localized on the sulphur atoms, as shown

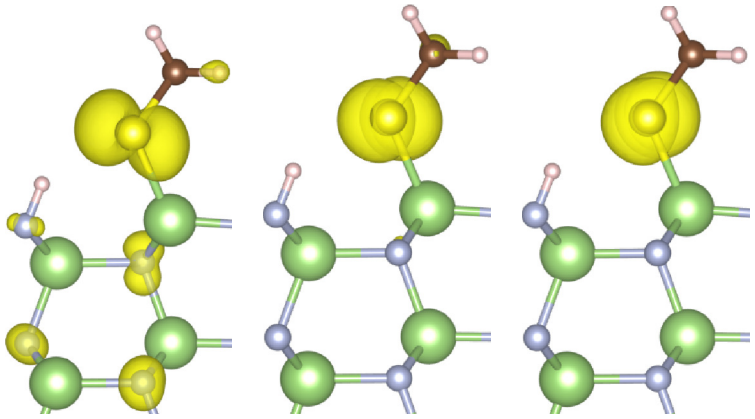

FIGURE 5.7: Band projected charge density for thiol group adsorbed on the GaN-(10$\bar{1}$0) surface. From left to right, the HOMO-2, HOMO-1, and HOMO is shown.

in Fig. 5.7 for the HOMO-1 (middle) and the HOMO (right). On the other hand, the HOMO-2 (left) hybridizes with the surface. Fig. 5.6 (b) confirms this, consequently leading to a delocalized charge.

The functionalization with carboxyl groups leads to different results. In contrast to thiol, the electronic structure shows no intra-gap states as displayed in Fig. 5.6 (c). Instead, strong changes around the VBM are found, the surface N-*p* states hybridize with the O-*p* states of the carboxyl group, which results in localized states at the VBM. C-*p* states are located deep in the valence band and overlap with Ga-*d* states. The molecular states at VBM + 7.7 eV in the conduction band stem mainly from C-*p* and O-*p* states.

The DOS for the amine system (Fig. 5.6 (d)) shows a weak hybridization between N-*p* states of the amine group and N-*p* surface states directly at the VBM. The most striking feature is an overall shift to higher energies compared to the other structures. A possible explanation is the non-dissociative binding behaviour of the molecule. The surface N atoms possess dangling bonds, which results in a strongly reduced work function. The required energy to remove an electron is therefore decreased. These results agree with experimental works, suggesting that functionalization with amine groups does not influence the conductivity of GaN systems [125].

Finally, the optical properties will be discussed. Figure 5.8 shows the dielectric function for all systems. The functionalization of ZnO surfaces in Section 5.1 lead to the presence of optically active intra-gap states with an additional absorption peak. This feature is not found for the intra-gap states introduced by thiol groups on GaN surfaces. Thus functionalizing the surface with thiol groups would trap non-recombining holes in the band structure. For carboxyl on GaN a similar behaviour is found. The presence of molecular states at the VBM suppresses optical

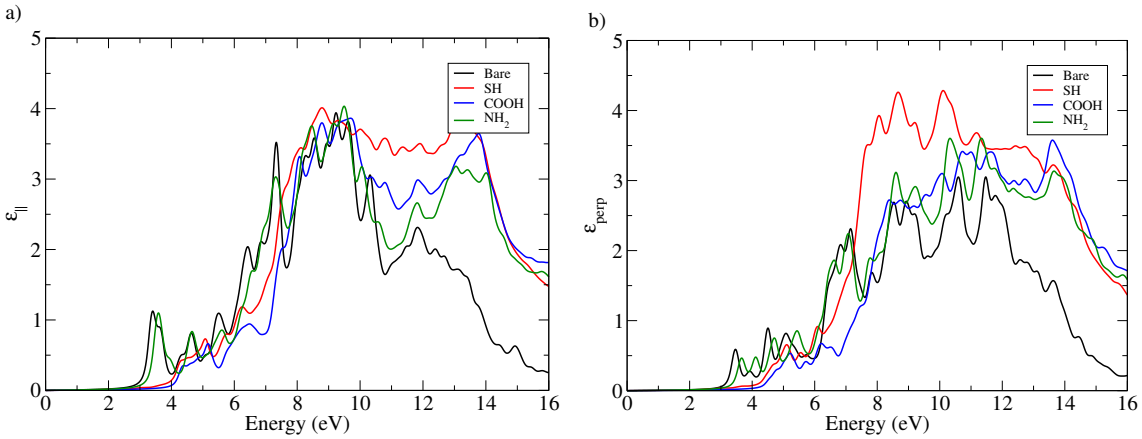

FIGURE 5.8: Dielectric function for the bare and modified surfaces, shown are (a) $\varepsilon_{||}$ and (b) $\varepsilon_{\perp}$.

absorption. In contrast to these observations, for bare surfaces and surfaces functionalized with amine groups, a distinct peak is visible around the absorption onset. This reflects the presence of dangling bonds.

Chapter 6

Doping of zinc oxide with cobalt

This chapter reports on GW calculations of cobalt implanted ZnO nanostructures. Structural as well as thermodynamic and electronic properties will be discussed for a variety of intrinsic defects and defect complexes in order to investigate which defect complex is responsible for the experimentally observed 3*d*-intrashell emission [127–129].

6.1 Cobalt in zinc oxide

Cobalt doped zinc oxide nanoparticles have been investigated experimentally and theoretically to some extent over the course of the last fifty years [127, 130–132]. However, in more recent years, such systems gained considerable interest due to the possibility for the use as diluted magnetic semiconductors (DMS). DMS are of interest, because they possess unique spintronics properties and provide a way to possibly use the spin of electrons in addition to their charge. Ultimately this could be used to record information and consequently such spin-polarized devices could be smaller and more efficient than today's systems which are based on the charge exclusively [133, 134]. However, these devices usually only work at low temperatures due to their low Curie temperature T_C, but Co-doped ZnO nanostructures are ferromagnetic at room temperature. Zinc interstitials and oxygen vacancies were found to be the reasons for this [135].

Furthermore, doping with transition metals can extend the emission range from the intrinsic band gap to the infrared spectrum. Consequently, Co atoms can be incorporated as optical centers into the ZnO matrix, allowing to tune its electronic and optical properties, making it interesting for optoelectronic devices, for example as single-photon emitters [136, 137]. It was shown that it is an efficient luminescent center when incorporated at substitutional sites [129, 138].

Several experiments indicate that transitional-metal elements like cobalt typically occupy cation sites in zinc oxide replacing a zinc atom [139, 140]. In the case of cobalt, this leads to a formal charge of 2+ and a $3d^7$-configuration for the Co ion, with a ^{4}F ground state, followed by the ^{4}P and ^{2}G excited states.

It was observed that the ground term splits into the $^4T_1(F)$ term at 0.78 - 1.13 eV and the $^4T_2(F)$ term at 0.45 - 0.55 eV above the $^4A_2$ ground term [128, 141]. After implantation, several experiments assign a luminescence signature at 1.88 eV to the $^2E(G) \rightarrow^4 A_2(F)$ transition and an additional one at 2.02 eV to the $^1T(P) \rightarrow^4 A_2(F)$ transition [142, 143]. However, it is still not entirely clear, what kind of intrinsic defect or defect complex is responsible for this phenomenon. This study will offer an explanation for this from a computational perspective.

6.2 Computational details

A combination of DFT [17, 18] and many-body GW methods [47] as implemented in the Vienna ab initio simulation package (VASP) [101–104] and introduced in Chapter 2 has been employed in order to investigate the formation energies and electronic structure of Co-doped ZnO and its complexes. The supercell consisted of 72 atoms with a concentration of 2.8 %. The projected augmented wave method has been used [19] to relax the structures with the PBE exchange-correlation functional [33]. A plane wave basis set with an energy cutoff of $E_{\text{cut}} = 400\,\text{eV}$ and a $(3 \times 2 \times 2)$ Monkhorst-Pack **k**-point sampling was employed for the GW calculations of the defect complexes [21]. They have been performed with 1000 bands after convergence tests. For ZnO, a $(6 \times 6 \times 6)$ **k**-point sampling with a cutoff of 400 eV has been applied to a wurtzite bulk model, consisting of 4 atoms. For zinc bulk, $(10 \times 10 \times 10)$ **k**-points were used.

6.3 Results

6.3.1 Thermodynamic properties

Formation energies provide a way to assess the thermodynamic stability of defect complexes. Following the approach described in [144], the formation energy E_f of a neutral defect in ZnO is defined as

$$E_\text{f} = E^\text{tot}_\text{defect} - E^\text{tot}_\text{bulk} - \sum_i n_i \mu_i, \tag{6.1}$$

where $E^\text{tot}_\text{defect}$ is the total energy of the respective defect complex and E^tot_bulk is the total energy of a bulk ZnO supercell. n_i describes the number of atoms of type i that have been added or removed from the complex with μ_i as the corresponding chemical potential. Since the conditions can be anything in between Zn-rich or O-rich conditions in a growth process, limits should be introduced to the chemical potential μ. In the lower limit, the material is free of defects, whereas the upper limit corresponds to the formation of elemental bulk phases. This can be avoided

by employing the following condition for Co metal

$$\mu_{\mathrm{Co}} \leq \mu_{\text{Co-bulk}}. \tag{6.2}$$

A similar condition can be imposed for cobalt oxide in order to avoid the formation of such crystal phases

$$\mu_{\mathrm{Co}} \leq \mu_{\mathrm{CoO}}, \tag{6.3}$$

where CoO was chosen as the upper limit, since it is a very stable phase of cobalt. With μ_{Zn} and μ_{O} as the chemical potentials of zinc and oxygen, respectively, the ZnO chemical potential reads

$$\mu_{\mathrm{ZnO}} = \mu_{\mathrm{Zn}} + \mu_{\mathrm{O}}. \tag{6.4}$$

Using the formation enthalpy of ZnO ΔH^{ZnO}

$$\Delta H^{\mathrm{ZnO}} = E^{\mathrm{tot}}_{\mathrm{ZnO}} - \mu_{\mathrm{Zn}} - \mu_{\mathrm{O}}, \tag{6.5}$$

the potential energy of oxygen can be expressed as

$$\mu_{\mathrm{O}} = \mu_{\mathrm{O_2}} + \lambda \Delta H^{\mathrm{ZnO}}, \tag{6.6}$$

where $\mu_{\mathrm{O_2}}$ is the oxygen molecule chemical potential and λ is either 0 or 1 for oxygen rich or oxygen poor conditions, respectively.

In order to obtain an expression for μ_{Co}, the chemical potential of cobalt oxide is needed

$$\mu_{\mathrm{CoO}} = \Delta H^{\mathrm{CoO}} + \mu_{\text{Co-bulk}} + \mu_{\mathrm{O_2}}, \tag{6.7}$$

where ΔH^{CoO} is the formation enthalpy of cobalt oxide bulk. Finally, the chemical potential for cobalt can be written as

$$\mu_{\mathrm{Co}} \leq \Delta H_{\mathrm{CoO}} + \mu_{\text{Co-Bulk}} - \lambda \Delta H^{\mathrm{ZnO}}. \tag{6.8}$$

The total energy for the respective zinc and cobalt bulk systems were calculated on hcp crystal phases.

A value of $\Delta H^{\mathrm{ZnO}} = 2.88\,\mathrm{eV}$ was calculated for the formation of enthalpy for bulk ZnO, which is in good agreement with other GGA calculations [145, 146]. Furthermore, cohesive energies of $E^{\mathrm{ZnO}}_{\mathrm{c,PBE}} = -7.37\,\mathrm{eV}$ and $E^{\mathrm{Zn}}_{\mathrm{c,PBE}} = -1.11\,\mathrm{eV}$ have been calculated, which agree very well with experimental values of $E^{\mathrm{ZnO}}_{\mathrm{c,exp}} = -7.52\,\mathrm{eV}$ [106] and $E^{\mathrm{Zn}}_{\mathrm{c,exp}} = -1.35\,\mathrm{eV}$ [147], respectively.

Table 6.1 displays the calculated formation energies for the investigated defects under O-rich and O-poor conditions.

	E_f [eV]	
defect	O-rich	O-poor
Co_{Zn}	-0.91	0.94
V_{Zn}	1.63	4.51
V_O	3.74	0.85
Zn_i	5.44	2.56
O_i	4.01	6.89
$Co_{Zn} + V_{Zn}$	0.25	4.99
$Co_{Zn} + V_O$	3.41	2.37
$Co_{Zn} + Zn_{int}$	14.79	13.76
$Co_{Zn} + O_{int}$	1.83	6.57

TABLE 6.1: Formation energies E_f for the intrinsic defects and defect complexes in ZnO calculated with the PBE functional.

As expected, incorporating cobalt into the ZnO matrix does not disturb the lattice in a significant manner, which is reflected in the low formation energies of -0.91 eV and 0.94 eV for oxygen rich and oxygen poor conditions in the absence of intrinsic defects, respectively. Oxygen vacancies also have a very low formation energy (0.85 eV) under O-poor conditions, whereas zinc vacancies have a similarly low formation energy (1.63 eV) under O-rich conditions, which is plausible. The formation energies further confirm that in the limit of O-rich conditions, oxygen interstitials are also more likely to form compared to the O-poor case, as expected. The opposite is true for zinc interstitials. These values agree with other works [148]. On the other hand, incorporating cobalt at an interstitial site is unfavourable due to the stress and will therefore not be discussed here [149].

The most stable defect complexes under O-rich (Zn-poor) conditions are the $Co_{Zn} + V_{Zn}$ (0.25 eV) and the $Co_{Zn} + O_{int}$ (1.83 eV) defect complexes. So it is energetically more favourable to create a zinc vacancy than to create an oxygen interstitial. This might be due to the fact that because of their size, incorporating an O atom at an interstitial site causes more stress to the ZnO matrix. This is corroborated by the observation, that $Co_{Zn} + Zn_{int}$ complexes have very high formation energies under both conditions and are therefore very unlikely to form. This will be of interest when discussing the electronic structure later. However, a possible explanation for the stability of the $Co_{Zn} + O_{int}$ complex could be the low diffusion barrier for oxygen interstitials [148]. Furthermore, under O-poor (Zn-rich) conditions, only the $Co_{Zn} + V_O$ complex has a fairly low formation energy (2.37 eV). Interestingly, the isolated oxygen interstitial has a fairly high formation energy. This means that once it is formed during an experiment, it can quickly form complexes in the material.

6.3.2 Electronic properties

Different functionals have been applied to the calculation of bulk ZnO. Since every approach yields a different band gap, the results have been under debate. Parameters like the choice of the exchange-correlation potential for the underlying DFT calculation [150, 151] or the number of total bands influence the outcome [152]. Table 6.2 gives an overview of the calculated band gaps in this work for several different functionals in comparison to values from the literature

	E_g [eV]	
Functional	This work	Literature
PBE	0.78	0.74 [153]
PBE0	3.16	3.18 [145]
HSE06	2.46	2.49 [145]
PBE+G_0W_0	2.57	2.12-3.01 [53, 131, 154, 155]
PBE+GW_0	3.30	2.54-3.55 [131, 154–156]

TABLE 6.2: Calculated band gaps E_g for bulk ZnO calculated with a variety of functionals.

Describing the band gap correctly is important for investigations of impurities in semiconductors [157, 158]. Therefore, the PBE+GW_0 approach was chosen in this work, since it yields a band gap close to the experimental value. It was shown that a large number of bands needs to be considered to obtain properly converged results in G_0W_0 calculations [150, 159]. However, Sarsari et al. have shown, that the position of the defect states is not significantly affected by the number of empty bands and the cutoff of the response function [131]. For the GW_0 calculations in this work, 1000 bands were used. This results in a quasi-particle band gap of 3.30 eV in reasonable agreement with the experimental value of 3.44 eV [160] and with other GW_0 calculations [151]. Furthermore, it has been shown that the GW method provides an accurate description for itinerant and localized states of many open *d*-shell materials [161]. Consequently, from here on only results obtained from GW_0 calculations will be presented.

First, the structural and electronic properties of cobalt at a zinc lattice position will be discussed. The corresponding geometry can be seen in Fig. 6.1. The cobalt distances to nearest neighbour oxygen atoms are 1.97 Å and 1.98 Å for in-plane and c-direction, respectively. The Co-Zn distances are 3.29 Å for in-plane and 3.23 Å for c-direction. These values agree very well with the corresponding distances in pure ZnO, which are 1.98 Å for Zn-O and 3.24 Å for Zn-Zn. Therefore an incorporation of Co at a Zn position does not disturb the lattice significantly. Fig. 6.2 displays the density of states for the Co_{Zn} defect. The Co-*d* states lie inside the band gap, around 2 eV above the VBM. In this configuration, Co has a formal charge of 2+. The *d* spin-up orbitals are fully occupied, whereas the *d* spin-down

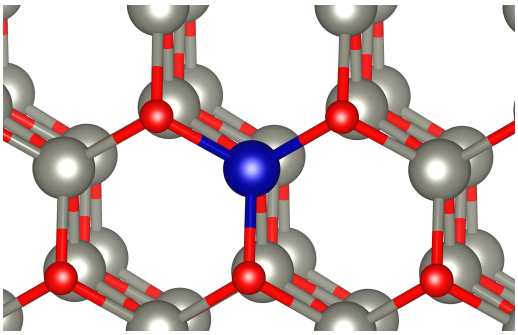

FIGURE 6.1: Atomic structure around the Co_{Zn} defect calculated with the PBE functional. Grey, red and blue spheres represent Zn, O, and Co atoms, respectively.

orbitals are only partially occupied, resulting in a total magnetic moment of 3 μ_B. However, there are no unoccupied states inside the band gap or close to the CBM, which does not fit with the experimentally observed luminescence.

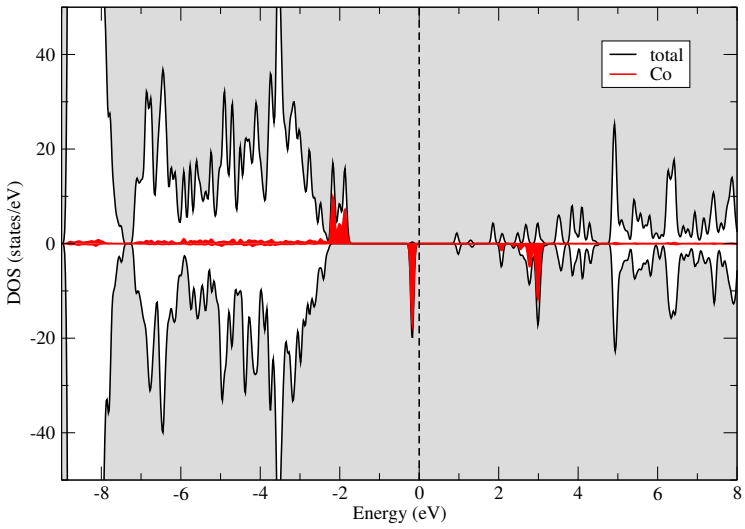

FIGURE 6.2: Density of states for the Co_{Zn} defect calculated within the PBE+GW_0 approximation. The vertical line denotes the highest occupied state. Positive (negative) values of the DOS denote spin up (down).

Introducing intrinsic defects is a possible way to modify the oxidation state of Cobalt in zinc oxide. Intrinsic defects disturb the lattice and lead to a change of the environment. It was shown that during ion implantation intrinsic defects are likely to form [136, 162]. Therefore, cobalt doped zinc oxide has been investigated in the presence of intrinsic defects, namely zinc vacancies, oxygen vacancies, zinc interstitials, and oxygen interstitials.

The optimized geometry of the $Co_{Zn} + V_{Zn}$ complex is shown in Fig. 6.3. In this case, the Co atom slightly shifts towards the vacancy, resulting in two different

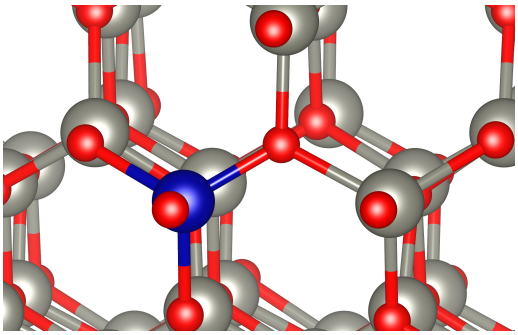

FIGURE 6.3: Atomic structure around the $Co_{Zn} + V_{Zn}$ complex calculated with the PBE functional. Grey, red and blue spheres represent Zn, O, and Co atoms, respectively.

Co-Zn distances for the c-direction with 3.21 Å and 3.29 Å as well as in two different Co-Zn distances for the in-plane direction with 3.27 Å and 3.30 Å. Consequently, the Co-O bond lengths change accordingly. The in-plane distances decrease to 1.79 Å and 1.90 Å, whereas they change along the c-direction to 1.94 Å. Fig. 6.4 shows the corresponding density of states.

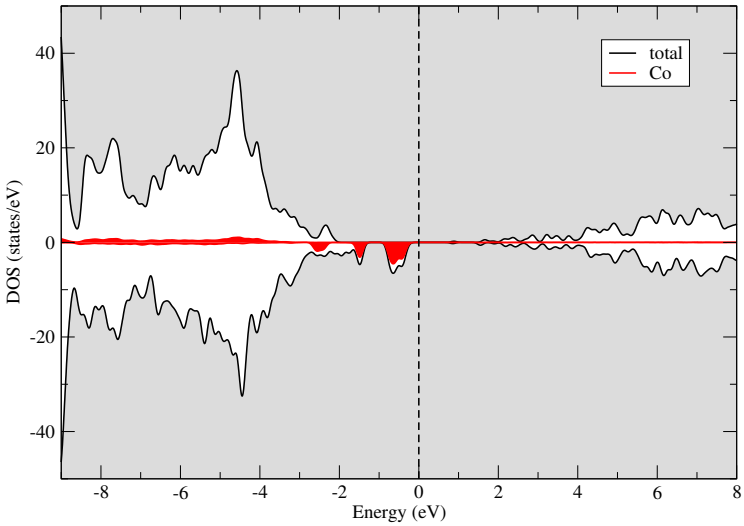

FIGURE 6.4: Density of states for the $Co_{Zn} + V_{Zn}$ complex calculated within the PBE+GW_0 approximation. The vertical line denotes the highest occupied state. Positive (negative) values of the DOS denote spin up (down).

There are no unoccupied Co-*d* states inside the band gap and the formal charge of the Co atom is closer to 3+. Occupied states are located at the VBM and around 1 eV above it. Considering both observations, this defect complex cannot be responsible for the experimentally observed 2+-emission.

Next, cobalt at a Zn site in the presence of an a oxygen vacancy was investigated. The presence of the vacancy does not disturb the lattice strongly, compared to the

case without it, the Co-O distances remain almost unchanged with 1.96 Å. The geometry can be seen in Fig. 6.5.

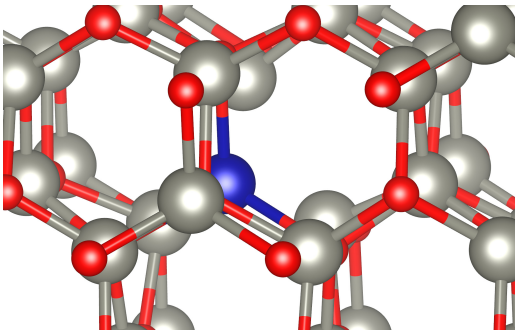

FIGURE 6.5: Atomic structure around the $Co_{Zn} + V_O$ complex calculated with the PBE functional. Grey, red and blue spheres represent Zn, O, and Co atoms, respectively.

Co-Zn distances are also almost the same with 3.27 Å for in-plane and 3.29 Å for c-direction. The electronic structure for this system is displayed in Fig 6.6.

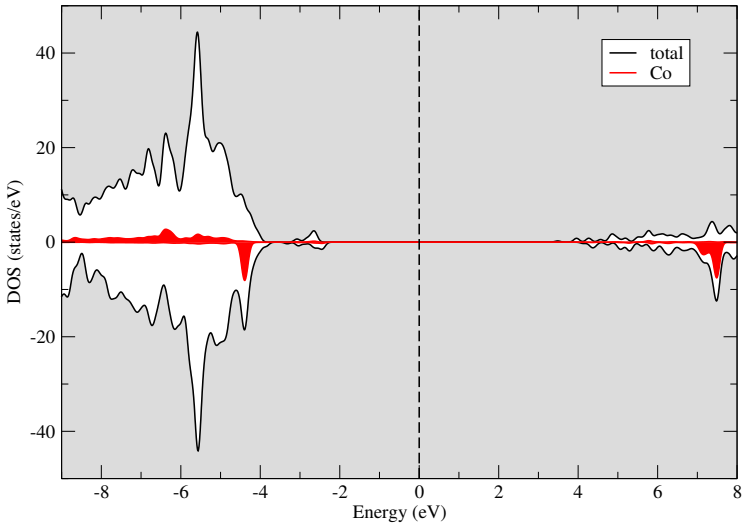

FIGURE 6.6: Density of states for the $Co_{Zn} + V_O$ complex calculated within the PBE+GW_0 approximation. The vertical line denotes the highest occupied state. Positive (negative) values of the DOS denote spin up (down).

There are no intra-gap states stemming from the Co atom inside the band gap. The energy difference between the occupied and unoccupied Co 3*d*-states is around 11 eV and therefore this defect complex cannot be responsible for the photoluminescence.

Besides these vacancies, interstitals were also investigated. The optimized geometry of the zinc interstitial defect complex is presented in Fig. 6.7. The zinc interstitial disturbs the lattice and consequently the cobalt atom relaxes away from

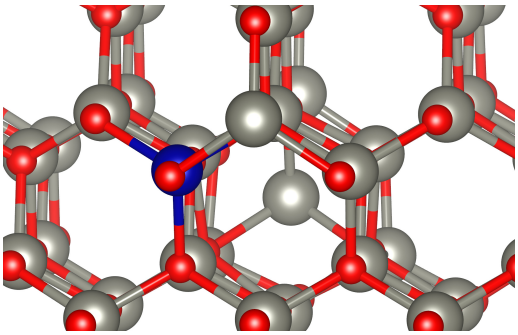

FIGURE 6.7: Atomic structure around the $Co_{Zn} + Zn_{int}$ complex calculated with the PBE functional. Grey, red and blue spheres represent Zn, O, and Co atoms, respectively.

it. This is corroborated by the fact that the distances between the interstitial and its nearest oxygen neighbours vary from 1.69 Å to 2.20 Å. Thus it is incorporated asymmetrically. Furthermore, this results in Co-O distances of 2.00 Å for the in-plane and 2.06 Å in c-direction. The Co-Zn distances are 2.21 Å to the Zn_i and 3.25 Å to the second nearest neighbours in the lattice. The density of states for this system is shown in Fig. 6.8.

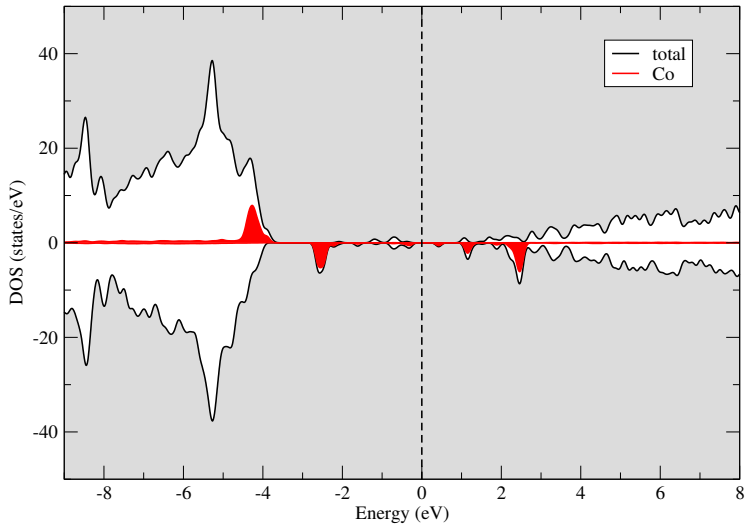

FIGURE 6.8: Density of states for the $Co_{Zn} + Zn_{int}$ complex calculated within the PBE+GW_0 approximation. The vertical line denotes the highest occupied state. Positive (negative) values of the DOS denote spin up (down).

For this system, intra-gap states appear. Unoccupied states are located at -2.5 and -0.3 eV, while occupied states are located at 0.4 and 1.2 eV. The formal charge of the Co atom remains close to 2+, which fits with the ^{4}F ground state. However, the very high formation energy of this complex makes it very unlikely that it is responsible for the 3*d*-emission.

The final investigated defect complex consists of an oxygen atom at a octahedral interstitial site next to a cobalt atom at a zinc position. The corresponding atomic structure is presented in Fig. 6.9.

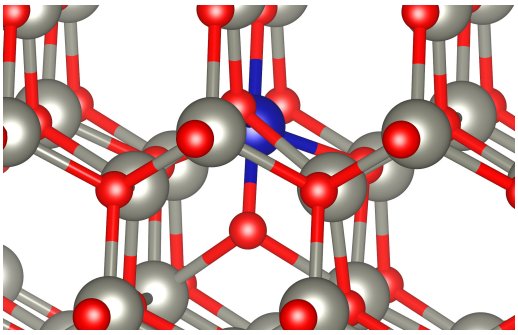

FIGURE 6.9: Atomic structure around the $Co_{Zn} + O_{int}$ complex calculated with the PBE functional. Grey, red and blue spheres represent Zn, O, and Co atoms, respectively.

The Co-O distances to nearest neighbour oxygen atoms in the ZnO lattice are 1.92 Å along the c and 1.94 Å for the in-plane direction. The distance to the oxygen interstitial is 1.73 Å. The corresponding electronic structure is shown in Fig. 6.10.

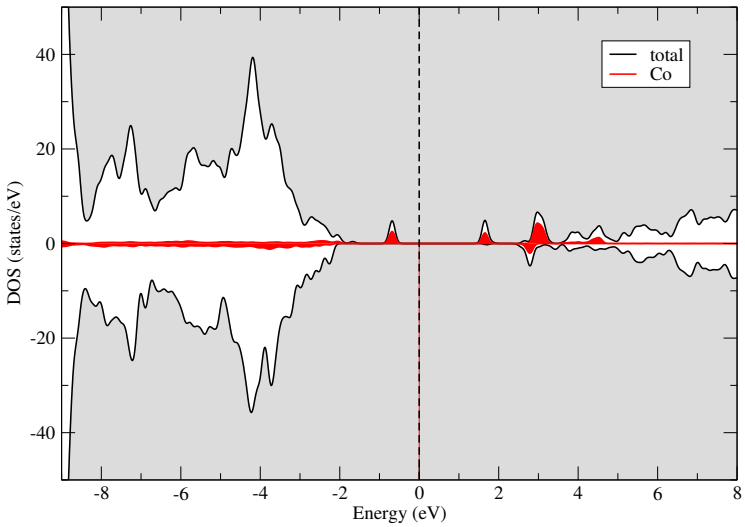

FIGURE 6.10: Density of states for the $Co_{Zn} + O_{int}$ complex calculated within the PBE+GW_0 approximation. The vertical line denotes the highest occupied state. Positive (negative) values of the DOS denote spin up (down).

The occupied Co 3*d*-states are located inside the band gap, with the Co-3*d* orbitals being occupied with six electrons. The occupied and unoccupied states are located at -0.6 eV and 1.6 eV, respectively. This fits well with the experimentally observed luminescence signature at 1.88 eV and 2.02 eV. The total magnetic moment of the complex is 2.8 μ_B, determined by a magnetic moment of 1.92 μ_B on the

cobalt, 0.2 μ_B on the oxygen interstitial atom, and contributions from the oxygen atoms surrounding the defect complex. Therefore, also taking into consideration, that this is a thermodynamically stable defect complex, the intra-3*d* luminescence of the cobalt-doped zinc oxide is most likely due to $Co_{Zn} + O_{int}$ complexes.

Chapter 7

Density functional based tight binding parametrization and applications

7.1 HfO

Hafnium oxide (HfO_2) is one of the most promising candidates to replace silicon dioxide (SiO_2) as the main gate oxide material in electronic components [163, 164]. Nowadays, electronic devices are steadily being decreased in size. Consequently, the SiO_2 gate oxide needs to be manufactured with a very small thickness as well, which leads to high tunneling leakage current [7, 8]. To deal with this problem, metal oxides with higher dielectric constants κ like Al_2O_3 and HfO_2 came into focus [163]. Scientific interest in HfO_2 has grown over the past years, because it provides advantages like high thermal stability in contact with silicon besides the dielectric constant [165]. Those high-κ metal oxides are preferred in their amorphous form for applications due to several reasons. The isotropic physical properties of amorphous structures matter especially, since they result in less defects at the interface with the Si substrate and very low leakage currents, therefore avoiding the major problem of SiO_2. Furthermore, amorphous metal oxides are easier to handle during the CMOS fabrication process [166]. Additionally, Hf-based alloy materials are also being studied and used as gate oxides in the semiconductor industry [167, 168].

Another important application area of amorphous HfO_2 is optical coating, since most of the presently used optical components feature a thin-film coating. Hence, modern coating techniques serve as important tools to produce thin films with advanced optical properties [169]. Especially ion coating methods such as ion beam sputtering (IBS) or ion assisted deposition tend to produce amorphous thin films with enhanced properties like surface smoothness and high optical homogeneity.

a-HfO_2 has been widely investigated using ab initio molecular dynamics to determine its structural, electronic and dielectric properties [170–174]. But the disordered nature of amorphous structures yields some computational problems. Exploring large systems over long periods using conventional ab initio methods is very time consuming. Chapter 3 introduced the DFTB method, which is one possible way to overcome these difficulties. This section will present the DFTB parametrization procedure for hafnium oxide. The parametrization is then validated against both, ab initio data on hafnium and hafnium oxide crystalline structures as well as amorphous systems using classical potentials and DFT. Major parts of this Section are based on previously published results [175]. Parts of it were obtained during the author's Master's project.

7.1.1 Creating the reference data

At ambient pressure, HfO_2 crystallizes in three polymorphs, dependent on the temperature. The most stable one is the monoclinic phase ($P2_1/c$). The phase transition to the less stable tetragonal phase ($P4_2/nmc$) takes place at 1720 °C and the phase transition to the high temperature cubic (fcc) phase ($Fm\bar{3}m$) occurs at 2600 °C [176]. Hafnium on the other hand has two different crystalline phases, a hexagonal close-packed phase ($P6_3/mmc$) and the less stable cubic (bcc) phase ($Im3m$) with a phase transition at 1750 °C [177].

Ab initio reference data are needed for the parametrization procedure. For this, the PBE functional within VASP [101–104] was employed in order to optimize the different crystal structures of hafnium and hafnia. The projector augmented waves (PAW) were applied to model the electrons in the core. In general, a DFTB parametrization requires band structures, formation energies and structural data of all considered crystal phases. More details about the geometric input for those phases of hafnium and hafnia can be seen in table 7.1 [178, 179]. $12 \times 12 \times 12$ and $4 \times 4 \times 4$ Monkhorst-pack k-point meshes have been employed for DFT calculations of hafnium and hafnia, respectively [21]. In addition, a plane wave basis and an energy cutoff of $E_c = 400\,\text{eV}$ was used [19, 20]. The atomic structures were optimized using the PBE functional [33].

7.1.2 The parametrization procedure

The parametrization procedure consists of two major parts. First, the electronic part of the interatomic interaction between two elements has to be created. This is done by choosing a basis and confinement radii for the orbitals and density (see Chapter 3) to calculate a DFTB band structure. Then, different confinement radii are chosen until the DFTB band structure matches the reference DFT counterpart satisfyingly. For the O-O interaction, the respective sk file was taken from the

model	phase	parameter	value
Hf	bcc	a	3.50 Å
Hf	hcp	a	3.197 Å
Hf	hcp	c	5.068 Å
Hf	hcp	γ	120.0 °
HfO_2	fcc	a	5.08 Å
HfO_2	tetra	a	5.15 Å
HfO_2	tetra	c	5.29 Å
HfO_2	tetra	d	0.302 Å
HfO_2	mono	a	5.127 Å
HfO_2	mono	b	5.175 Å
HfO_2	mono	c	5.291 Å
HfO_2	mono	γ	99.22 °
HfO_2	mono	r_{Hf}	(0.276, 0.040, 0.208)
HfO_2	mono	r_{O_1}	(0.074, 0.332, 0.347)
HfO_2	mono	r_{O_2}	(0.449, 0.758, 0.480)

TABLE 7.1: Geometric parameters for the crystal phases of Hf and HfO_2. The lattice constants a, b and c are given in Å, the angle γ in °. d describes the deviation of the O atom relatively to its ideal position in the cubic phase. Atomic coordinates r_{Hf}, r_{O_2} and r_{O_1} are given as internal coordinates. Reprinted with permission from [175]. Copyright 2018 by the American Physical Society.

well-established mio set for organic molecules [180]. This saves time and effort to create a new SK-file for O-O and opens up the possibility to add hafnium to the whole set of organics within the mio set, if needed. Secondly, the repulsive part has to be created. For this purpose, several reference DFT calculations are needed as target systems.

Electronic part

The electronic part contains Hamilton and overlap matrix integrals, which were calculated according to Chapter 3. This requires choosing the confinement radii for the orbitals and the density for the explicitly treated atomic orbitals in such a way that the reference ab initio band structure is matched. For pure hafnium occupied 6-*s*, occupied 5-*d*, and unoccupied 6-*p* orbitals were considered. The other orbitals were modeled as a frozen core. The optimal values for the confinement radii in this case are 4.42 a_0 for the density, 10.52 a_0 for the 6-*s* and 5-*d* orbitals, and 5.00 a_0 for the 6-*p* orbitals.

Repulsive part

For the Hf-O interatomic interaction, the repulsive part was obtained by fitting the difference between the DFT total energy curve and DFTB electronic energy curves against varying values of the lattice constant a for the fcc phase. This simplifies the process, since only one nearest-neighbour bond length needs to be considered in the process. The unit cells were then compressed and extended isotropically from 85 % to 130 % of the equilibrium reference value in order to describe a representative range of possible bond lengths. The final cutoff radius for the repulsive potential is shown in Table 7.2.

A similar procedure was applied to the calculation of the Hf-Hf repulsive interaction. In this case, the hcp phase was used with a varying lattice constant a extending from 90 % to 130 % of the equilibrium reference value a=3.1967 Å [178]. The obtained cutoff radii can be seen in Table 7.2.

Interaction	Reference system	Cutoff radius [Å]
Hf-Hf	hcp	4.4
Hf-O	fcc	3.0

TABLE 7.2: Cutoff values for the repulsive potentials for the different interactions. Reprinted with permission from [175]. Copyright 2018 by the American Physical Society.

7.1.3 Amorphous hafnia models

Generating the classical models

To enlarge the structure sizes of amorphous HfO_2 systems to nanometer scale classical MD simulations have been applied. The forces between the different species were calculated using the Born-Mayer-Buckingham potential function (BMB).

$$V(r_{ij}) = Ae^{-\frac{r_{ij}}{\rho}} - \frac{C}{r_{ij}^6} + \frac{q_i q_j}{4\pi\varepsilon_0 r_{ij}} \tag{7.1}$$

The parameters for the distinct elements are obtained from Ref. [181] and presented in Table 7.3, while spherically truncated, pairwise $\frac{1}{r}$ summation was used for the summation of the Coulomb interactions [182]. The real space cut-off for the Coulomb interactions was defined to be 12 $\mathring{A}$ and 8 $\mathring{A}$ for the short range interactions, respectively.

The velocity Verlet algorithm as introduced in Chapter 4 was used for the time integration with a time step of 1 fs. The simulation temperature was set to 300

Element	Charge	A [eV]	ρ [Å]	C
Hf	+4	1454.6	0.350	0.0
O	-2	22764.3	0.149	20.4

TABLE 7.3: Parameters for the applied Born-Mayer-Buckingham potential function. Reprinted with permission from [175]. Copyright 2018 by the American Physical Society.

K, accordingly to characteristic temperatures in IBS coating processes. Two different models were realized, a condensed periodic bulk system and a classical grown thin film structure. A density of 8.60 g/cm^3 was set for the bulk structure. This is in agreement with other studies on amorphous HfO_2 [183]. The structure consists of 2400 atoms, 800 Hf atoms and 1600 O atoms. The applied temperature of 300 K was controlled by the Andersen thermostat (see Chapter 4) over a timespan of 20 ps.

The thin film structure on the other hand was calculated by employing a developed layer growth model algorithm [184, 185] based on classical MD. The atoms, which form the thin film, are successively deposited on a pre-defined substrate, which is basically a relaxed hafnia structure consisting of 9600 atoms. Since the growth should only happen along the c-direction, periodic boundary conditions were applied for the in-plane direction. Two successive steps modeled the coating process. First, a microcanonical ensemble ensures an optimal energy of the entry atoms and second, a canonical ensemble cools the system down to 300 K. Thus, the total time integration is about 1 ps for one deposition step and the corresponding kinetic deposition energy was set to 5 eV.

However, due to higher oxygen reflection as described in [186], additional low energetic O atoms were incorporated into the system after a certain number of deposited atoms. This can be understood as providing additional oxygen gas in the coating chamber during an experimental thin film coating process.

The described procedure was repeated until in total 78586 atoms were deposited onto the substrate, resulting in a total number of 88186 atoms with a film thickness of around 18 nm.

Generating the quantum mechanical models

The generated sk files were used in DFTB MD simulations of amorphous HfO_2 systems. In addition two larger models have been generated using a classical potential described before. Table 7.4 gives an overview of the different models. To generate a reasonable initial structure for the DFTB MD simulation, the atoms

Model	ρ [g/cm^3]	N	N_{Hf}	N_O	a [Å]	b [Å]	c [Å]
DFTB-I	7.97	300	100	200	16.368	16.368	16.368
DFTB-II	8.50	300	100	200	16.021	16.021	16.021
DFTB-III	8.93	300	100	200	15.760	15.760	15.760
DFTB-IV	9.39	300	100	200	15.498	15.498	15.498
DFTB-V	10.0	300	100	200	15.176	15.176	15.176
BMB-VI	8.60	2400	800	1600	35.229	40.679	22.680
BMB-VII	8.50	88186	29438	58748	70.458	81.358	212.32
DFT-VIII	9.39	96	32	64	10.601	10.601	10.601

TABLE 7.4: Overview of the geometric input data for the different models. N denotes the number of atoms and a, b, c denote the side lengths of the supercells. DFTB-I to DFTB-V refer to structures calculated using the DFTB method, while BMB-VI and BMB-VII refer to structures calculated with the Born-Mayer-Buckingham potential and DFT-VIII refers to an ab initio work [170] used for comparison. Reprinted with permission from [175]. Copyright 2018 by the American Physical Society.

were chemically and spatially randomly distributed in a three dimensional supercell with periodic boundary conditions to model a gas of hard spheres. By doing this, any memory effects and unphysical repulsive forces at the beginning of the simulation are avoided. For the DFTB simulations, a simulated annealing strategy was applied in the cooling procedure, using the Andersen thermostat (see Chapter 4) in an exponential path from 5000 K towards 300 K over 23 ps. In total, 24000 steps with one step consisting of 40 atomic time units ($1\tau = 2.419 \cdot 10^{-17}\, s$) were performed. The first 500 steps served as an equilibrating process. During this dynamic quench process, the Andersen thermostat creates a canonical NVT-ensemble. One DFTB structure is displayed in figure 7.1 as an example.

7.1.4 Results

Crystal phases

This section will cover the results for crystalline hafnium, crystalline hafnia, and amorphous hafnium oxide, which were obtained with the created new parameters. All aforementioned crystal phases of hafnium and hafnia will be used as target systems to assess the performance of the created DFTB parametrization.

As a first step, the band structures will be compared to reference DFT ones. The figures 7.2 and 7.3 provide a comparison between the band structures calculated with the PBE functional within DFT and DFTB for the crystal phases. All DFTB

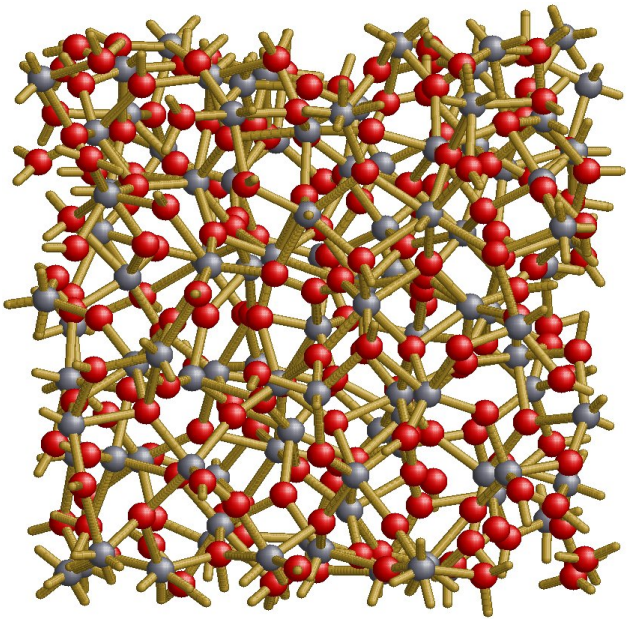

FIGURE 7.1: Structural snapshots of an amorphous HfO_2-network at a density of $\rho = 8.93\,\mathrm{g/cm^3}$. Reprinted with permission from [175]. Copyright 2018 by the American Physical Society.

band structures show an excellent agreement with the respective DFT calculations. Especially the general shapes match well. With one exception at the W-point in the bcc band structure, where the deviation is approximately 1 eV, the general deviation is smaller than 0.5 eV, in most parts far smaller.

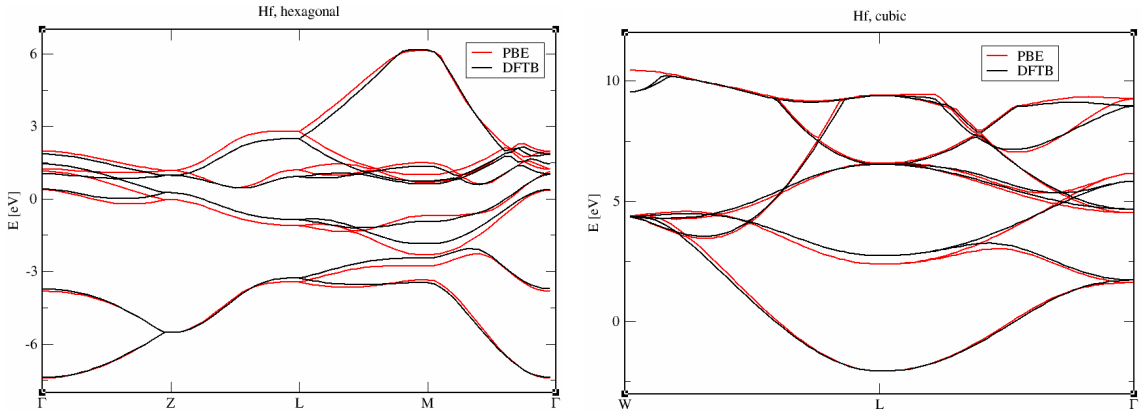

FIGURE 7.2: Band structures for hcp and bcc hafnium. Comparison between PBE (red) and DFTB (black). Reprinted with permission from [175]. Copyright 2018 by the American Physical Society.

It is important to point out that hafnium also suffers from the GGA band gap problem. DFT-GGA calculates a band gap of $E_{\mathrm{gap}} = 3.98\,\mathrm{eV}$ [187] for monoclinic HfO_2, a significant underestimation of the experimental gap, which lies between

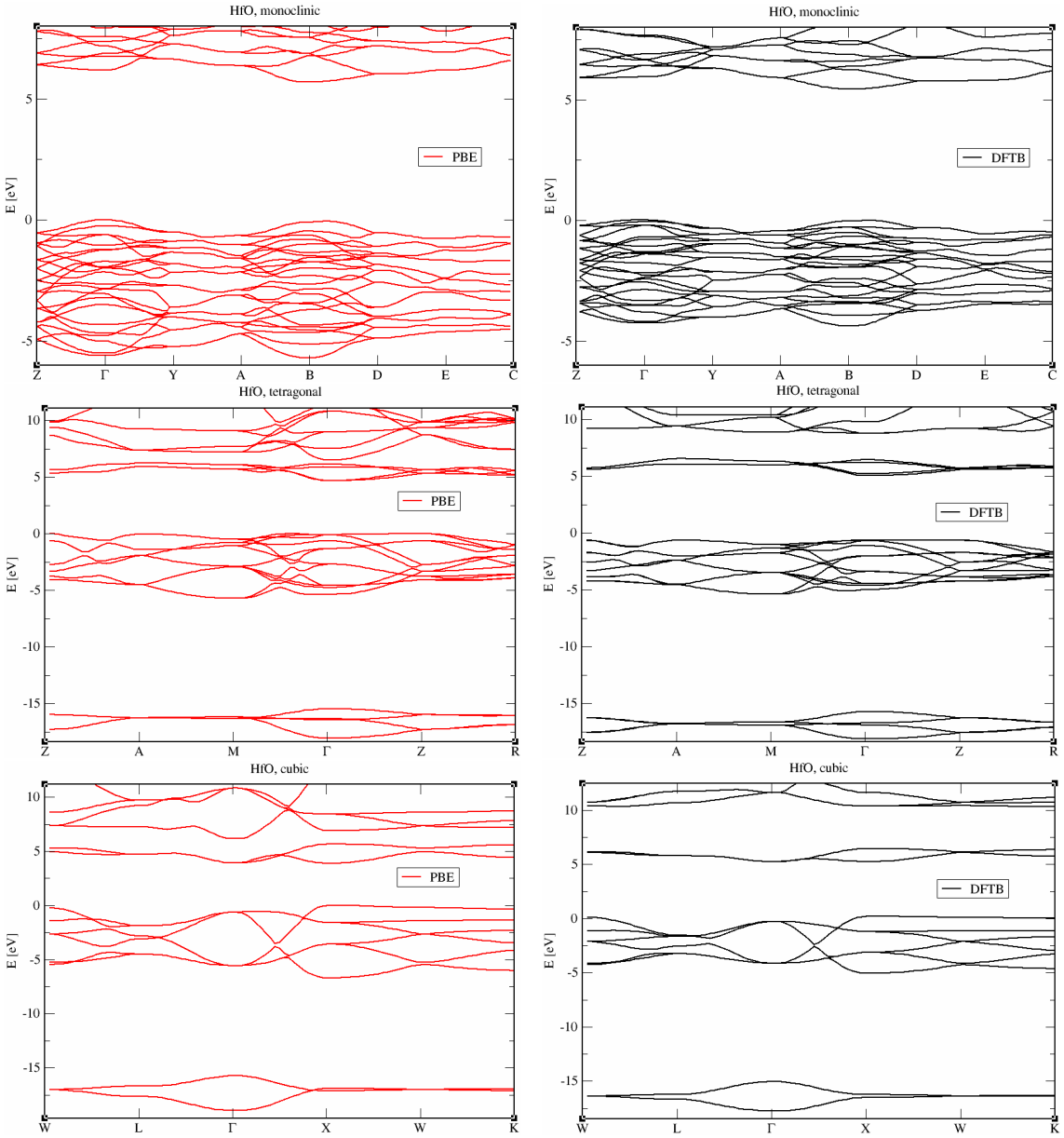

FIGURE 7.3: Band structures for monoclinic, fcc and tetragonal hafnium oxide. Comparison between PBE (red) and DFTB (black). Reprinted with permission from [175]. Copyright 2018 by the American Physical Society.

$E_{\text{gap}}^{\text{exp}} = (5.30 - 5.85)\,\text{eV}$ [188, 189]. Therefore, an uniform shift of the conduction bands was performed in order to match the experimentally found gap with DFTB. This resulted in a band gap of $E_{\text{gap}} = 5.65\,\text{eV}$ in the DFT reference. Finally, DFTB yielded a band gap of $E_{\text{gap}} = 5.40\,\text{eV}$ for monoclinic hafnia, a value within the experimental range.

As a second step, formation energies and bond lengths will be compared with the

DFT reference in order to further assess the performance of the DFTB parametrization. Table 7.5 presents the results. DFTB identifies the most stable phases of

		$E_{\text{formation}}$ [eV]		d [Å]	
model	phase	VASP	DFTB	VASP	DFTB
Hf	hcp	0	0	3.157-5.155	3.171-5.152
Hf	bcc	+0.186	+0.390	3.528	3.529
HfO_2	mono	0	0	2.033-2.231	2.037-2.223
HfO_2	tetra	+0.092	+0.289	2.056-2.366	2.048-2.350
HfO_2	fcc	+0.262	+0.235	2.169	2.196

TABLE 7.5: Formation energies per atom and bond lengths compared between DFT and DFTB. Formation energies of the most stable phases are set to 0 eV by definition. Reprinted with permission from [175]. Copyright 2018 by the American Physical Society.

hafnium and hafnia correctly. However, the energetic phase ordering for HfO_2 is incorrect. The high temperature phases fcc and tetragonal are exchanged with an energy difference of 0.054 eV per atom. But it is important to point out that the energy difference in the DFT reference is also just 0.17 eV per atom. Therefore, these results are very sensitive to any approximations and chosen values in DFTB.

The bond lengths are being reproduced excellently with DFTB. The deviation is below 1.4 % for all systems. Consequently, the parametrization performs very well.

Amorphous models

After this successful test on crystal phases, the created sk files were used to investigate amorphous systems with different densities in order to investigate their structural and electronic properties. Additionally, the results will be compared to other theoretical models using ab initio and classical approaches.

First, the structural properties will be discussed. As introduced in Chapter 4, the pair distribution function provides access to distance correlations in the discussed models and consequently enables the description of bond lengths, bond angles, and coordination numbers. Figure 7.4 presents the partial pair distribution functions of all DFTB systems and one DFT result from [170] for the Hf-Hf, Hf-O, and O-O correlations. Fig. 7.5 shows the pair distribution functions for the classical models in comparison with one DFTB structure having similar density. The graphs show no significant influence of the varying density.

Furthermore, they agree qualitatively well with the depicted DFT ab initio work. This observation does also hold true for the bond lengths, which are shown in

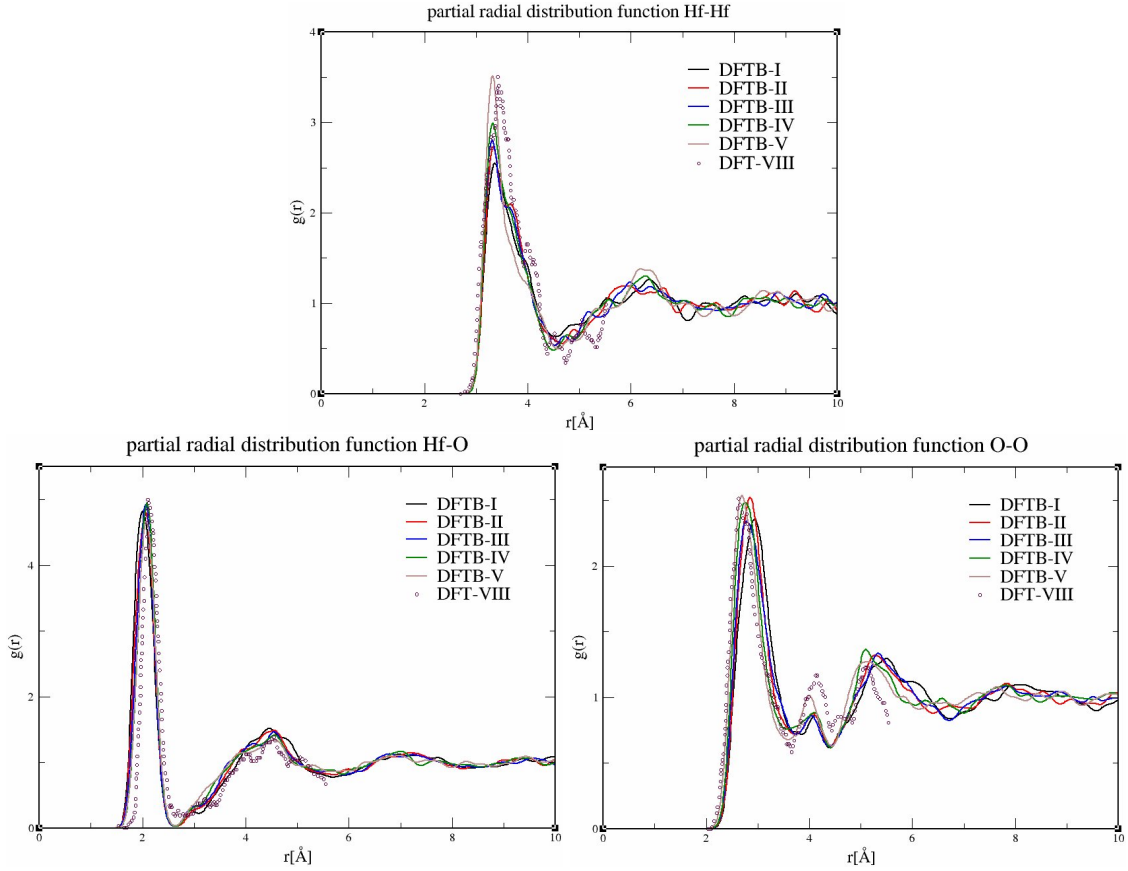

FIGURE 7.4: Partial pair distribution functions for the hafnium-hafnium, hafnium-oxygen and oxygen-oxygen correlation. Reprinted with permission from [175]. Copyright 2018 by the American Physical Society.

table 7.6. In addition, an increasing density induces slightly decreasing bond lengths for Hf-Hf and O-O correlations, whereas it causes the Hf-O bond length to remain almost constant in the DFTB calculations. At the same time, the resulting partial distribution functions and bond lengths also agree well with the models obtained by classical-potential MD growth and MD condensation simulations. In particular the locations of the minima and maxima and the general shape of the curves are almost identical. Especially R_1^{Hf-Hf} and R_1^{Hf-O} fit nicely into the trend. However, R_1^{O-O} is slightly smaller with 2.83 $\mathring{A}$ (BMB-VI) and 2.91 $\mathring{A}$ (BMB-VII) in the classical models compared to the DFTB values of $2.93 - 3.12$ $\mathring{A}$. A possible reason for this is the increased coordination number as discussed in the next paragraph. The only discrepancy is noticeable in the Hf-Hf pair distribution functions for the large-scale classical models. In contrast to both the DFTB structures and the ab initio model, they do not show the two peak structure in the first coordination shell, which is a result of differently coordinated polyhedra

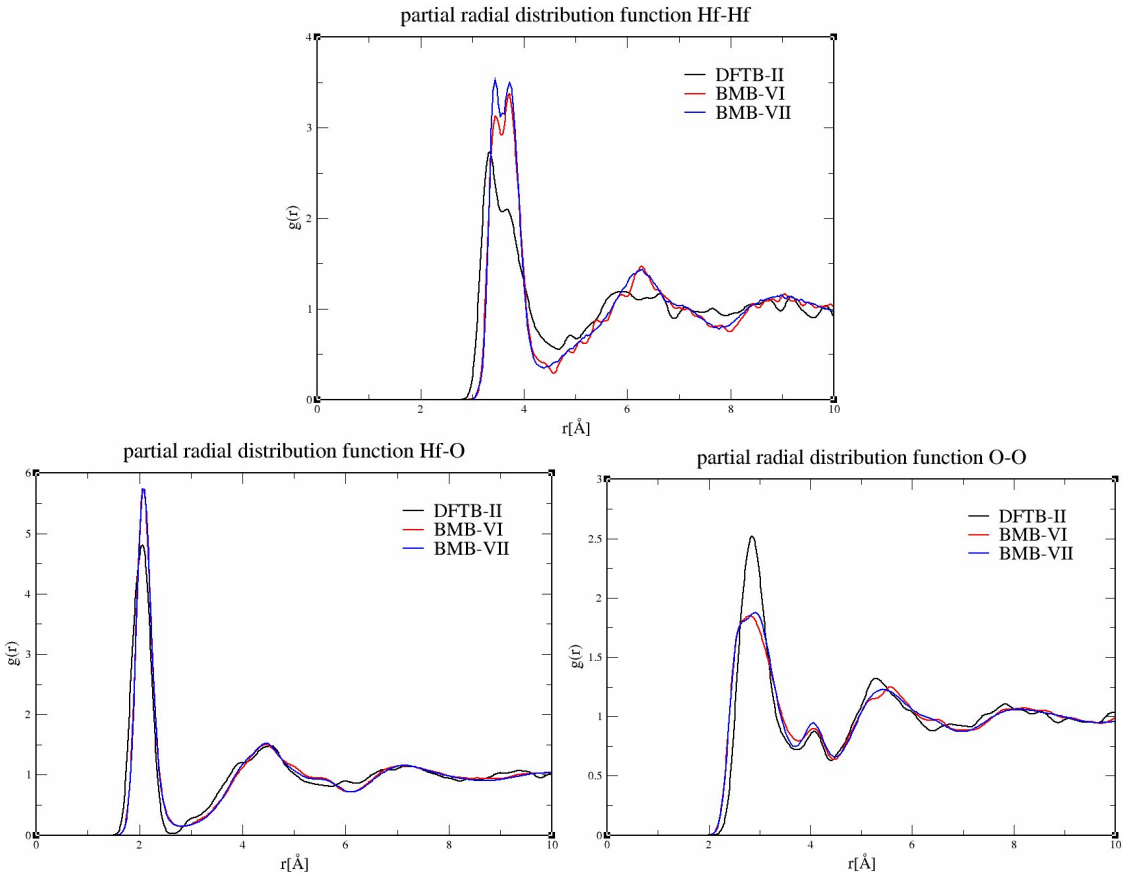

FIGURE 7.5: Partial pair distribution functions for the hafnium-hafnium, hafnium-oxygen and oxygen-oxygen correlation in comparison to the two classical models. Reprinted with permission from [175]. Copyright 2018 by the American Physical Society.

within the amorphous network. But since the classical models contain significantly more atoms, DFTB studies on larger HfO_2 systems might reproduce this feature.

The discussed partial pair distribution functions provide access to the description of coordination numbers, which are displayed in Table 7.7. Coordination numbers can be obtained by integrating the first coordination shell of the respective pair distribution function (first maximum) until a certain cutoff value. In this case, the cutoff radius for the Hf-O interaction is $r_{cutoff} = 2.6$ Å based on the first minimum in the corresponding partial pair distribution function.

The values for the DFTB simulations are consistently slightly lower compared to the other theoretical works. The best agreement between the coordination numbers calculated for the different DFTB models and other investigated theoretical works is obtained with the classically grown model based on the potential employed by Lewis et al. [181] (BMB-VII). So a DFTB model of comparable size may

Model	ρ [g/cm^3]	$R_1^{\text{Hf-Hf}}$ [Å]	$R_1^{\text{Hf-O}}$ [Å]	$R_1^{\text{O-O}}$ [Å]
DFTB-I	7.97	3.73	2.04	3.12
DFTB-II	8.50	3.77	2.06	3.03
DFTB-III	8.93	3.70	2.07	3.04
DFTB-IV	9.39	3.68	2.09	2.96
DFTB-V	10.0	3.67	2.09	2.93
BMB-VI	8.60	3.68	2.08	2.83
BMB-VII	8.50	3.66	2.09	2.91
DFT-VIII	9.39	3.50	2.06	2.75

TABLE 7.6: Average bond lengths for all systems. Reprinted with permission from [175]. Copyright 2018 by the American Physical Society.

Model	ρ [g/cm^3]	$K_{\text{Hf-O}}$	4-fold	5-fold	6-fold	7-fold	8-fold
DFTB-I	7.97	5.20	17.0%	49.0%	33.0%	1.0%	0.0%
DFTB-II	8.50	5.46	7.0%	45.0%	46.0%	2.0%	0.0%
DFTB-III	8.93	5.58	1.0%	45.0%	48.0%	6.0%	0.0%
DFTB-IV	9.39	5.87	0.0%	29.0%	55.0%	16.0%	0.0%
DFTB-V	10.0	6.08	0.0%	19.0%	54.0%	26.0%	1.0%
BMB-VI	8.60	6.05	0.1%	17.3%	60.7%	21.3%	0.6%
BMB-VII	8.50	5.92	0.7%	21.0%	64.2%	13.8%	0.3%
DFT-VIII	9.39	6.49	-	-	-	-	-

TABLE 7.7: Coordination numbers for a-HfO_2. $K_{\text{Hf-O}}$ denotes the average number of oxygen atoms bonding to a hafnium atom. A more detailed overview of the coordination numbers was not available for model DFT-VIII, thus only the average number is given here. Reprinted with permission from [175]. Copyright 2018 by the American Physical Society.

show similar coordination numbers. A very evident observation is the increasing coordination number $K_{\text{Hf}-\text{O}}$ for an increasing mass density ρ. $K_{\text{Hf-O}}$ seems to approach the value of the most stable monoclinic phase with increasing density, $K_{\text{Hf}-\text{O}} = 7$. But an ideal value will never be reached in amorphous structures due to the admixture and unordered arrangement of different crystalline structures. Figure 7.6 visualized this finding for the DFTB structures with the lowest and highest densities, respectively.

The next structural property to discuss are bond angles. Analogous to the description of bond lengths in amorphous systems, bond angles are not sharply defined, but widely distributed among a certain range. An overview of the different angles can be seen in Fig. 7.7. Model BMB-VII was too large to investigate all angle correlations, therefore, only the bond angle distributions Hf-O-Hf and

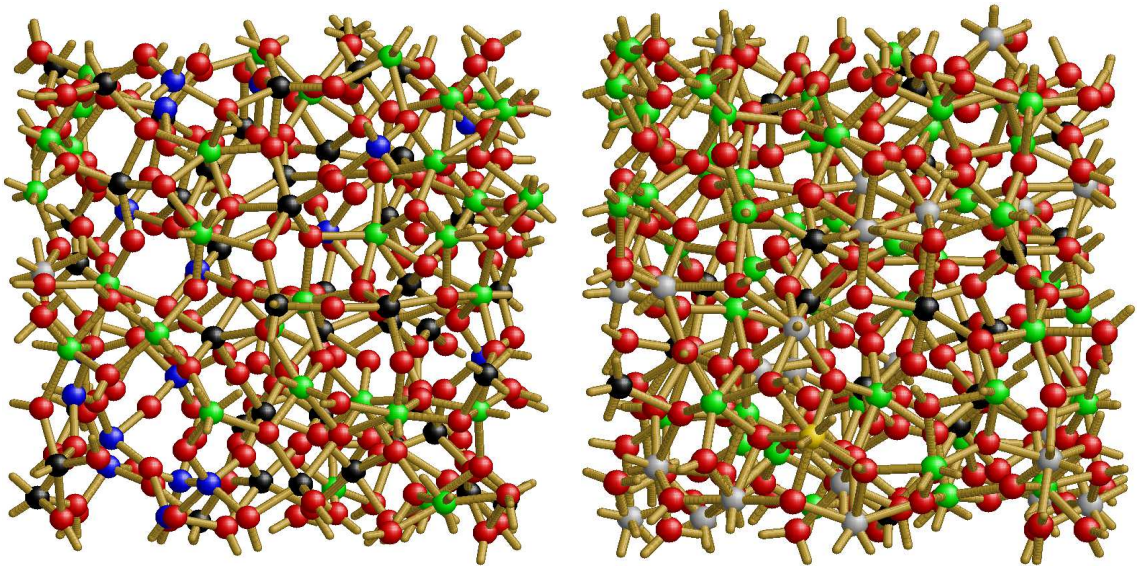

FIGURE 7.6: Comparison of the coordination numbers for $\rho = 7.97 \frac{g}{cm^3}$ (left) and $\rho = 10.0 \frac{g}{cm^3}$ (right). Oxygen is presented in red, 4-fold hafnium in blue, 5-fold in black, 6-fold in green, 7-fold in grey, and 8-fold hafnium in gold. Reprinted with permission from [175]. Copyright 2018 by the American Physical Society.

O-Hf-O will be discussed for this system. In general all the depicted angles agree well among both models. Especially the Hf-Hf-O, Hf-O-O and O-O-O curves show an almost identical course. The Hf-Hf-Hf, Hf-O-Hf and O-Hf-O curves also show a similar course between DFTB and the classic calculation, but their peaks are shifted slightly. Again, this might be related to the coordination numbers. Nevertheless, the qualitative agreement is still good. It is also important to point out that the classical models generate smoother distributions, a result of the larger system size.

Finally, the electronic properties of a-HfO_2 will be discussed, since it is considered as a possible substitute for SiO_2 in optical devices. Figure 7.8 displays the electronic density of states (EDOS) for the DFTB structures and the smaller classical structure BMB-VI. The curves do not show any significant differences among each other. So the mass density does not influence the qualitative course of the EDOS significantly. Neither does the applied functional as the comparison with the classical grown model demonstrates. Furthermore, the VBM stems mainly from O-*p* orbitals, while the conduction band edge consists primarily of contributions from Hf-*d* orbitals. These orbital characters do not change in a significant manner for the different models. Figure 7.9 visualizes this result. It should be noted, that all structures consistently show clean energy band gaps, so no defects caused by direct Hf-Hf or O-O bonds occur, thus providing well-defined HOMO-LUMO gaps.

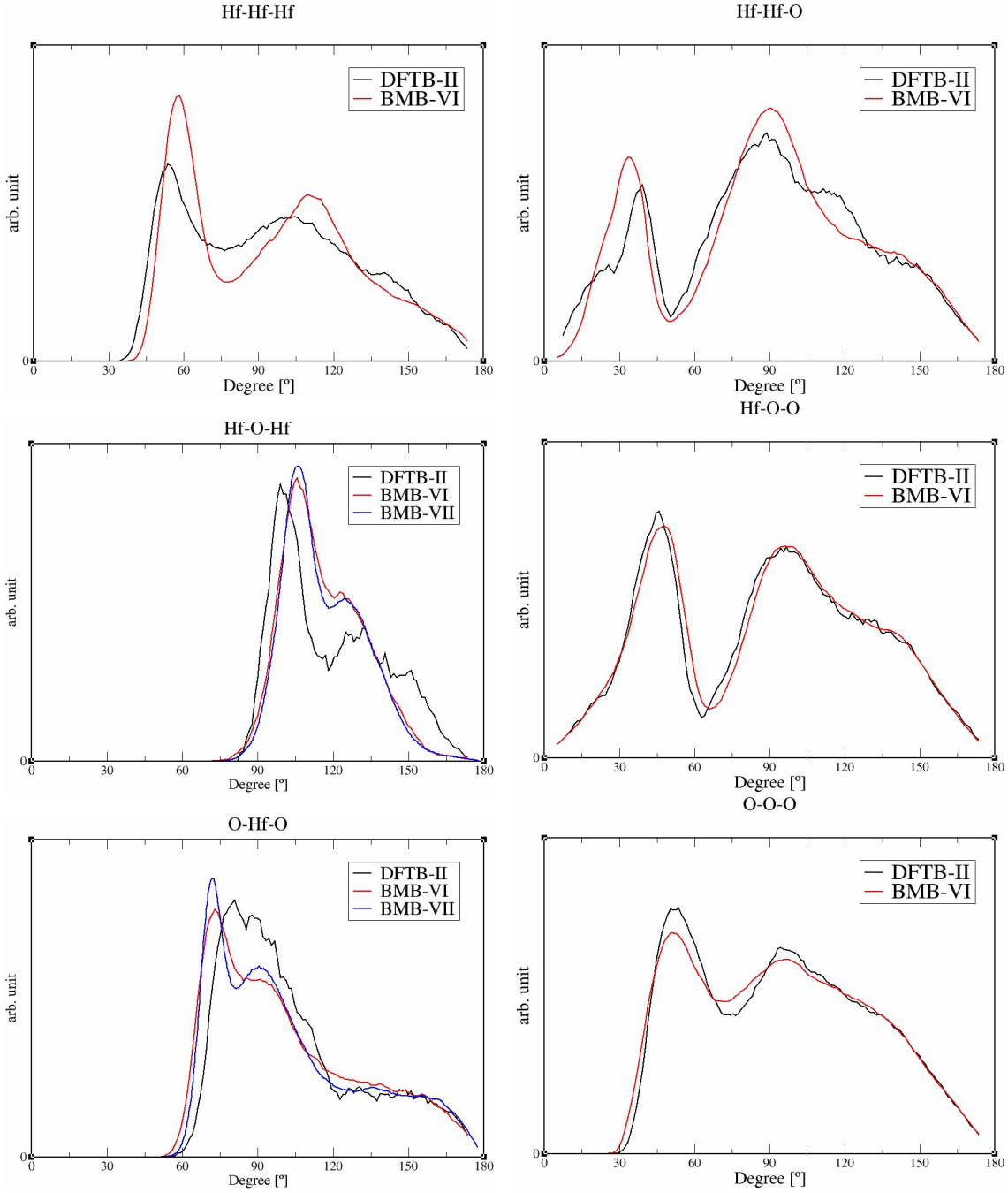

FIGURE 7.7: Angle distributions for the models DFTB-II, BMB-VI and BMB-VII. Reprinted with permission from [175]. Copyright 2018 by the American Physical Society.

The resulting band gaps are summarized in table 7.12 and compared to values obtained in other theoretical works. With one exception for $\rho = 8.50\,\mathrm{g/cm^3}$, the size of the band gap is slightly linear decreasing with increasing density for the DFTB runs. Furthermore, the values between $4.15\,eV < E_{gap} < 4.68\,eV$ indicate an insulating nature for a-HfO_2. The results also agree well with both the work

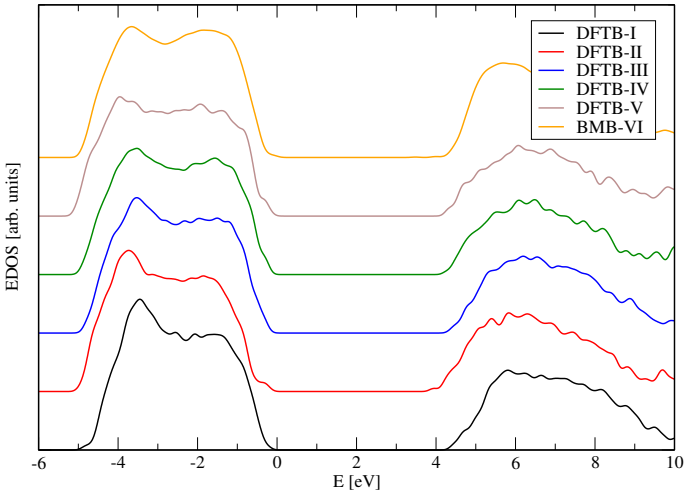

FIGURE 7.8: Electronic density of states for the five DFTB models and one classical structure.

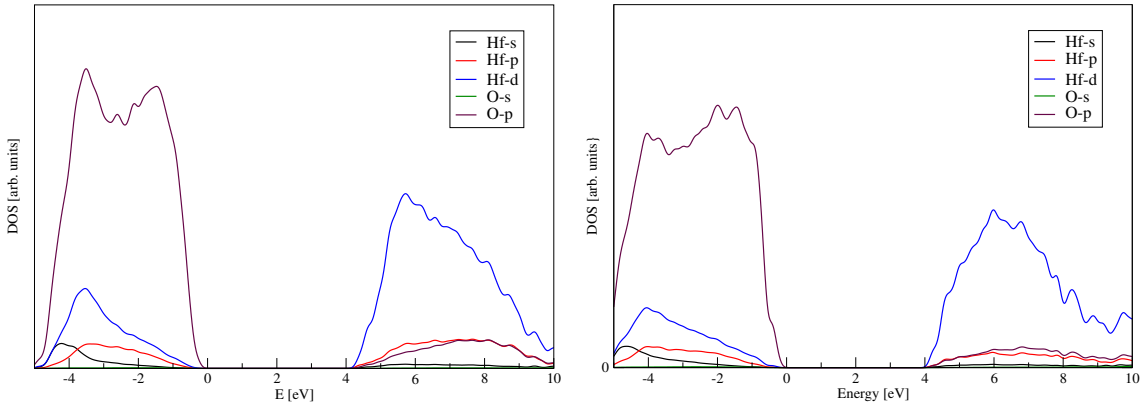

FIGURE 7.9: Projected density of states for DFTB-I (left) and DFTB-V (right). The VBM was shifted to 0 eV in both cases.

Model	$\rho\ [\frac{g}{cm^3}]$	E_{gap} [eV]
DFTB-I	7.97	4.66
DFTB-II	8.50	4.21
DFTB-III	8.93	4.49
DFTB-IV	9.39	4.53
DFTB-V	10.0	4.48
BMB-VI	8.60	3.52
DFT-VIII	9.39	3.80

TABLE 7.8: Calculated band gaps for the amorphous structures. The result for DFT-VIII was obtained using GGA without a correction of the band gap problem. Reprinted with permission from [175]. Copyright 2018 by the American Physical Society.

of Chen and Kuo [190] and the classical model. They applied both, a GGA functional and a PBE0 hybrid density functional and obtained $E_{gap} = 3.61\,eV$ and $E_{gap} = 5.90\,eV$, respectively. The GGA ab initio work DFT-VIII reflects this as well with $E_{gap} = 3.80\,eV$. Interestingly, the classical MD condensation simulation yields $E_{gap} = 3.52\,eV$, a value in the same range. Those results demonstrate, that the applied functional influences the value in a significant way.

Since a variety of defects can occur in amorphous systems, the density of states for an oxygen vacancy inserted into a monoclinic supercell was also investigated to assess how well the parametrization handles a common defect like this and ultimately legitimize it for the investigation of amorphous structures. Figure 7.10 presents the resulting curve and compares it to a DFT reference result obtained with PBE. Both graphs show an intra-gap state. It is located at VBM + 2.5 eV for

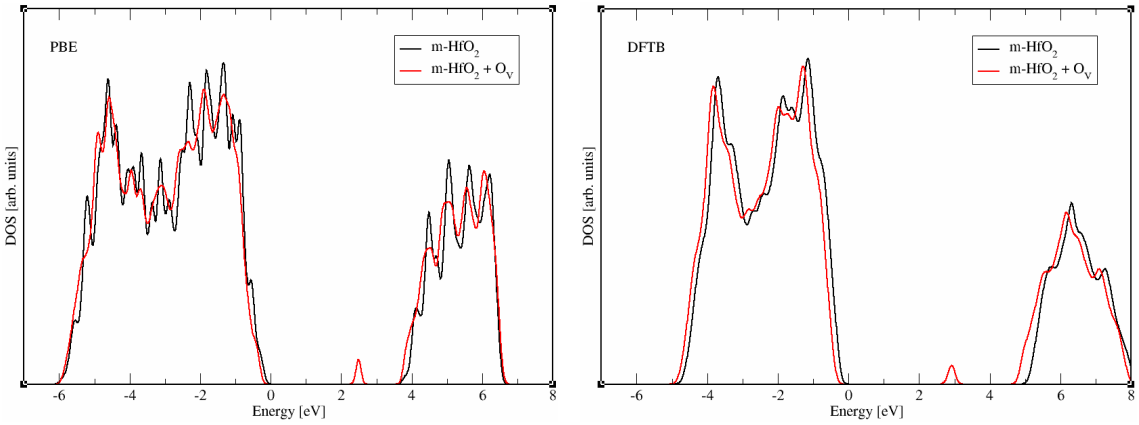

FIGURE 7.10: Density of states for the oxygen vacancy defect in monoclinic hafnia calculated with PBE (top) and DFTB (bottom). The valence band maximum was shifted to 0 eV in both cases. Reprinted with permission from [175]. Copyright 2018 by the American Physical Society.

the DFT and at VBM + 3.0 eV for the DFTB method. It is important to mention that it is not possible to compare the exact locations of these defect states, since hafnia suffers from the GGA band gap problem and therefore the band gap is 1.4 eV smaller than the respective DFTB band gap. The overall agreement of both DOS is very well.

7.2 $HfSiO_4$

The previous section covered results on amorphous hafnia and motivated why it is an important study. But besides pure hafnia, hafnium silicate is also widely used as a replacement of silicon oxide for gate dielectrics [191]. Hafnium silicates possess the same advantages over silcon oxide as hafnia, however, they

have a lower permittivity. Nevertheless, they are still of great interest, because they can resist high temperatures longer in their amorphous phase compared to hafnia, which consequently leads to lower leakage currents [192]. Furthermore, hafnium silicates form naturally at the interface between a SiO_2 substrate and the HfO_2 film during growth processes. Therefore, is is important to extend the HfO_2 parametrization by Si in order to provide a full set of sk files for the description of $Hf_xSi_{1-x}O_2$ structures.

7.2.1 Parametrization procedure

In order to describe $Hf_xSi_{1-x}O_2$ systems with DFTB, interaction with silicon had to be added to the created hafnia parametrization. The compression radii and basis set were taken from the existing pbc set [193]. Since the electronic part of the pbc O-O sk-file is the same as the one from the mio O-O sk-file, no band structure fitting had to be done. The Hf-Si repulsive was fitted on a artificially created tetragonal $HfSiO_4$ unit cell consisting of 24 atoms. All Hf-Si bond lengths were the same. This simplifies the process tremendously. The cell was then compressed and expanded isotropically from 78 % to 110 % of that reference to obtain an array of target systems. The fitting procedure itself was done analogous to the described procedure for hafnium. The difference between the DFT and DFTB coherence energy curves with respect to varying values of the lattice constant a for that artificial system was fitted. The cutoff radius is 3.30 Å.

7.2.2 Results

Applying the final set of sk-files to the $HfSiO_4$ cell, the Si-O and Hf-O bond lengths deviated by less than 1 % compared to the reference PBE values. Furthermore, no direct Hf-Hf, Si-Si or Hf-Si bonds were formed, resulting in defect-free structures. As a next step, the validated parametrization were used to generate amorphous structures. Three models of the type $Hf_xSi_{1-x}O_2$ were created. In order to evaluate the effect of different ratios between HfO_2 and SiO_2, the values x = 0.25, 0.50, 0.75 were chosen. To model a realistic density, the joint-density for both oxides was used ($\rho_{HfO_2} = 9.70\,g/cm^3$, $\rho_{SiO_2} = 2.65\,g/cm^3$). The process to generate the amorphous models is described in Section 7.1.3.

The resulting DFTB models were compared to two works from the literature, a DFT study [194] as well as a classical approach [195]. Table 7.9 gives a quick overview of the different models and their parameters. The authors in [194] used the PBE functional within VASP to optimize the geometries and applied the PBE0 functional to get a more accurate description of the electronic properties. The authors in [195] on the other hand used a Morse-BKS combined two-body potential

Method	x	ρ [g/cm^3]	N	N_{Hf}	N_{Si}	N_{Si}	l [Å]
DFTB	0.25	4.41	300	25	75	200	15.43
DFTB	0.50	6.18	300	50	50	200	15.38
DFTB	0.75	7.94	300	75	25	200	15.35
DFT	0.25	3.85	96	8	24	64	-
DFT	0.50	5.44	96	16	16	64	-
DFT	0.75	7.04	96	24	8	64	-
M-BKS	0.25	4.08	648	54	162	432	-
M-BKS	0.50	5.64	648	108	108	432	-
M-BKS	0.75	7.28	648	162	54	432	-

TABLE 7.9: Overview of the geometric input data used for the different models. N denotes the number of atoms and l denotes the side length of the supercells. Information about l was not available for the models from [194] and [195].

to conduct a classical MD study. They developed this new potential by employing the widely used BKS silica potential as a basis [196]. By adding a Morse term to introduce control the degree of covalency, they overcame a major weakness of the BKS potential. They fitted the required parameters to DFT and experimental values. Figure 7.11 displays two of the DFTB structures.

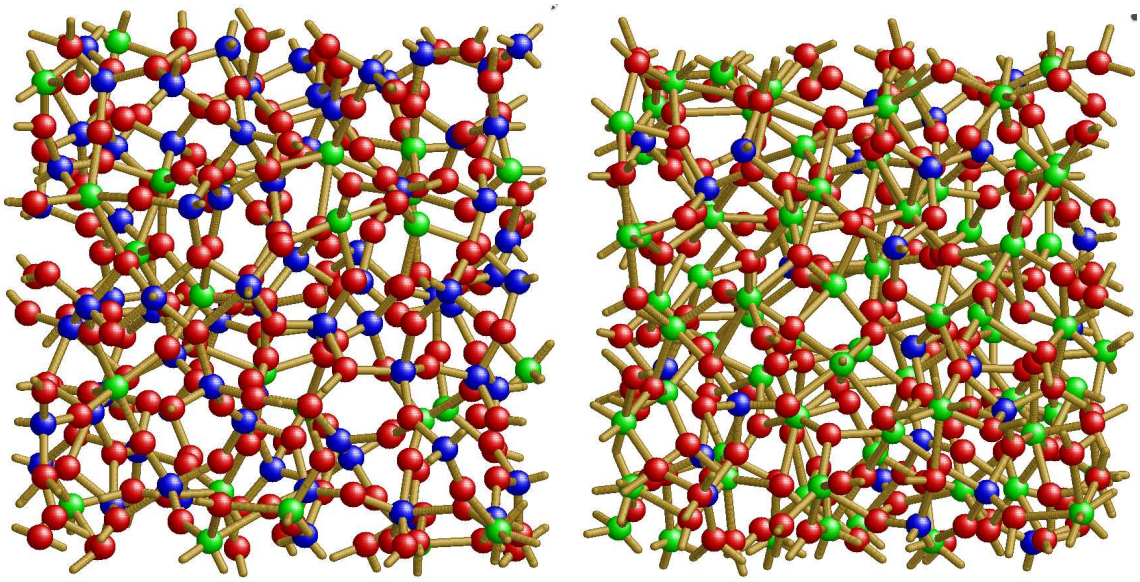

FIGURE 7.11: Structural snapshot of the amorphous $Hf_xSi_{1-x}O_2$ structures with x = 0.25 (left) and x = 0.75 (right). Hafnium, silicon, and oxygen atoms are represented by grey, blue, and red spheres, respectively.

First, the topological short-range order will be discussed. Therefore, Fig. 7.12 shows the partial pair distribution functions for the different models. For the

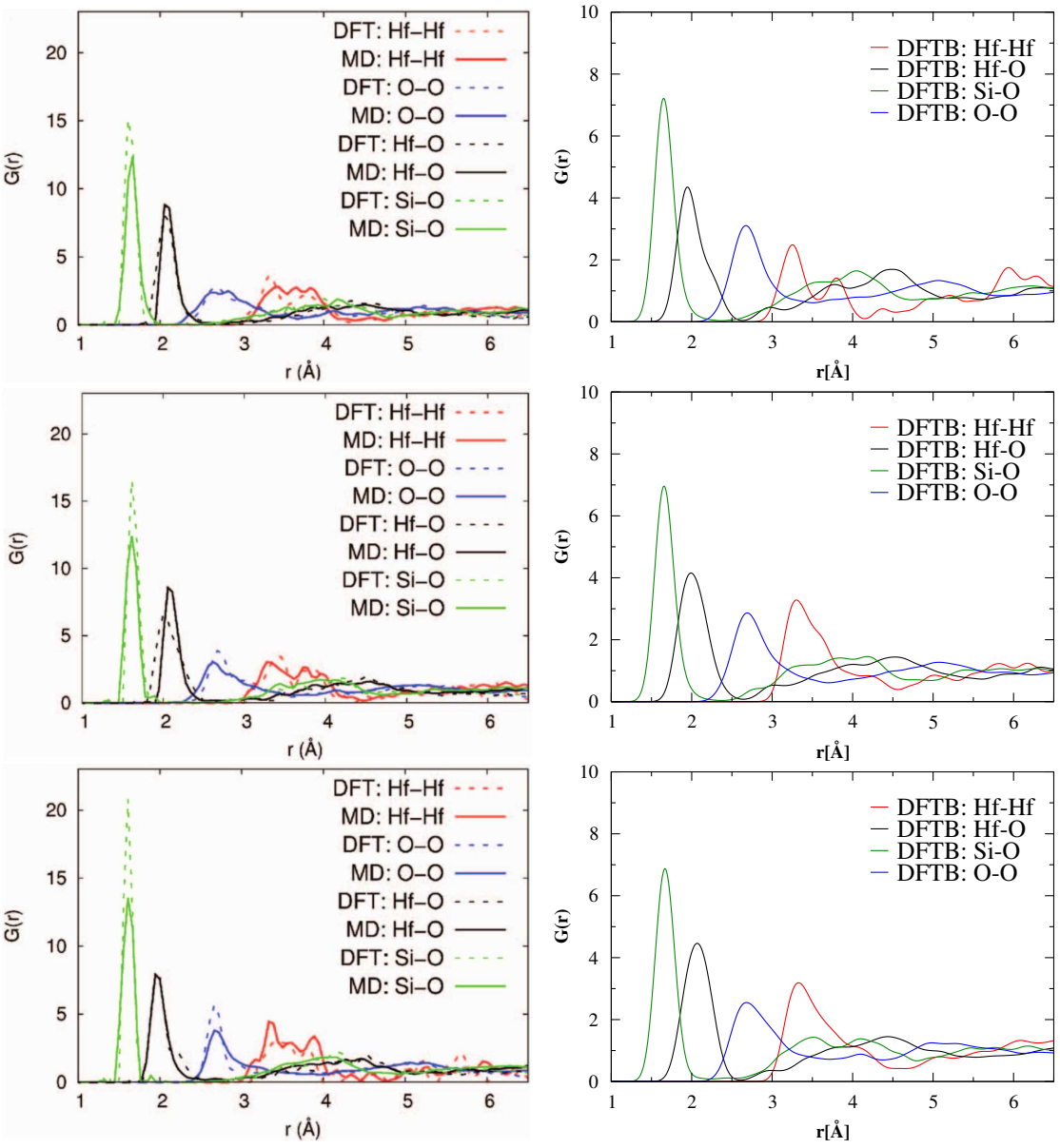

FIGURE 7.12: Partial pair distribution functions of the DFTB models (right) in comparison to the DFT and classical calculations (left). The pictures on the left were reprinted from [195], with the permission of AIP Publishing.

DFTB structures, only the Hf-Hf curve shows significant differences caused by the varying density. For 25 % HfO_2 contribution, the first Hf-Hf peak shows a well pronounced shoulder around 3.8 Å. With increasing HfO_2 contribution, this feature vanishes, resulting in an overall broader and higher peak. However, its location is not influenced significantly, the generated maxima are between 3.32 Å and 3.37 Å. This observation is in good agreement with the DFT calculation, which shows a similar picture. The classical MD study on the other hand yields a slightly different result. The Hf-Hf partial pair distribution function consists here

of three less pronounced subpeaks, indicating, that the classical potential generates a less homogeneic bond length distribution. Nevertheless, the maximum values are comparable with 3.35 Å < r < 3.48 Å for the DFT and 3.40 Å < r < 3.45 Å for the classical study.

This is also true for the Hf-O and Si-O curves. Both, the locations of the first minima and maxima agree very well with the respective results in [194] and [195] for Hf-O. For DFTB, the maxima are at 2.04 Å < r < 2.11 Å, meaning that an increasing density induces slightly increasing interatomic Hf-O distances, an observation that is reproduced in the DFT as well as in the classical study. It is important to point out that neither of these studies made any comments regarding broadening or normalization factors, therefore comparing the relative heights of the curves is not possible.

O-O partial pair distribution functions fit into the depicted trend. In particular the first maximum should be pointed out. Its general shape agrees exceptionally well among the three methods. It gets broader with increasing density without affecting the average bond lengths significantly. With 2.85 Å < r < 2.93 Å they are overall larger for the DFTB models compared to r = 2.70 Å for DFT and 2.65 Å < r < 2.75 Å for classical potentials. This feature was most likely carried over from the HfO_2 parametrization and stands in direct correlation to the coordination numbers as discussed in the next paragraph. These results are summarized in Table 7.10.

Method	x	$R_1^{\text{Hf-Hf}}$ [Å]	$R_1^{\text{Hf-O}}$ [Å]	$R_1^{\text{Si-O}}$ [Å]	$R_1^{\text{O-O}}$ [Å]
DFTB	0.25	3.32	2.04	1.68	2.85
DFTB	0.50	3.34	2.05	1.70	2.93
DFTB	0.75	3.37	2.11	1.70	2.89
DFT	0.25	3.48	2.05	1.65	2.70
DFT	0.50	3.43	2.11	1.65	2.70
DFT	0.75	3.35	2.11	1.66	2.70
M-BKS	0.25	3.45	2.05	1.65	2.70
M-BKS	0.50	3.40	2.10	1.65	2.65
M-BKS	0.75	3.40	2.10	1.70	2.75

TABLE 7.10: Resulting average bond lengths for all models.

Next, the coordination numbers will be discussed. The obtained values are displayed in Table 7.11. The overall agreement with the DFT values is good. The deviation is between 1.6 and 5.4 %. Furthermore, an increasing density results in larger coordination numbers for the Hf-O interaction. An interesting observation is the large jump for K_{Hf-O} from 25 % to 50 % HfO_2 contribution. Both methods produce this. On the other hand, although K_{Si-O} shows a good quantitative agreement, the qualitative trend does not agree between both approaches.

Method	x	$K_{Hf\text{-}O}$	$K_{Si\text{-}O}$
DFTB	0.25	5.04	4.23
DFTB	0.50	5.52	4.20
DFTB	0.75	5.72	4.20
DFT	0.25	4.92	4.00
DFT	0.50	5.73	4.06
DFT	0.75	5.81	4.12

TABLE 7.11: Coordination numbers for the DFTB and DFT structures. These data were not available for the M-BKS models.

Whereas the coordination numbers increase with increasing density ($4.00 < K_{Si-O} < 4.12$), they remain constant within the DFTB simulations ($4.20 < K_{Si-O} < 4.23$). However, it should be pointed out, that the DFT models consist of only 96 atoms due to the required computational resources, and therefore even one additional Si-O bond has a significant influence on the coordination number.

Since $Hf_xSi_{1-x}O_2$ systems play an important role as gate materials for optical devices, the electronic properties need to be determined as well. Thus, the electronic density of states for the DFTB structures can be seen in Fig. 7.13.

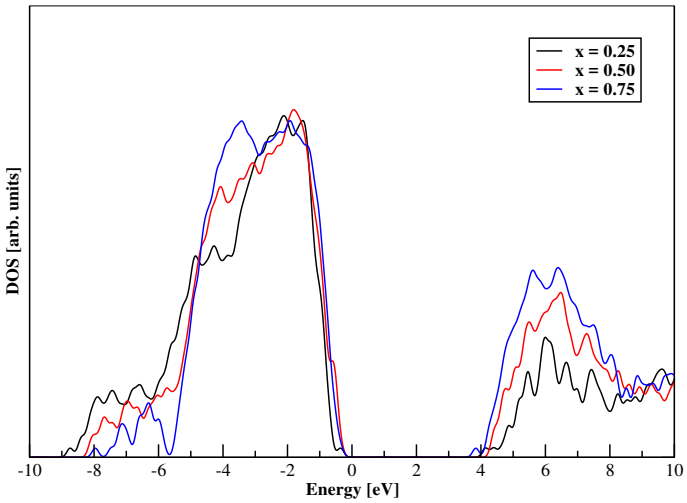

FIGURE 7.13: Electronic density of states for the different DFTB models. The VBM was shifted to 0 eV.

The curves do not show any significant differences among each other. So the mass density does not influence the qualitative course of the EDOS significantly. Neither does the applied functional as the comparison with the classical grown model demonstrates. The valence band maximum consists primarily of contributions from O_p orbitals, while the conduction band edge stems mainly of Hf_d orbitals. We like to point out, that these orbital characters do not change significantly for the different mass densities. It should be noted, that all structures

consistently show clean energy band gaps, so no defects caused by direct Hf-Hf or O-O bonds occur, thus providing well-defined HOMO-LUMO gaps. The resulting band gaps are summarized in table 7.12 and compared to values obtained in other theoretical works. There is a clear influence of the density visible, however, a trend cannot be identified. The obtained values are constantly below the DFT counterparts. A possible explanation is the applied functional in the DFT simulations. The authors in [194] used the PBE0 functional, whereas the obtained DFTB band gaps would probably agree better with PBE values. Ultimately meaning, that more models and stoichiometric ratios need to be investigated to get a more complete picture.

Method	x	E_{gap} [eV]
DFTB	0.25	4.49
DFTB	0.50	4.73
DFTB	0.75	3.97
DFT	0.25	6.38
DFT	0.50	6.24
DFT	0.75	6.08

TABLE 7.12: Calculated band gaps for the amorphous structures.

7.3 GaN

As described in Chapter 5, GaN is of huge interest for biomedical and optoelectronic applications [115–118]. Employing ab-initio methods leads to an accurate description of structural and optical properties, however, they are computationally very time-consuming and therefore limit the possible model size to a few hundred atoms at most, depending on the applied functional. If hybrid functionals are needed, the possible system size shrinks even more. In order to discuss larger systems and real molecules for surface functionalization purposes, a different approach is needed. Since DFTB allows the simulation of thousands of atoms, a parametrization needs to be created for the description of GaN. This Section covers the parametrization procedure and its evaluation on bulk and surface systems in order to approve it for further applications in the future.

7.3.1 Creating the reference data

Analogous to the parametrization procedure for hafnia, ab initio reference data had to be generated for parametrizing GaN. The computational details are the same. Table 7.13 gives details about the geometric parameters of the Ga and GaN

model	phase	parameter	value
Ga	ortho	a	4.52 Å
Ga	ortho	b	7.66 Å
Ga	ortho	c	4.53 Å
Ga	fcc	a	4.08 Å
Ga	mono	a	2.77 Å
Ga	mono	b	8.05 Å
Ga	mono	c	3.33 Å
Ga	mono	γ	92.0 °
Ga	tetra	a	2.80 Å
Ga	tetra	a	4.45 Å
GaN	wurtz	a	3.19 Å
GaN	wurtz	c	5.19 Å
GaN	zinc	a	4.50 Å
GaN	rock	a	4.18 Å

TABLE 7.13: Geometric parameters for the crystal phases of Ga and GaN.

crystal phases [197–202]. The calculations for gallium and gallium nitride were performed on a $12 \times 12 \times 12$ and $4 \times 4 \times 4$ Monkhorst-pack k-point mesh, respectively [21]. Furthermore, a plane wave basis with an energy cutoff of $E_c = 400\,\text{eV}$ has been used [19, 20]. The atomic structures were optimized using the PBE functional [33].

7.3.2 The parametrization procedure

In order to create the parameters which are needed for the DFTB application, both the electronic and the repulsive part of the interatomic interactions between two elements have to be computed as described in Chapter 3. The required data for the nitrogen-nitrogen interaction was taken from the established 3ob set for organic and biological systems [203]. Since one purpose of this GaN parametrization is the investigation of functionalized surfaces with organic molecules, this opens up the possibility to add the remaining elements in the 3ob set in a future work.

Electronic part

The electronic part contains Hamilton and overlap matrix integrals, which were calculated analogous to the procedure described for hafnia. In this case the same confinement radii were chosen for the orbitals and the density with a minimal

basis of only s and p orbitals. Unoccupied d orbitals were also considered during the process, but it turned out that this does not improve the resulting band structure. As a consequence, the final sk set uses only a minimal basis consisting of s and p orbitals in order to save computational effort. The resulting optimal confinement radius is 3.2 a_0.

Repulsive part

To generate the repulsive part for the Ga-Ga interaction, several systems were considered as the reference crystalline system. It turned out that the best results were obtained when an artificially constructed cubic cell was used. By doing this, only one bond length had to be considered, which simplified the process tremendously. A geometry optimized tetragonal Ga system was compressed along the c-axis to achieve this. The resulting cell was then compressed and expanded isotropically from 80 % to 130 % of that reference to obtain an array of target systems. The fitting procedure itself was done analogous to the described procedure for hafnium. The cutoff radius of the repulsive potential can be seen in Table 7.14.

For the generation of the GaN repulsive, the zincblende phase has been used, since it also contains only one nearest-neighbour bond length. The reference cell was compressed and extended isotropically from 80 % to 150 %. This range turned out to be optimal in order to describe a representative range of bond lengths in the systems. The cutoff radii are displayed in Table 7.14.

Interaction	Reference system	Cutoff radius [Å]
Ga-Ga	cubic	4.6
Ga-N	zinc	3.4

TABLE 7.14: Obtained cutoff values for the repulsive potentials of the different interactions.

7.3.3 Results

The created DFTB parametrization has to be evaluated in order to approve it for applications in the future. Its performance is tested for four crystal phases of gallium as well as for all three crystal phases of gallium nitride. Since the purpose of this GaN parametrization is the ability to describe surface systems and charge transfer phenomena correctly, it needs to describe the structural and energetic properties of the most important bulk phases of Ga and GaN accurately enough. Furthermore, the surface of interest also needs to be described well.

The figures 7.14 and 7.15 provide a comparison between the band structures calculated with PBE and DFTB for orthorhombic and fcc gallium as well as for wurtzite and zincblende gallium nitride.

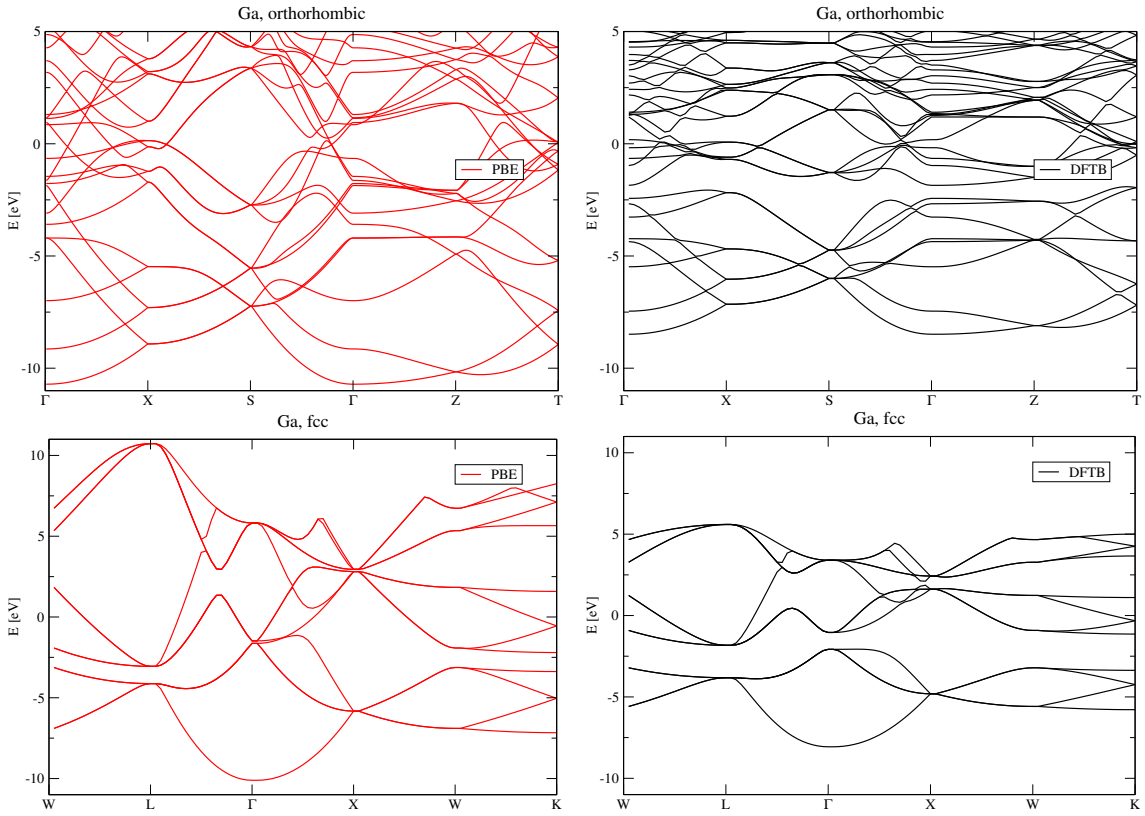

FIGURE 7.14: Band structures for orthorhombic and fcc gallium. Comparison between PBE (red) and DFTB (black). The fermi level was set to 0 eV.

For Ga, the DFTB band structures show an acceptable agreement with the PBE calculations. In the case of orthorhombic Ga, the qualitative shape of the bands is well described up until 0 eV, the higher energetic bands then begin to deviate strongly. For fcc Ga, a different picture is found. The whole band structure is strongly compressed, it covers a smaller energy interval compared to the PBE counterpart. However, the general shape of the PBE band structure is somewhat being reproduced. The aim of this parametrization is primarily the correct description of GaN and in order to obtain the best possible result, the Ga orbitals had to be compressed quite considerably. Whereas this leads to good results for GaN, the Ga band structures are too strongly compressed as a consequence, but the qualitative description is still acceptable for Gallium.

The DFTB band structures for GaN show an excellent agreement with the PBE equivalents especially for the valence bands. In addition, the first conduction band is also described well, which is important to be able to obtain an accurate

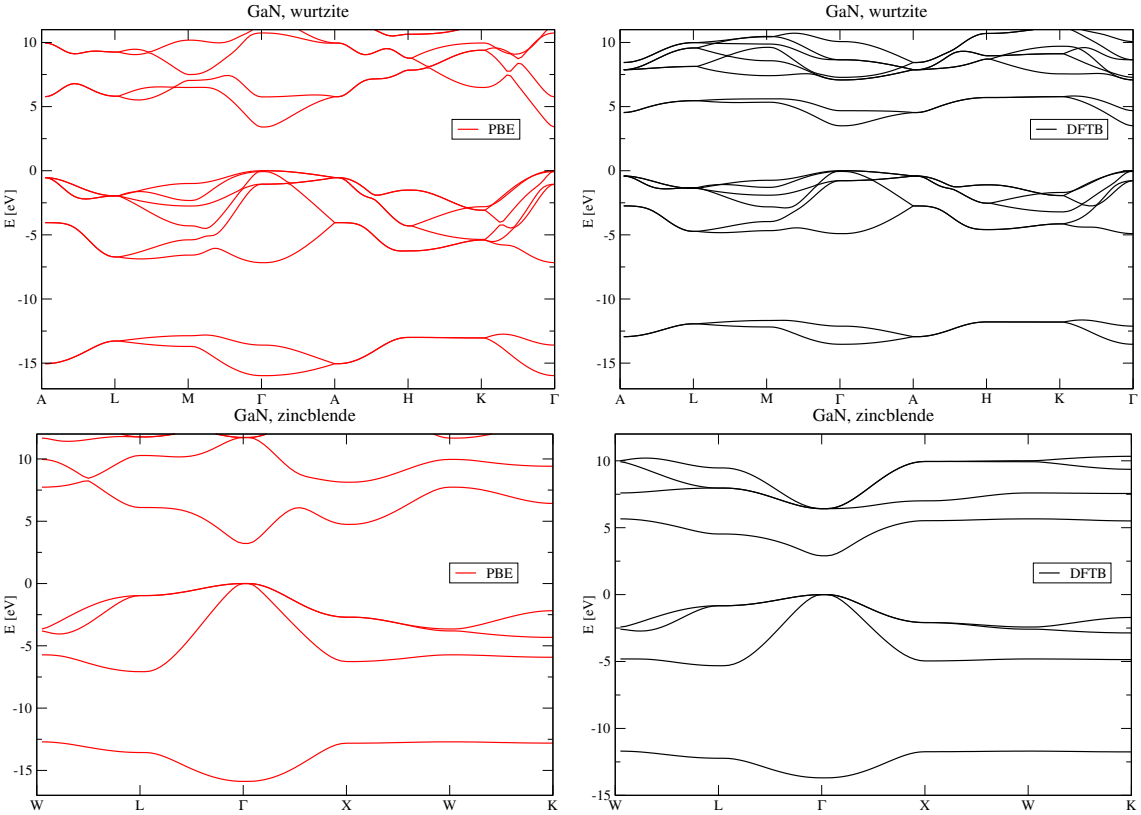

FIGURE 7.15: Band structures for wurtzite and zincblende gallium nitride. Comparison between PBE (red) and DFTB (black). The VBM has been shifted to 0 eV.

band gap. However, the effect of the strong compression can be seen here as well, since the conduction bands are a bit too flat in comparison to PBE.

Similar to the case of HfO_2, DFT-GGA underestimates the band gap for wurtzite GaN considerably with $E_{\text{gap}} = 2.4\,\text{eV}$ compared to the experimentally found gap of $E_{\text{gap}}^{\text{exp}} = 3.4\,\text{eV}$ [106]. In order to match the experimental gap, an uniform shift of the conduction bands was performed to obtain a band gap of $E_{\text{gap}} = 3.40\,\text{eV}$ in the DFT reference structure. The resulting DFTB band gap for wurtzite gallium nitride is $E_{\text{gap}} = 3.45\,\text{eV}$.

The next step is to compare the formation energies and bond lengths for all phases in order to assess the performance of the SK files. Table 7.15 displays the results. DFTB identifies the most stable phases correctly. However, the energy differences are very slim for PBE, the formation energy of the least stable tetragonal Ga phase is only 0.013 eV higher than the one for the most stable orthorhombic phase. Therefore, reproducing the correct phase ordering is a challenging task for a parameter-based method like DFTB. As a consequence, the fcc and monoclinic phases are exchanged. It is also important to mention, that for DFTB, the orthorhombic phase is the most stable with a margin of 0.128 eV, in contrast to

		$E_{\text{formation}}$ [eV]		d [Å]	
model	phase	VASP	DFTB	VASP	DFTB
Ga	ortho	0	0	2.537-2.814	2.716-2.820
Ga	fcc	+0.004	+0.315	2.993	2.990
Ga	mono	+0.008	+0.128	2.760-2.911	2.819-2.916
Ga	tetra	+0.013	+0.327	2.878-3.078	2.889-3.084
GaN	wurtz	0	0	1.985-1.991	2.049-2.050
GaN	zinc	+0.014	+0.026	1.987	2.048
GaN	rock	+0.801	+1.695	2.139	2.212

TABLE 7.15: Formation energies per atom (for GaN per Ga-N unit) and bond lengths compared between PBE and DFTB. Formation energies of the most stable phases are set to 0 by definition.

0.004 eV for PBE. For GaN the phase ordering is correct, even though the wurtzite and zincblende phases are of comparable stability.
Only the rocksalt phase is with 0.801 eV (PBE) and 1.695 eV (DFTB) energy difference significantly less stable. The bond lengths are in general well reproduced. With one exception for the orthorhombic phase with 7.1 %, the deviation is between 0.1 % and 3.4 % and therefore above acceptability. During the parametrization process it turned out to be apparently impossible to reproduce the geometric properties of the orthorhombic phases as well as the other Gallium phases without letting the results for GaN suffer considerably. Since an accurate description of the latter is more important for this study, it is a necessary and worthwhile tradeoff.

The final step for the assessment of the parametrization is a comparison between PBE and DFTB for a surface slab model of GaN. For this purpose the bare GaN-$(10\bar{1}0)$ surface model of Chapter 5 is used as the reference system. Figure 7.16 shows the respective band structures.
The band structures show a similar result as the bulk ones. While the valence bands are described very well, the conduction bands are too flat. Nevertheless the qualitative shape of the first conduction bands is acceptable in comparison to the reference.

Similar to the formation energies for bulk crystalline systems, an important value to evaluate the stability of surface models is the cleavage energy E_c. It basically describes how strong the bonds in the slab are. It can be calculated as follows

$$E_c = E_{\text{surface}} - nE_{\text{bulk}}, \tag{7.2}$$

where n is the number of bulk unit cells in the slab. Table 7.16 presents the calculated cleavage energies as well as the bond lengths for interactions inside the slab

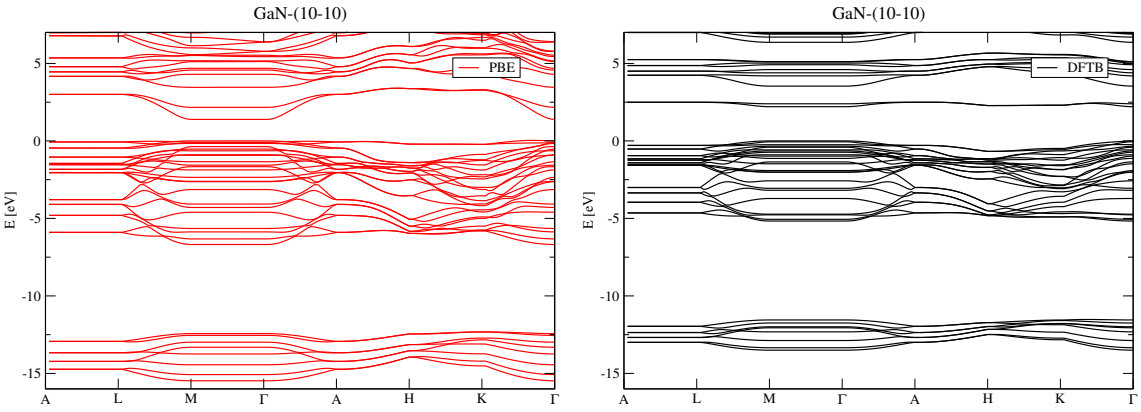

FIGURE 7.16: Band structures for a GaN-$(10\bar{1}0)$ surface. Comparison between PBE (red) and DFTB (black). The VBM has been shifted to 0 eV.

	E_c [eV]		d [Å]	
model	VASP	DFTB	VASP	DFTB
GaN-$(10\bar{1}0)$	0.665	0.884	1.983-2.061 (i)	2.015-2.115 (i)
			1.858 (o)	1.910 (o)

TABLE 7.16: Cleavage energy per Ga-N unit and bond lengths compared between PBE and DFTB for the GaN-$(10\bar{1}0)$ surface. i denotes bonds inside the slab, whereas o describes the Ga-N bond at the top of the slab.

(i) and on top of it (o). In this work, a DFT cleavage energy of $E_c^{DFT} = 0.665\,eV$ was calculated, whereas in the literature values up to $E_c^{DFT} = 0.975\,eV$ can be found [204]. The obtained DFTB value is $E_c^{DFTB} = 0.885\,eV$ and thus agrees very well with that range. The obtained bond lengths do also agree very well with the reference values. The deviation is between 1.61 % and 2.79 %. It is also important to point out that DFTB reproduces specific PBE results. For example does the Ga-N bond length directly on the surface (o) shrink from the bulk value of 1.99 Å to 1.86 Å. DFTB describes this behaviour qualitatively correctly.

Chapter 8

Concluding remarks

8.1 Summary

In this thesis, different DFT-based methods were employed to investigate crystalline and amorphous wide-bandgap semiconductors.

In Chapter 5, semilocal and hybrid functionals were employed to investigate the functionalization of ZnO and GaN surfaces. MPA-derived molecules with different carbon chain lengths have been attached to a slab model of ZnO in order to discuss the binding and optical properties. The monodentate mode was found to be the most stable one for all investigated chain lengths. Furthermore, intra-gap states appeared for all models. But the chain length does not influence the electronic and optical properties of the systems significantly, indicating that even small molecules could be used to tune the dielectric properties of such systems. Additionally, TDDFT was employed to validate these results on a more sophisticated level of accuracy. These findings agree well with experimental results.

This Chapter also presented the results for the functionalization of GaN surfaces with thiol, carboxyl, and amine groups. All groups were found to bind strongly to the surface. While a modification with carboxyl or amine groups did not influence the electronic properties of the systems in a significant way, functionalization with thiol groups lead to the appearance of intra-gap states. However, in contrast to the results for functionalized ZnO surfaces, these states are optically inactive.

The results for cobalt-doped ZnO nanostructures were discussed in Chapter 6. Standard DFT and the GW_0 approximation were employed to investigate the thermodynamical, structural, and electronic properties of different defect complexes in Co-doped ZnO. Co_{Zn}+Zn_{int} and Co_{Zn}+O_{int} complexes were identified as possible sources for the optical activity of Co in ZnO. However, due to a very high formation energy of the Co_{Zn}+Zn_{int} defect complex, the optical activity was attributed to Co_{Zn}+O_{int} complexes.

Chapter 7 discussed the results for DFTB parametrizations and respective applications for HfO_2, $Hf_xSi_{1-x}O_2$, and GaN. A new parametrization for HfO_2 is

presented and validated against DFT reference data. The resulting band structures showed a very good agreement with the DFT counterparts and the band gap of 5.40 eV lies within the experimental range. Furthermore, the obtained bond lengths for all crystal phases of hafnium and hafnia deviated up to 1.4 % from reference values, which is a very good agreement. That parametrization was then used to calculate amorphous HfO_2 structures with different densities in order to see, how the density influences the resulting structural and electronic properties. These results were compared to DFT data from the literature and classically obtained models, which were provided by collaboration partners from hannover, with good agreement.

This Chapter also extended the parametrization by silicon in order to be able to describe $Hf_xSi_{1-x}O_2$ systems. The results for three different stoichiometric ratios agreed well with DFT and classical MD results, making this set of sk files promising for further studies in the future.

Finally, a new parametrization for GaN was presented and validated against DFT reference data. Compared to the HfO_2 parametrization, the obtained results are not of the same quality, however, the GaN band structures showed a good qualitative agreement with DFT equivalents. Calculated bond lengths differed by 0.1 % to 7.1 %.

8.2 Outlook

This work could stimulate further projects in the future. Intra-gap states for thiol groups on GaN surfaces were found to be optically inactive. More functional groups need to be investigated in order to obtain more knowledge about the possibility to tune optical properties of GaN-based nanostructures. Additionally, as a follow-up, GaN nanowires could be investigated using the aforementioned functional groups, once suitable ligands are identified.

Furthermore the GaN parametrization for DFTB could be combined with other elements of the corresponding DFTB data set for in order to enable functionalization of GaN surfaces with organic molecules in DFTB. Ultimately this could be extended to the description of nanowires of reasonable sizes, which is nowadays still impossible with standard DFT methods. This field of research is still less advanced than the investigation of ZnO nanostructures. DFT and DFTB approaches could be combined at this point for a more complete and efficient study.

The functionalization of ZnO surfaces with MPA molecules showed very promising results for optoelectronic applications. This opens up the possibility to extend this study to more complex systems.

Appendix A

Acknowledgements

First I express my sincere gratitude to my supervisor Prof. Dr. Thomas Frauenheim for the continuous support of my PhD study and related research. He gave me the chance to work on this project in the first place. My sincere thanks also goes to Dr. Michael Lorke and Prof. Dr. Andreia Luisa da Rosa for their support, patience and knowledge. Their guidance helped me in the time of research and writing of this thesis. I thank Dr. Michael Lorke especially for proof-reading this thesis.

My special thanks goes to Dr. Bálint Aradi for his time and advise, whenever I needed help. I am also very grateful for his feedback on parts of this thesis. Another special thanks goes to my office colleague Patrick Karasch for all the science-related and unrelated discussions. Having you as my office colleague made the time much more enjoyable.

I am grateful to Dr. Christof Köhler for always fixing any computer-related problems without hesitation. Sandra Smit and Svenja Wehr are gratefully acknowledged for helping me whenever I encountered problems with bureaucracy. My thanks also goes to the DFG and the FOR1616 research group for funding this project.

I am deeply grateful to my family for their endless and unconditional love and support. In particular my mom, my brother, my dad, Liane and my grandparents. You believed in me even in times where I got off track. I will never forget this.

And finally to Helena, who stepped into my life at a crucial point of my PhD study and without whom this thesis would not exist. You showed me that there are things worth fighting for. Thank you for being a part of my life and having believed in me from the very first second. You make me a better person. And always remember: It's just physics.

Appendix B

List of Publications

Parts of this thesis are based on publications. The following list will give an overview of the individual contributions of the author to these publications.

- D. Franke, C. Hettich, T. Köhler, M. Turowski, H. Ehlers, D. Ristau, and T. Frauenheim, *Density functional based tight-binding parametrization of hafnium oxide: Simulations of amorphous structures*, Phys. Rev. B **98**, 075207, 2018.

  Statement: The author wrote all parts of the paper with the exception of the part regarding the generation of amorphous models using classical potentials. He rewrote that part for this thesis. He further did all the DFTB simulations and analysed the data.

- D. Franke, M. Lorke, T. Frauenheim, and A. L. Rosa, *Hybrid Density-Functional Theory Calculations of Electronic and Optical Properties of Mercaptocarboxylic Acids on ZnO-(10$\bar{1}$0) Surfaces*, J. Phys. Chem. C. **2018** 122(43), 24838-24842.

  Statement: The author did all calculations with the exception of the TDDFT calculation. He analysed the data and provided the pictures. M. Lorke and A. L. Rosa helped in writing the paper. The author rewrote the text for this thesis.

- D. Franke, M. Lorke, T. Frauenheim, and A. L. Rosa, *Electronic and Optical Properties of Functionalized GaN-(10$\bar{1}$0) Surfaces using Hybrid-Density Functionals*, Phys. Status Solidi B, accepted.

  Statement: The author did all calculations and the analysis. He wrote the paper together with M. Lorke and A. L. Rosa. The author rewrote the text for this thesis.

- D. Franke, M. Lorke, T. Frauenheim, and A. L. Rosa, *Co-doped ZnO within the GW approximation*, in preparation.

  Statement: The author did all calculations and the analysis. He further wrote the paper. A. L. Rosa performed the GW convergence tests and helped in writing and improving the text. The author rewrote the text for this thesis.

- R. Röder, S. Geburt, M. Zapf, D. Franke, M. Lorke, T. Frauenheim, and A. L. Rosa, and C. Ronning, *Transition metal and rare earth element doped ZnO nanowires for optoelectronics*, Phys. Status Solidi B, accepted.

  Statement: The author provided text and pictures for DFT calculations of Co_{Zn}+O_{int} defect complexes in ZnO.

Bibliography

[1] *Renewables 2018 Global Status Report*. REN21, 2018.

[2] R. Fu et al. *NREL U.S. Solar Photovoltaic System Cost Benchmark: Q1 2017*. National Renewable Energy Laboratory, 2012.

[3] R. Cariou et al. "III-V-on-silicon solar cells reaching 33 % photoconversion efficiency in two-terminal configuration". In: *Nature Energy* 3 (2018), pp. 326–333.

[4] Nadarajah Kannan and Divagar Vakeesan. "Solar energy for future world: - A review". In: *Renewable and Sustainable Energy Reviews* 62 (2016), pp. 1092–1105. ISSN: 1364-0321.

[5] The Hong Kong Polytechnic University. *Perovskite-silicon tandem solar cells with the world's highest power conversion efficiency*. 2016. URL: `https://www.sciencedaily.com/releases/2016/04/160412104814.htm` (visited on 11/30/2018).

[6] J. Bardeen and W. H. Brattain. "The Transistor, A Semi-Conductor Triode". In: *Phys. Rev.* 74 (2 1948), pp. 230–231.

[7] D. A. Buchanan. "Scaling the gate dielectric: materials, integration and reliability". In: *IBM J. Res. Develop.* 43 (2002), pp. 245–264.

[8] M. Bidaud et al. "1.5–2.5 nm RTP gate oxides: process feasibility, properties and limitations". In: *J. Non-Cry. Sol.* 280 (2001), pp. 32–38.

[9] *The rapid transition to energy efficient lighting: an integrated policy approach*. The United Nations Environment Programme, 2013.

[10] *LEDs and the worldwide market for lighting fixtures*. CSIL, 2018.

[11] "Facile fabrication of electrochemical ZnO nanowire glucose biosensor using roll to roll printing technique". In: *Sensors and Actuators B: Chemical* 247 (2017), pp. 807–813. ISSN: 0925-4005. DOI: `https://doi.org/10.1016/j.snb.2017.03.105`.

[12] R. O. Jones. "Density functional theory: Its origins, rise to prominence, and future". In: *Rev. Mod. Phys.* 87 (3 2015), pp. 897–923.

[13] Kieron Burke. "Perspective on density functional theory". In: *The Journal of Chemical Physics* 136.15 (2012), p. 150901.

[14] R. G. Parr and W. Yang. "Density-functional theory of atoms and molecules". In: New York: University Oxford Press, 1989.

[15] D. R. Hartree. "The Wave Mechanics of an Atom with a Non-Coulomb Central Field. Part I. Theory and Methods". In: *Mathematical Proceedings of the Cambridge Philosophical Society* 24.1 (1928), 89–110.

[16] V. Fock. "Näherungsmethode zur Lösung des quantenmechanischen Mehrkörperproblems". In: *Zeitschrift fur Physik* 61 (1930), pp. 126–148.

[17] P. Hohenberg and W. Kohn. "Inhomogeneous Electron Gas". In: *Phys. Rev.* 136 (3B 1964), B864–B871.

[18] W. Kohn and L. J. Sham. "Self-Consistent Equations Including Exchange and Correlation Effects". In: *Phys. Rev.* 140 (4A 1965), A1133–A1138.

[19] G. Kresse and D. Joubert. "From ultrasoft pseudopotentials to the projector augmented-wave method". In: *Phys. Rev. B* 59.3 (1999), p. 1758.

[20] P. Bloechl. "Projector Augmented-wave Method". In: *Phys. Rev. B* 50 (1994), pp. 17953–17979.

[21] Hendrik J. Monkhorst and James D. Pack. "Special points for Brillouin-zone integrations". In: *Phys. Rev. B* 13 (12 1976), pp. 5188–5192.

[22] P. A. M. Dirac. "Note on Exchange Phenomena in the Thomas Atom". In: *Mathematical Proceedings of the Cambridge Philosophical Society* 26.3 (1930), 376–385.

[23] D. M. Ceperley and B. J. Alder. "Ground State of the Electron Gas by a Stochastic Method". In: *Phys. Rev. Lett.* 45 (7 1980), pp. 566–569.

[24] J. P. Perdew and Alex Zunger. "Self-interaction correction to density-functional approximations for many-electron systems". In: *Phys. Rev. B* 23 (10 1981), pp. 5048–5079.

[25] John P. Perdew and Yue Wang. "Accurate and simple analytic representation of the electron-gas correlation energy". In: *Phys. Rev. B* 45 (23 1992), pp. 13244–13249.

[26] Axel D. Becke. "Perspective: Fifty years of density-functional theory in chemical physics". In: *The Journal of Chemical Physics* 140.18 (2014), 18A301.

[27] John P. Perdew et al. "Atoms, molecules, solids, and surfaces: Applications of the generalized gradient approximation for exchange and correlation". In: *Phys. Rev. B* 46 (11 1992), pp. 6671–6687.

[28] John P. Perdew and Wang Yue. "Accurate and simple density functional for the electronic exchange energy: Generalized gradient approximation". In: *Phys. Rev. B* 33 (12 1986), pp. 8800–8802.

[29] A. D. Becke. "Density-functional exchange-energy approximation with correct asymptotic behavior". In: *Phys. Rev. A* 38 (6 1988), pp. 3098–3100.

[30] Chengteh Lee, Weitao Yang, and Robert G. Parr. "Development of the Colle-Salvetti correlation-energy formula into a functional of the electron density". In: *Phys. Rev. B* 37 (2 1988), pp. 785–789.

[31] John P. Perdew and Yue Wang. "Accurate and simple analytic representation of the electron-gas correlation energy". In: *Phys. Rev. B* 45 (23 1992), pp. 13244–13249.

[32] Larry A. Curtiss et al. "Gaussian2 theory for molecular energies of first and secondrow compounds". In: *The Journal of Chemical Physics* 94.11 (1991), pp. 7221–7230.

[33] J. P. Perdew, K. Burke, and M. Ernzerhof. "Generalized gradient approximation made simple". In: *Phys. Rev. Lett* 77.18 (1996), pp. 3865–3868.

[34] L. J. Sham and M. Schlüter. "Density-Functional Theory of the Energy Gap". In: *Phys. Rev. Lett.* 51 (20 1983), pp. 1888–1891.

[35] John P Perdew et al. "Understanding band gaps of solids in generalized Kohn–Sham theory". In: *Proceedings of the National Academy of Sciences* 114.11 (2017), pp. 2801–2806.

[36] J. F. Janak. "Proof that $\frac{\partial E}{\partial n_i} = \epsilon$ in density-functional theory". In: *Phys. Rev. B* 18 (12 1978), pp. 7165–7168.

[37] Axel D. Becke. "A new mixing of Hartree–Fock and local densityfunctional theories". In: *The Journal of Chemical Physics* 98.2 (1993), pp. 1372–1377.

[38] Axel D. Becke. "Densityfunctional thermochemistry. III. The role of exact exchange". In: *The Journal of Chemical Physics* 98.7 (1993), pp. 5648–5652.

[39] P. J. Stephens et al. "Ab Initio Calculation of Vibrational Absorption and Circular Dichroism Spectra Using Density Functional Force Fields". In: *The Journal of Physical Chemistry* 98.45 (1994), pp. 11623–11627.

[40] Carlo Adamo and Vincenzo Barone. "Toward reliable density functional methods without adjustable parameters: The PBE0 model". In: *The Journal of Chemical Physics* 110.13 (1999), pp. 6158–6170.

[41] Matthias Ernzerhof and Gustavo E. Scuseria. "Assessment of the Perdew Burke Ernzerhof exchange-correlation functional". In: *The Journal of Chemical Physics* 110.11 (1999), pp. 5029–5036.

[42] J. Paier et al. "Screened hybrid density functionals applied to solids". In: *The Journal of Chemical Physics* 124.15 (2006), p. 154709.

[43] J. Heyd, G. E. Scuseria, and M. Ernzerhof. In: *J. Chem. Phys.* 118 (2003), p. 8207.

[44] Erich Runge and E. K. U. Gross. "Density-Functional Theory for Time-Dependent Systems". In: *Phys. Rev. Lett.* 52 (12 1984), pp. 997–1000.

[45] Robert van Leeuwen. "Causality and Symmetry in Time-Dependent Density-Functional Theory". In: *Phys. Rev. Lett.* 80 (6 1998), pp. 1280–1283.

[46] L. D. Landau. "The Theory of a Fermi Liquid". In: *J. Exp. Theor. Phys.* 30 (1956), 1058–1064.

[47] Lars Hedin. "New Method for Calculating the One-Particle Green's Function with Application to the Electron-Gas Problem". In: *Phys. Rev.* 139 (3A 1965), A796–A823.

[48] Lars Hedin and Stig O. Lundqvist. "Effects of Electron-Electron and Electron-Phonon". eng. In: ed. by Frederick Seitz, David Turnbull, and Henry Ehrenreich. Vol. 23. Solid State Physics. Academic Press, 1969, pp. 1–181.

[49] David Bohm and David Pines. "A Collective Description of Electron Interactions. I. Magnetic Interactions". In: *Phys. Rev.* 82 (5 1951), pp. 625–634.

[50] David Pines and David Bohm. "A Collective Description of Electron Interactions: II. Collective vs Individual Particle Aspects of the Interactions". In: *Phys. Rev.* 85 (2 1952), pp. 338–353.

[51] David Bohm and David Pines. "A Collective Description of Electron Interactions: III. Coulomb Interactions in a Degenerate Electron Gas". In: *Phys. Rev.* 92 (3 1953), pp. 609–625.

[52] M. Shishkin and G. Kresse. "Implementation and performance of the frequency-dependent *GW* method within the PAW framework". In: *Phys. Rev. B* 74 (3 2006), p. 035101.

[53] M. Shishkin and G. Kresse. "Self-consistent *GW* calculations for semiconductors and insulators". In: *Phys. Rev. B* 75 (23 2007), p. 235102.

[54] M. Shishkin, M. Marsman, and G. Kresse. "Accurate Quasiparticle Spectra from Self-Consistent GW Calculations with Vertex Corrections". In: *Phys. Rev. Lett.* 99 (24 2007), p. 246403.

[55] G. Onida, L. Reining, and A. Rubio. "Electronic Excitations: Density-functional Versus Many-body Greens Function Approaches". In: *Rev. Mod. Phys.* 601-659 (2002), p. 2002.

[56] F Aryasetiawan and O Gunnarsson. "The GW method". In: *Reports on Progress in Physics* 61.3 (1998), p. 237.

[57] R. W. Godby, M. Schlüter, and L. J. Sham. "Quasiparticle energies in GaAs and AlAs". In: *Phys. Rev. B* 35 (8 1987), pp. 4170–4171.

[58] Mark S. Hybertsen and Steven G. Louie. "Electron correlation in semiconductors and insulators: Band gaps and quasiparticle energies". In: *Phys. Rev. B* 34 (8 1986), pp. 5390–5413.

[59] F. Fuchs et al. "Quasiparticle band structure based on a generalized Kohn-Sham scheme". In: *Phys. Rev. B* 76 (11 2007), p. 115109.

[60] Joachim Paier, Martijn Marsman, and Georg Kresse. "Dielectric properties and excitons for extended systems from hybrid functionals". In: *Phys. Rev. B* 78 (12 2008), p. 121201.

[61] Ulf von Barth and Bengt Holm. "Self-consistent GW_0 results for the electron gas: Fixed screened potential W_0 within the random-phase approximation". In: *Phys. Rev. B* 54 (12 1996), pp. 8411–8419.

[62] M. Shishkin and G. Kresse. "Self-consistent *GW* calculations for semiconductors and insulators". In: *Phys. Rev. B* 75 (23 2007), p. 235102.

[63] Adrian Stan, Nils Erik Dahlen, and Robert van Leeuwen. "Levels of self-consistency in the GW approximation". In: *The Journal of Chemical Physics* 130.11 (2009), p. 114105.

[64] Iek-Heng Chu et al. "All-electron self-consistent *GW* in the Matsubara-time domain: Implementation and benchmarks of semiconductors and insulators". In: *Phys. Rev. B* 93 (12 2016), p. 125210.

[65] M. Elstner. "SCC-DFTB: What Is the Proper Degree of Self-Consistency?" In: *J. Phys. Chem. A* 111 (2007), pp. 5614–5621.

[66] C. Köhler, G. Seifert, and T. Frauenheim. "Density-Functional based calculations for Fe(n), (n32)". In: *Chem. Phys.* 309 (2005), p. 23.

[67] T. A. Niehaus et al. "Tight-binding approach to time-dependent density-functional response theory". In: *Phys. Rev. B* 63 (2001), p. 085108.

[68] A. Dominguez et al. "Extensions of the Time-Dependent Density Functional Based Tight-Binding Approach". In: *J. Chem. Theory Comput.* 9 (2013), pp. 4901–4914.

[69] Th. Frauenheim et al. "A Self-Consistent Charge Density-Functional Based Tight-Binding Method for Predictive Materials Simulations in Physics, Chemistry and Biology". In: *physica status solidi (b)* 217.1 (), pp. 41–62.

[70] W. Matthew C. Foulkes and Roger Haydock. "Tight-binding models and density-functional theory". In: *Phys. Rev. B* 39 (17 1989), pp. 12520–12536.

[71] J. C. Slater and G. F. Koster. "Simplified LCAO Method for the Periodic Potential Problem". In: *Phys. Rev.* 94 (6 1954), pp. 1498–1524.

[72] H. Eschrig. "Optimized LCAO Method and the Electronic Structure of Extended Systems". In: Berlin: Springer-Verlag, 1989.

[73] D. Porezag. "Development of Ab-Initio and Approximate Density Functional Methods and their Application to Complex Fullerene Systems". PhD thesis. Technical University of Chemnitz, 1997.

[74] G. Seifert, H. Eschrig, and W. Bieger. "Eine approximative Variante des LCAO-X_α-Verfahrens". In: *Z. Phys. Chem.* 267 (1986), p. 529.

[75] Thomas Frauenheim et al. "Atomistic simulations of complex materials: ground-state and excited-state properties". In: *Journal of Physics: Condensed Matter* 14.11 (2002), p. 3015.

[76] Robert G. Parr and Ralph G. Pearson. "Absolute hardness: companion parameter to absolute electronegativity". In: *Journal of the American Chemical Society* 105.26 (1983), pp. 7512–7516.

[77] Loup Verlet. "Computer "Experiments" on Classical Fluids. I. Thermodynamical Properties of Lennard-Jones Molecules". In: *Phys. Rev.* 159 (1 1967), pp. 98–103.

[78] William C. Swope et al. "A computer simulation method for the calculation of equilibrium constants for the formation of physical clusters of molecules: Application to small water clusters". In: *The Journal of Chemical Physics* 76.1 (1982), pp. 637–649.

[79] L. Boltzmann. *Vorlesungen über Gastheorie: Th. Theorie van der Waals'; Gase mit zusammengesetzten Molekülen; Gasdissociation; Schlussbemerkungen*. Vorlesungen über Gastheorie. J. A. Barth, 1898.

[80] R. M. Mazo. "Brownian motion: fluctuations, dynamics, and applications". In: Oxford University Press, 2002.

[81] A. Einstein. "Über die von der molekularkinetischen Theorie der Wärme geforderte Bewegung von in ruhenden Flüssigkeiten suspendierten Teilchen". In: *Annalen der Physik* 322.8 (), pp. 549–560.

[82] Shūichi Nosé. "A molecular dynamics method for simulations in the canonical ensemble". In: *Molecular Physics* 52.2 (1984), pp. 255–268.

[83] H. C. Andersen. "Molecular dynamics simulations at constant pressure and/or temperature". In: *J. Chem. Phys.* 72 (1980), p. 2384.

[84] A. Kolodziejczak-Radzimska and T. Jesionowski. "Zinc Oxide-From Synthesis to Application: Review". In: *Materials* 7 (2014), pp. 2833–2881.

[85] Z.L. Wang and J.H. Song. "Piezoelectric Nanogenerators Based on Zinc Oxide Nanowire Arrays". In: *Science* 312 (2006), pp. 242–246.

[86] Z. Yang et al. "Mixed-Quantum-Dot Solar Cells". In: *Nat. Comm.* 8 (2017), pp. 1325–1233.

[87] E. H. Sargent. "Colloidal Quantum Dot Solar Cells". In: *Nat. Photon.* 6 (2012), pp. 133–135.

[88] O. E. Semonin, J. M.Luther, and M. C.Beard. "Quantum Dots for Next-generation Photovoltaics". In: *Materials Today* 15 (2012), pp. 508–515.

[89] K. S. Leschkies et al. "Photosensitization of ZnO Nanowires with CdSe Quantum Dots for Photovoltaic Devices". In: *Nano Lett.* (2007), pp. 1793–1798.

[90] S. Bley et al. "Electron Tunneling from Colloidal CdSe Quantum Dots to ZnO Nanowires Studied by Time-Resolved Luminescence and Photoconductivity Experiments". In: *J. Phys. Chem. C* 119 (2015), pp. 15627–15635.

[91] T. Le Bahers et al. "Acetylacetone using DFT and IR". In: *Langmuir* 27 (2011), pp. 3442–34450.

[92] J. Kiss et al. "Combined Theoretical and Experimental Study on the Adsorption of Methanol on the ZnO(10-10) Surface". In: *J. Phys. Chem. A* 115 (2011), pp. 7180–7188.

[93] A. Calzolari, A. Ruini, and A. Catellani. "Anchor Group versus Conjugation: Toward the Gap-State Engineering of Functionalized ZnO$(10\bar{1}0)$ Surface for Optoelectronic Applications". In: *J. Am. Chem. Soc.* 133 (2011), pp. 5893–5899.

[94] N. H. Moreira, A. L. Rosa, and Th. Frauenheim. "Covalent Functionalization of ZnO Surfaces: a Density-Functional Tight-Binding Study". In: *Appl. Phys. Lett.* 94 (2009), pp. 193109–1–193109–3.

[95] N. H. Moreira et al. "On the Stabilization Mechanisms of Organic Functional Groups on ZnO Surfaces". In: *Phys. Chem. Chem. Phys.* 14 (2012), pp. 15445–15451.

[96] X. Q. Shi et al. "Substrate Mediated Stabilization of Methylphosphonic Acid on ZnO Non-polar Surfaces". In: *Surf. Sci.* 606 (2012), pp. 289–292.

[97] A. Dominguez et al. "First Principles Investigations on the Electronic Structure of Anchor Groups on ZnO Nanowires and Surfaces". In: *J. Appl. Phys.* 115 (2014), pp. 203720–1–203720–9.

[98] R. Franking R. E. Ruther et al. "Formation of Smooth, Conformal Molecular Layers on ZnO Surfaces via Photochemical Grafting". In: *Langmuir* 27 (2011), pp. 10604–10614.

[99] J. Chen et al. "Molecular Adsorption on ZnO$(10\bar{1}0)$ Single-crystal Surfaces: Morphology and Charge Transfer". In: *Langmuir* 28 (2012), pp. 10437–10445.

[100] Dennis Franke et al. "Hybrid Density-Functional Theory Calculations of Electronic and Optical Properties of Mercaptocarboxylic Acids on ZnO(1010) Surfaces". In: *The Journal of Physical Chemistry C* 122.43 (2018), pp. 24838–24842. DOI: 10.1021/acs.jpcc.8b08412.

[101] G. Kresse and J. Hafner. "Ab initio molecular dynamics for liquid metals". In: *Phys. Rev. B* 47 (1993), p. 558.

[102] G. Kresse and J. Hafner. "Ab initio molecular-dynamics simulation of the liquid-metal–amorphous-semiconductor transition in germanium". In: *Phys. Rev. B* 49 (1994), p. 14251.

[103] G. Kresse and J. Furthmüller. "Efficiency of ab-initio total energy calculations for metals and semiconductors using a plane-wave basis set". In: *Comput. Mat. Sci.* 6.1 (1996), pp. 15–50.

[104] G. Kresse and J. Furthmüller. "Efficient iterative schemes for ab initio total-energy calculations using a plane-wave basis set". In: *Phys. Rev. B* 54 (1996), p. 11169.

[105] A. Dominguez et al. "First principles investigations on the electronic structure of anchor groups on ZnO nanowires and surfaces". In: *Journal of Applied Physics* 115.20 (2014), p. 203720.

[106] "CRC handbook of chemistry and physics: A ready-reference book of chemical and physical data". In: ed. by W. M. Haynes. 97th. Boca Raton: CRC Press, 2016.

[107] P. Umari et al. "Energy-level alignment in organic dye-sensitized TiO2 from GW calculations". In: *The Journal of Chemical Physics* 139.1 (2013), p. 014709.

[108] Jun Kang et al. "Band offsets and heterostructures of two-dimensional semiconductors". In: *Applied Physics Letters* 102.1 (2013), p. 012111.

[109] M. Gajdos et al. "Linear Optical Properties in the Projector-Augmented Wave Methodology". In: *Phys. Rev. B* 73 (2006), pp. 045112–1–045112–9.

[110] E. Luppi, I. Urdaneta, and M. Calatayud. "Photoactivity of Molecule-TiO2 Clusters with Time-Dependent Density-Functional Theory". In: *J. Phys. Chem. C* 120 (2016), pp. 5115–5124.

[111] M. E. Casida. "Recent Advances in Density Functional Methods". In: vol. 1. World Scientific, Singapore, edited by D. P. Chong, 1995.

[112] Shuji Nakamura, Masayuki Senoh, and Takashi Mukai. "Highpower InGaN/GaN doubleheterostructure violet light emitting diodes". In: *Applied Physics Letters* 62.19 (1993), pp. 2390–2392.

[113] H. Morkoç et al. "Largebandgap SiC, IIIV nitride, and IIVI ZnSebased semiconductor device technologies". In: *Journal of Applied Physics* 76.3 (1994), pp. 1363–1398.

[114] Jae-Ryoung Kim et al. "Electrical transport properties of individual gallium nitride nanowires synthesized by chemical-vapor-deposition". In: *Applied Physics Letters* 80.19 (2002), pp. 3548–3550.

[115] D. J. Guo et al. In: *Langmuir* 26 (2010), p. 18382.

[116] H. Kim et al. In: *Langmuir* 22 (2006), p. 8121.

[117] E. H. Williams et al. In: *Surf. Sci* 627 (2014), p. 23.

[118] M.-Ki Choi et al. In: *Sci. Rep.* 7 (2017), p. 14917.

[119] M. Zhou and C. V. Robinson. In: *Trends Biochem. Sci.* 35 (2010), p. 522.

[120] J. Kool et al. In: *Anal. Bioanal. Chem.* 401 (2011), p. 1109.

[121] C. Wöll. In: *Prog. Surf. Sci.* 82 (2007), p. 55.

[122] S. U. Schwarz et al. In: *Langmuir* 29 (2013), p. 6296.

[123] C. Arisio, C. A. Cassou, and M Lieberman. In: *Langmuir* 29 (2013), p. 5145.

[124] V. M. Bermudez. In: *Langmuir* (2003), p. 6813.

[125] R. Stine et al. In: *Appl. Surf. Sci.* 256 (2010), p. 4171.

[126] A. J. Garza and G. E. Scuseria. In: *J. Phys. Chem. Lett.* 7 (2016), p. 4165.

[127] Herbert A. Weakliem. "Optical Spectra of Ni2+, Co2+, and Cu2+ in Tetrahedral Sites in Crystals". In: *The Journal of Chemical Physics* 36.8 (1962), pp. 2117–2140.

[128] P. Koidl. "Optical absorption of Co^{2+} in ZnO". In: *Phys. Rev. B* 15 (5 1977), pp. 2493–2499.

[129] Sebastian Geburt et al. "Intense intra-3d luminescence and waveguide properties of single Co-doped ZnO nanowires". In: *physica status solidi (RRL) – Rapid Research Letters* 7.10 (), pp. 886–889.

[130] Igor Djerdj et al. "Co-Doped ZnO nanoparticles: Minireview". In: *Nanoscale* 2 (7 2010), pp. 1096–1104.

[131] I. Abdolhosseini Sarsari et al. "Many-body quasiparticle spectrum of Co-doped ZnO: A *GW* perspective". In: *Phys. Rev. B* 87 (24 2013), p. 245118.

[132] Rebecca Janisch, Priya Gopal, and Nicola A Spaldin. "Transition metal-doped TiO 2 and ZnO—present status of the field". In: *Journal of Physics: Condensed Matter* 17.27 (2005), R657.

[133] S. Das Sarma. "Spintronics - A new class of device based on the quantum of electron spin, rather than on charge, may yield the next generation of microelectronics". In: *American Scientist* 89 (2001), pp. 516–523.

[134] R.P. Feynman. "Quantum mechanical computers". In: *Foundation of Physics* 16.6 (1986), pp. 507–531.

[135] Vijayaprasath Gandhi et al. "Effect of Cobalt Doping on Structural, Optical, and Magnetic Properties of ZnO Nanoparticles Synthesized by Co-precipitation Method". In: *The Journal of Physical Chemistry C* 118.18 (2014), pp. 9715–9725.

[136] C. Ronning et al. "Tailoring the properties of semiconductor nanowires using ion beams". In: *physica status solidi (b)* 247.10 (), pp. 2329–2337.

[137] Sebastian Geburt et al. "Intense Intrashell Luminescence of Eu-Doped Single ZnO Nanowires at Room Temperature by Implantation Created Eu–Oi Complexes". In: *Nano Letters* 14.8 (2014), pp. 4523–4528.

[138] J. Segura-Ruiz et al. "Nano-X-ray Absorption Spectroscopy of Single Co-Implanted ZnO Nanowires". In: *Nano Letters* 11.12 (2011), pp. 5322–5326.

[139] Kenji Ueda, Hitoshi Tabata, and Tomoji Kawai. "Magnetic and electric properties of transition-metal-doped ZnO films". In: *Applied Physics Letters* 79.7 (2001), pp. 988–990.

[140] C. Rath et al. "Effect of cobalt substitution on microstructure and magnetic properties in ZnO nanoparticles". In: *Indian Journal of Physics* 83.4 (2009), pp. 415–421.

[141] H.-J. Schulz and M. Thiede. "Optical spectroscopy of $3d^7$ and $3d^8$ impurity configurations in a wide-gap semiconductor (ZnO:Co,Ni,Cu)". In: *Phys. Rev. B* 35 (1 1987), pp. 18–34.

[142] Zhengwu Jin et al. "High throughput fabrication of transition-metal-doped epitaxial ZnO thin films: A series of oxide-diluted magnetic semiconductors and their properties". In: *Applied Physics Letters* 78.24 (2001), pp. 3824–3826.

[143] Claire A. Johnson et al. "Sub-band-gap photoconductivity in Co^{2+}-doped ZnO". In: *Phys. Rev. B* 81 (12 2010), p. 125206.

[144] Chris G. Van de Walle and Jörg Neugebauer. "First-principles calculations for defects and impurities: Applications to III-nitrides". In: *Journal of Applied Physics* 95.8 (2004), pp. 3851–3879.

[145] Fumiyasu Oba et al. "Defect energetics in ZnO: A hybrid Hartree-Fock density functional study". In: *Phys. Rev. B* 77 (24 2008), p. 245202.

[146] S. B. Zhang, S.-H. Wei, and Alex Zunger. "Intrinsic n-type versus p-type doping asymmetry and the defect physics of ZnO". In: *Phys. Rev. B* 63 (7 2001), p. 075205.

[147] E. Kaxiras. "Atomic and Electronic Structure of Solids". In: Cambridge: Cambridge University Press, 2003.

[148] Anderson Janotti and Chris G. Van de Walle. "Native point defects in ZnO". In: *Phys. Rev. B* 76 (16 2007), p. 165202.

[149] G. S. Chang et al. "Effect of Co and O defects on the magnetism in Co-doped ZnO: Experiment and theory". In: *Phys. Rev. B* 75 (19 2007), p. 195215.

[150] Christoph Friedrich, Mathias C. Müller, and Stefan Blügel. "Band convergence and linearization error correction of all-electron *GW* calculations: The extreme case of zinc oxide". In: *Phys. Rev. B* 83 (8 2011), p. 081101.

[151] Ji ří Klime š, Merzuk Kaltak, and Georg Kresse. "Predictive *GW* calculations using plane waves and pseudopotentials". In: *Phys. Rev. B* 90 (7 2014), p. 075125.

[152] Stephan Lany and Alex Zunger. "Many-body *GW* calculation of the oxygen vacancy in ZnO". In: *Phys. Rev. B* 81 (11 2010), p. 113201.

[153] B. Meyer and Dominik Marx. "Density-functional study of the structure and stability of ZnO surfaces". In: *Phys. Rev. B* 67 (3 2003), p. 035403.

[154] Youngho Kang et al. "*GW* calculations on post-transition-metal oxides". In: *Phys. Rev. B* 89 (16 2014), p. 165130.

[155] Hong Jiang and Peter Blaha. "*GW* with linearized augmented plane waves extended by high-energy local orbitals". In: *Phys. Rev. B* 93 (11 2016), p. 115203.

[156] Andreas Grüneis et al. "Ionization Potentials of Solids: The Importance of Vertex Corrections". In: *Phys. Rev. Lett.* 112 (9 2014), p. 096401.

[157] A. Janotti and C. G. van de Walle. "Native point defects in ZnO". In: *Phys. Rev. B* 76 (2007), p. 165202.

[158] Stephan Lany and Alex Zunger. "Accurate prediction of defect properties in density functional supercell calculations". In: *Modelling and Simulation in Materials Science and Engineering* 17.8 (2009), p. 084002.

[159] Bi-Ching Shih et al. "Quasiparticle Band Gap of ZnO: High Accuracy from the Conventional G^0W^0 Approach". In: *Phys. Rev. Lett.* 105 (14 2010), p. 146401.

[160] C. Kittel. "Introduction to Solid State Physics". In: New York: Wiley, 1986.

[161] Hong Jiang et al. "Localized and Itinerant States in Lanthanide Oxides United by *GW* @ LDA + *U*". In: *Phys. Rev. Lett.* 102 (12 2009), p. 126403.

[162] Dandan Wang et al. "Defects-Mediated Energy Transfer in Red-Light-Emitting Eu-Doped ZnO Nanowire Arrays". In: *The Journal of Physical Chemistry C* 115.46 (2011), pp. 22729–22735.

[163] X. Zhao and D. Vanderbilt. "First-principles study of structural, vibrational, and lattice dielectric properties of hafnium oxide". In: *Phys. Rev. B* 65 (2002), p. 233106.

[164] D. Ceresoli and D. Vanderbilt. "Structural and dielectric properties of amorphous ZrO_2 and HfO_2". In: *Phys. Rev. B* 74 (2006), p. 125108.

[165] E. P. Gusev et al. "Ultrathin HfO_2 films grown on Silicon by atomic layer deposition for advanced gate dielectrics applications". In: *Microelectron. Eng.* 69 (2003), p. 145.

[166] Y. Wang et al. "Structure and dielectric properties of amorphous high- oxides: HfO_2, ZrO_2 and their alloys". In: *Phys. Rev. B* 85 (2012), p. 224110.

[167] H. Momida et al. "Dielectric constants of amorphous hafnium aluminates: First-principles study". In: *Phys. Rev. B* 75 (2007), p. 195105.

[168] P. Broqvist and A. Pasquarello. "Amorphous hafnium silicates: structural, electronic and dielectric properties". In: *Microelectron. Eng.* 84.9-10 (2007), pp. 2416–2419.

[169] N. Kaiser and H. K. Pulker. *Optical Interference Coatings*. Springer, 2003.

[170] W. L. Scopel, A. J. R. da Silva, and A. Fazzio. "Amorphous HfO_2 and $Hf_{1-x}Si_xO$ via a melt-and-quench scheme using ab initio molecular dynamics". In: *Phys. Rev. B* 77 (2008), p. 172101.

[171] P. Broqvist and A. Pasquarello. "First principles investigation of defects at interfaces between silicon and amorphous high-kappa oxides". In: *Microelectron. Eng.* 84.9-10 (2007), pp. 2022–2027.

[172] P. Broqvist and A. Pasquarello. "Band gaps and dielectric constants of amorphous hafnium silicates: A first-principles investigation". In: *Appl. Phys. Lett.* 90.8 (2007), p. 082907.

[173] J. Strand et al. "Hole trapping in amorphous HfO_2 and Al_2O_3 as a source of positive charging". In: *Microelectron. Eng.* 84 (2017), pp. 2370–3.

[174] J. Strand, M. Kaviani, and A. L. Shluger. "Defect creation in amorphous HfO_2 faciliated by hole and electron injection". In: *Microelectron. Eng.* 84 (2017), pp. 2370–3.

[175] Dennis Franke et al. "Density functional based tight-binding parametrization of hafnium oxide: Simulations of amorphous structures". In: *Phys. Rev. B* 98 (7 2018), p. 075207. DOI: 10.1103/PhysRevB.98.075207.

[176] V. Ukirde. "Trapping of Hydrogen in Hafnium-based High Kappa Dielectric Thin Films for Advanced CMOS Applications". PhD thesis. University of North Texas, 2007.

[177] P. A. Romans, O. G. Paasche, and H. Kato. "The transformation temperature of hafnium". In: *J. Less-Common Met.* 8.3 (1965), pp. 213–215.

[178] O. N. Carlson, F. A. Schmidt, and H. A. Wilhelm. *Preparation of zirconium and hafnium metals by bomb reduction of their fluorides*. United States Atomic Energy Commission. Ames Laboratory at Iowa State College, 1956.

[179] J. Adam and M. D. Rogers. "The crystal structure of ZrO_2 and HfO_2". In: *Acta Crystallogr.* 12 (1959), p. 951.

[180] M. Elstner et al. "Self-consistent-charge density-functional tight-binding method for simulations of complex materials properties". In: *Phys. Rev. B* 58 (1998), p. 7260.

[181] G. V. Lewis and C. R. A. Catlow. "Potential models for ionic oxides". In: *J. Phys. C: Solid State Phys.* 18 (1985), pp. 1149–1161.

[182] D. Wolf et al. "Exact method for the simulation of Coulombic systems by spherically truncated, pairwise r^{-1} summation". In: *J. Chem. Phys.* 110 (1999), p. 8254.

[183] C. Kaneta and T. Yamasaki. "Oxygen-related defects in amorphous HfO_2 gate dielectrics". In: *Microelectron. Eng.* 84 (2007), pp. 2370–3.

[184] T. Köhler et al. "Computational approach for structure design and prediction of optical properties in amorphous TiO_2 thin-film coatings". In: *J. Phys. D: Appl. Phys.* 46 (2013), p. 325302.

[185] M. Turowski et al. "Practice-oriented optical thin film growth simulation via multiple scale approach". In: *Thin Solid Films* 592 (2015), pp. 240–247.

[186] M. Turowski et al. "Modeling of Al_2O_3 Thin Film Growth in Modern Ion Coating Processes". In: *Optical Interference Coatings*. OSA Technical Digest, 2013.

[187] V. I. Gavrilenko and R. Q. Wu. "Linear and nonlinear optical properties of group-III nitrides". In: *Phys. Rev. B* 61 (4 2000), pp. 2632–2642.

[188] N. Ikarashi and K. Manabe. "Electronic structure analysis of Zr silicate and Hf silicate films by using spatially resolved valence electron energy-loss spectroscopy". In: *J. Appl. Phys.* 94 (2003), p. 480.

[189] M. C. Cheynet et al. "Crystal structure and band gap determination of HfO_2 thin films". In: *J. Appl. Phys.* 101 (2007).

[190] T.-J. Chen and C.-L. Kuo. "First Principles Study of the Structural, Electronic, and Dielectric Properties of Amorphous HfO_2". In: *J. Appl. Phys.* 110.6 (2011), p. 064105.

[191] I.Z. Mitrovic et al. "Electrical and structural properties of hafnium silicate thin films". In: *Microelectronics Reliability* 47.4 (2007), pp. 645 –648.

[192] John Robertson. "High dielectric constant gate oxides for metal oxide Si transistors". In: *Reports on Progress in Physics* 69.2 (2006), p. 327.

[193] C. Koehler et al. "Theoretical investigation of carbon defects and diffusion in α-quartz". In: *Phys. Rev. B* 64 (2001), p. 085333.

[194] T.-J. Chen and C.-L. Kuo. "Structural, electronic, and dielectric properties of amorphous hafnium silicates". In: *J. Appl. Phys.* 110 (2011), p. 114105.

[195] J.P. Trinastic et al. "Unifies interatomic potential and energy barrier distributions for amorphous oxides". In: *J. Chem. Phys.* 139 (2013), p. 154506. DOI: 10.1063/1.4825197.

[196] B. W. H. van Beest, G. J. Kramer, and R. A. van Santen. "Force fields for silicas and aluminophosphates based on ab initio calculations". In: *Phys. Rev. Lett.* 64 (16 1990), pp. 1955–1958.

[197] B. D. Sharma and J. Donohue. "A refinement of the crystal structure of gallium". In: *Zeitschrift für Kristallographie* 117 (1962), pp. 293–300.

[198] L. Bosio et al. "Structure cristalline du gallium β". In: *Acta Crystallographica Section B* 25.5 (1969), p. 995.

[199] Louis Bosio. "Crystal structures of Ga(II) and Ga(III)". In: *The Journal of Chemical Physics* 68.3 (1978), pp. 1221–1223.

[200] Takemura Kenichi, Kobayashi Kazuaki, and Arai Masao. "High-pressure bct-fcc phase transition in Ga". In: *Phys. Rev. B* 58 (5 1998), pp. 2482–2486.

[201] I. Vurgaftman and J. R. Meyer. "Band parameters for nitrogen-containing semiconductors". In: *Journal of Applied Physics* 94.6 (2003), pp. 3675–3696.

[202] N. E. Christensen and I. Gorczyca. "Optical and structural properties of III-V nitrides under pressure". In: *Phys. Rev. B* 50 (7 1994), pp. 4397–4415.

[203] Michael Gaus, Albrecht Goez, and Marcus Elstner. "Parametrization and Benchmark of DFTB3 for Organic Molecules". In: *Journal of Chemical Theory and Computation* 9.1 (2013), pp. 338–354.

[204] John E. Northrup and J. Neugebauer. "Theory of GaN$(10\bar{1}0)$ and $(11\bar{2}0)$ surfaces". In: *Phys. Rev. B* 53 (16 1996), R10477–R10480.